University of Alberta

System Modeling and Controller Designs for a Peltier-based thermal device in microfluidic application

by

Jingbo Jiang

A thesis submitted to the Faculty of Graduate Studies and Research
in partial fulfillment of the requirements for the degree of

Doctor of Philosophy

in

Controls

Department of Electrical and Computer Engineering

Spring 2010

Edmonton, Alberta

Examining Committee

Dr. Horacio J. Marquez	Supervisor, Electrical and Computer Engineering
Dr. Chris J. Backhouse	Electrical and Computer Engineering
Dr. Qing Zhao	Electrical and Computer Engineering
Dr. Sirish L. Shah	Chemical and Material Engineering
Dr. Kenneth A. McIsaac	External, Electrical and Computer Engineering, University of Western Ontario

To my parents,
You supports are endless and priceless.

Abstract

A custom-made Peltier-based thermal device is designed to perform miniaturized bio-molecular reactions in a microfluidic platform for medical diagnostic tests, especially the polymerase chain reaction for DNA amplification. The cascaded two-stage device is first approximated by multiple local linear models whose parameters are obtained by system identification. A decentralized switching controller is proposed, where two internal model-based PI controllers are used in local stabilizations and PD and PI controllers are applied during transitions respectively. Couplings and drift are further reflected into the controllers. Desired temperature tracking performance on the transition speed and overshoot is achieved, and the feasibility of the Peltier device in a microfluidic platform is further validated by the successful applications of viral detection.

To achieve fast and smooth transition while avoiding tuning by trial-and-errors, a nonlinear model is developed based on the first principles, whose parameters are partially calculated from empirical rules and partially determined by open-loop and closed-loop experimental data. Two novel nonlinear controllers are designed based on the nonlinear model. The first controller extends the input-to-state feedback linearization technique to a class of nonlinear systems that is affine on both the control inputs and the square of control inputs (including the Peltier system). Additional local high gain controllers are introduced to reduce the steady-state errors due to parameter uncertainty. The second controller is a time-based switching controller which switches between nonlinear pseudo-PID/ state feedback controllers and local PI controllers. Calculation burden is reduced and steady-state error is minimized using a PI controller locally, while fast and smooth transition is achieved by the nonlinear counterpart. The robustness of the controller is verified in simulation un-

der worse case scenarios. Both simulation and experimental results validated the effectiveness of the two nonlinear controllers.

The proposed linear/ nonlinear, switching/ non-switching controllers provide different options for the Peltier-based thermal applications. The scalability and the parameter updating capability of the nonlinear controllers facilitate the extension of the Peltier device to other microfluidic applications .

Acknowledgements

Life at graduate school is a mixture of surprises, frustrations, and happiness, and also is full of cherishable memories of friends, supervisor, and collaborators.

Dr. Horacio Marquez has been my supervisor for the past seven years and allowed me great freedom to explore various research areas and find the research subject with mixed theoretical contribution and practical application. I am extremely grateful for his patience, guidance, and support.

The collaboration with the Applied Miniaturization Laboratory is fascinating and inspiring. Dr. Chris Backhouse is a pioneer in the microfluidics-based medical device development, and his group is in the process of bringing low-cost and reliable cancer diagnostic devices into reality. I am really honored and grateful to be part of this multi-disciplinary project. I shared most of my laboratory time in the instrumentation and controller implementation with Dr. Govind Kaigala from the AML, his knowledge and enthusiasm was instrumental to overcome many obstacles encountered during the implementation of our design. Also, many thanks to Mr. Loi Hua, Mr. Mohammad Behnam and other technicians in the AML. Their invaluable technical support and help on the instrumentation were important for the realization of this research work.

My stay at the University of Alberta would not have been pleasant without other encouraging and open-minded professors and the friendly and energetic graduate students in the Systems and Control laboratory. As a member of this small scientific community, countless discussions and debates, generous time and effort on the team work will be great asset for my future career.

Last but not the least I would like to thank my parents for their love and confidence in me.

Table of Contents

List of Tables

List of Figures

List of Abbreviations and Acronyms

ARX	Auto Regression with external input
CE	Capillary Electrophoresis
CT	Continuous Time
DAC	Digital to Analog Converter
DNA	Deoxyribonucleic Acid
DT	Discrete Time
EFBL	Extended Feedback Linearization
GUI	Graphic User Interface
HMI	Human Machine Interface
IC	Integrated Circuit
IMC	Internal Model Control
IR	Infrared Radiation
LIF	Laser Induced Fluorescence
LPV	Linear Parameter Varying
LQR	Linear Quadratic Regulation
LTR	Loop Transfer Recovery
MIMO	Multi Input Multi Output
PCR	Polymerase Chain Reaction
PDMS	Polydimethylsiloxane
PEM	Prediction Error Method
PMMA	Polymethylmethcrylate
PID	Proportional Integral Derivative

RBS	Random Binary Signal
RGA	Relative Gain Array
SISO	Single Input Single Output
TEM	Thermoelectric Module
TS	Takagi-Sugeno

Chapter 1

Introduction

1.1 Motivation of the research

Miniaturization via microfluidic approaches of conventional molecular biology techniques for disease diagnosis results in a significant reduction of analysis times and reagent costs, which provides great opportunity for low-cost and portable medical device development. Microfluidic devices formed using photolithographic techniques are enabling the miniaturization of conventional molecular biology techniques, leading to rapid and low volume implementations [70]. In addition, unlike conventional commercial thermal cycling devices, integration of multiple biological reactions in one microchip is achievable under a microfluidic platform by an elaborate microchip design and fabrication. Furthermore, the growing demand for rapid gene expression and mutation analysis in pharmaceutical research has stimulated the development in the field of high throughput analytical instrumentation and approaches [69]. Microfluidics is suitable for both coupled-process and also for high-throughput analysis. It is envisaged that microfluidic devices will lend themselves to the integration of functionalities necessary for portable diagnostic devices and simultaneously for high throughput screening applications [4, 33]. With increased interest in clinical diagnostics [70, 3], forensic laboratory testing [25], and population screening [26], instrumentation development surrounding microfluidic devices is gaining importance in a total analysis system development with speed, specificity, portability and economics being the crucial considerations. Numerous conventional molecular biology procedures have been ported to the microfluidic

platforms e.g. Polymerase Chain Reaction (PCR) [52], DNA sequencing [2] and diagnostics and prognosis on the genetic basis of the diseases [17].

A multidisciplinary research project is organized here in the Alberta Cross Cancer Institute (ACCI) for developing portable devices for clinical cancer diagnosis. As a part of the project, a low cost microfluidic platform for performing disease detection is designed and prototyped in the Applied Miniaturization Laboratory (AML) at the University of Alberta. Fig. 1.1 shows the prototype platform with its external power source and control box. A complete diagnostic test is performed by a set of coupling biochemical processes inside a polydimethylsiloxane (PDMS)/ glass microchip on the Peltier-based thermal device in the microfluidic platform.

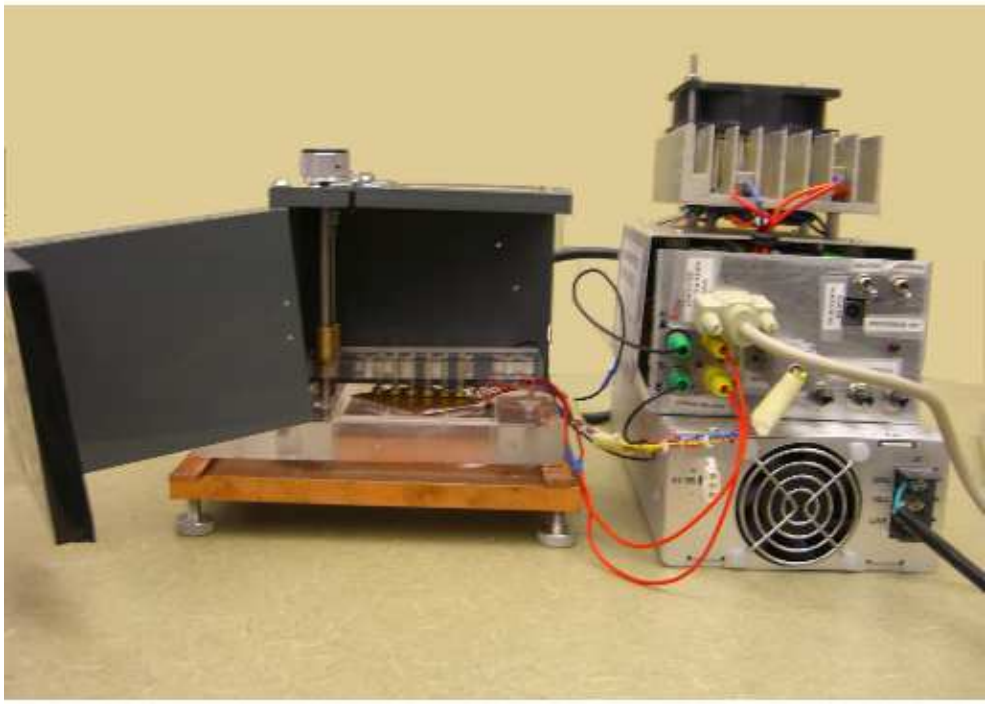

Figure 1.1: Prototype experimental microfluidic platform with its external control box. Peltier-based thermal device is on the left side, while the control box including the micro-controller and other auxiliary circuit boards is on the right side.

The entire microfluidic platform is functionally divided into five groups,

(a) A two-layer microchip with microfabricated channels, chambers and wells for amplification reaction and electrophoresis analysis.

(b) A set of finger-type probes with servo-motors for pumping and valving.

(c) A thermal device made of two-stage Peltier modules for thermal cycling.

(d) A group of circuit boards with a micro-controller, and other A/D and D/A IC chips interfacing the controller with the Peltier device.

(e) A Human Machine Interface (HMI) for operators to send operating instructions and record measurement data.

Various designs of microchips have been proposed in the literatures and have been customized to the specific molecular biological test and thermal heating device. The particular design of the microchip in our platform using Peltier-based thermal device for DNA amplification is composed of a glass substrate irreversibly bonded to a thin layer of a flexible sheet of polydimethylsiloxane (PDMS) [3]. The features of the microchip are a pair of $\sim$2.5μL wells (sample and waste), a central enclosed reaction chamber, 50μm wide and 14μm deep channels connecting the sample/waste wells to the reaction well (Fig. 1.2). By choosing a malleable PDMS top layer, external forces can easily be applied to deform the microstructures shaped into the PDMS, which help to implement integrated pumping and valving of reaction solutions [19].

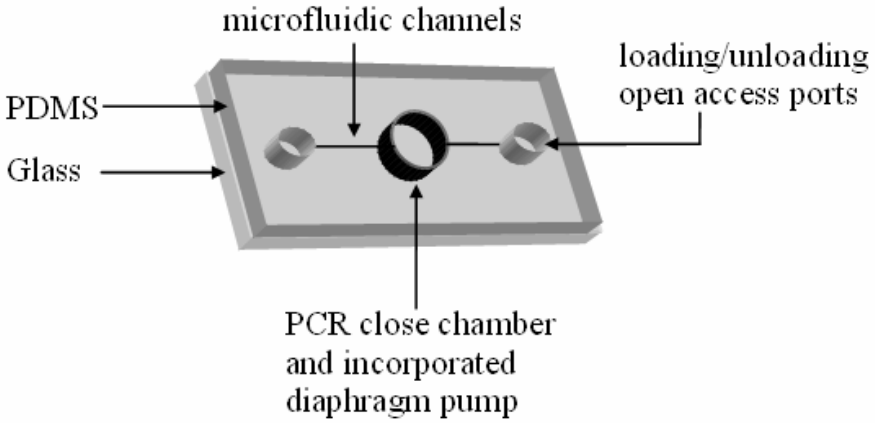

Figure 1.2: Schematic diagram of a hybrid PDMS/glass 3-port PCR microchip consisting of an enclosed hollow chamber molded into the PDMS and other loading and unloading ports flanking the PCR chamber.

The cascaded Peltier-based thermal device is composed of two single-stage, square shape, Bismuth Telluride (Bi_2Te_3)-based Peltier modules, a few interfacing high-purity copper plates, and three thermocouples. Heating and cooling actions are controlled by the two separated voltage inputs to the two Peltier modules. The entire thermal device is enclosed inside a polymethylmethcrylate (PMMA) frame and supported by a large heat sink made of pure copper.

Six finger type probes are held by a horizontal beam placed on top of the chip holder and are driven by a series of Hitec HS-300 servo-motors to anchor the chip position and perform pumping and valving. The vertical motion of each finger probe is controlled by a microprocessor board that sends instructions to the motors. Integrated diaphragm pumping and pinch-off valving techniques are adopted here using the finger probes and the two layer PDMS/glass microchip, which are the key elements of a robust fluidic control system that is suitable for PCR genetic amplification and capable of repeated cycles of sample loading and unloading in an automated fashion. The valving system takes advantage of the malleable PDMS layer design and applies constant valving pressure to a channel without direct contact with the PCR reaction mixture. Valving is realized by applying enough pressure to a localized region of the PMDS layer to compress and close the inflow and outflow channels of the reaction reservoir. Ultimately, this approach can facilitate the integration of the PCR process with other portions of a microfluidic analysis platform. Details of the pumping and valving designs and the programming of the control sequences of the servo-motors are elaborated in [54, 32].

The thermal management component in this platform provides precise and efficient thermal tracking performance for different molecular bio-reactions, such as Polymerase Chain Reaction (PCR). The accuracy of the temperature tracking performance will govern the reaction efficiency (activity of enzyme for reaction), while the speed of thermal cycles will dominate the overall reaction time. Although there are off-the-shelf PID controller structure IC chips [12] and other manufacturer-provided thermal control box available for single-stage Peltier modules, the covered temperature range for a single module will be really large (about 70°C) and the modules are not operated at high thermal efficiency region. Multiple-stage

Peltier modules are preferred to reduce the operating range of individual Peltier module and the transition time (smaller range leads to faster transition), and improve the thermal efficiency (usually achieved around 30°C). However, there are very few controllers with multiple inputs available in industry and usually end-users have to design dedicated controllers for custom-made multi-input-multi-stage Peltier-modules. In this thesis, we focus on developing model-based multi-input controllers of Peltier-based thermal devices for various bio-molecular reactions in microfluidic platforms, especially to achieve fast and efficient PCR amplification.

1.2 Thermal requirement of PCR

As a key procedure for successful disease diagnosis, DNA amplification through PCR test is central since the DNA concentration in patients' samples is relatively low. In a typical PCR operation, usually 30-40 temperature cycles of DNA amplification are required, after each cycle the focused DNA segment will be ideally doubled. In a single PCR temperature cycle, there includes three bio-molecular steps:

(a) **Denaturation**: Involves melting of the double stranded DNA to form two single strands of DNA. The temperature is typically as high as 92-96°C. Strict temperature range (about$\pm$1°C) is necessary. If temperature is under 93°C, DNA may not denature efficiently, while temperature above 97°C may cause boiling of the sample or destruction of enzymes.

(b) **Annealing**: Binding of the primers (short fragments of DNA) to a specific location on each denatured DNA strand. This occurs in the temperature range 45-65°C. The optimal temperature for this step is selective and depends on the particular sequence of DNA primer, as primers ideally bind only to complementary sequence. In a temperature range within $\pm$1°C around the optimal temperature for a specific DNA sequence, the correct DNA match is achieved. Large temperature errors away from the set-point may cause incorrect sequences to be amplified or other failures.

(c) **Extension**: The primers are enzymatically extended to form the complementary strand of DNA typically at 68-74°C. For this step, the optimal temperature depends on the specific optimal temperature for the enzymatic activity. Approximately $\pm$1°C around 72°C is an acceptable range within which the reaction efficiency is retained.

Transitions between these temperature zones must occur rapidly to reduce the overall processing time and each set-point must be confined within a tight bound to improve the activity of the Taq polymerase (enzyme necessary for PCR). In addition, thermal constraints imposed by PCRs are stringent, such a thermal system developed for PCR is readily usable for other sensitive bio-chemical tests. Both the physical configurations of the thermal device and the digital controller designs will be crucial for the success of these microfluidics-based disease diagnostic applications.

1.3 Thermal device selection

Numerous commercial systems conventionally used in the life sciences (e.g. Applied Biosystems [6], Bio-Rad [8], Eppendorf [10]) are currently available for (non-microchip based) large volume PCR temperature cycling. However, no analysis capabilities are provided, hence, the resulting PCR mixture needs to be manually transferred onto other equipment for analysis. Additional features like integration with other upstream processes like sample preparation and down-stream processes like analyte separation (detection) are also not integrated in any of the commercial systems. Unlike conventional commercial thermal cycling devices, integration of multiple biological reactions in one microchip is achievable in a microfluidic platform using an elaborate microchip design and fabrication. Many sequential PCR-CE microchips have been reported [42], which will have a few extra physical designs and temperature profile requirements on the heating module in the microfluidic platform.

Various thermal heating methods have been developed for microfluidics-based PCR application, reference [73] is a recent review on different techniques used in

PCR microfluidic devices. Broadly, on the basis of the position of the fluid being heated, thermal cycling could be performed by two approaches. One is the stationary approach where the fluid is stationary and the temperature of the heater is changing [28,43,64]. The other one is a continuous-flow amplification approach in which the reaction mixture is pumped continuously through the chip and flows repeatedly through fixed temperature zones where multiple heaters are used to maintain different temperatures at different locations [38, 52, 22]. In the continuous flow-through approach, often large cycle numbers are required, the determination of the time span for each cycle is difficult and the device is relatively difficult to integrate with other analytical processes. Based on the consideration of the simplicity and the applicability for multiple function integration, stationary PCR heating approach is preferred and employed in our platform. Depending on whether the heating module has direct contact with the microchip or not, these methods can also be divided in two groups: contact mode methods and non-contact mode methods. Contact mode methods using Peltier modules are reported in [34,50], while contact mode methods using patterned thin-film resistive heaters are reported in [72, 30, 53, 33]. Applications of non-contact methods include infrared radiation (IR) [23], laser-mediated heating [68] and microwave heating [66, 61]. However, the non-contact heating sources may require higher external power inputs and may be limited in the application range. Considering the relative large volume of the reaction solution (due to low DNA concentration in the solution from patients' urine sample), contact mode methods are adopted in our design. In the AML at the University of Alberta, contact mode stationary heating methods are preferred, both Peltier-based heating and embedded thin-film heater-based heating are studied and prototyped.

Peltier module, also known as thermoelectric module (TEM), is a widely used device for localized heat pump or power generation. Due to its small size, light weight, high precision, and combined heating and cooling abilities in one module, the use of Peltier device is found in various applications such as biochemical reaction in microfluidic devices [37, 34, 50], thermal energy sensors such as infrared detectors and cryogenic heat flux sensor [57], thermal modules for laser diodes, charge-coupled devices [57], refractometers [7], and cooling stage for scanning

electron microscope [9]. Due to the relatively low-cost, the simplicity to setup, and the capability of active cooling (often important in life-science applications), Peltier modules are widely used in both conventional PCR systems and microfluidic implementations. In addition, having a Peltier-based heating device separated from the microfluidic chip (as opposed to integrated within the chip such as resistive thin film elements-based heating), the microfabrication of the microfluidic chip could be largely simplified, resulting in significantly reduced cost per chip and thus the cost of the diagnostic test itself - this is central to developing low-cost microfluidic tests. Several microchip PCR demonstrations using the Peltier modules as the thermal device were reported and summarized in [59]. In the AML lab, Peltier-based heating system is first studied and designed mainly considering the simplicity in the micro-fabrication of the microchip and the lower cost compared to the thin-film heaters. In this thesis, the research work is focusing on Peltier-based thermal system and the corresponding controller designs.

1.4 Physical design of the Peltier-based thermal device

Most Peltier-based PCR applications have made use of a single stage module with either one-side or two-side sandwich type heating configuration. Although some single-stage Peltier modules have the ability to work over a large temperature differential required ($\Delta T > 70$°C), the Peltier module does not operate at its optimal thermal efficiency, and large reference point changes usually require longer transition time. To overcome these issues, multi-stage Peltier modules are used to reduce the temperature differential covered by individual stages, and also to allow the Peltier modules to operate at higher efficiencies. Off-the-shelf multi-stage modules have only one input available, wherein each Peltier module functions in the same thermal flux direction. Custom-made multi-input-multi-stage designs have been earlier reported in [55], with the intention to utilize more control inputs to achieve faster temperature transitions and smaller tracking errors. Here, a custom-made two-stage Peltier device with multiple inputs is designed and built in the AML,

which has a component cost of only up to 150 CAD (approximately 1/25-1/50 price of the commercial thermal cyclers). And we intend to achieve comparable thermal tracking performance to commercial thermal cyclers in terms transition speed and error bounds using advanced controller designs.

The two-stage Peltier module arrangement in a cascade mode is composed of five horizontal layers: a chip holder composed of two copper plates with an embedded temperature sensor, a top Peltier module, an intermediate copper plate with another temperature sensor, a bottom Peltier, and a larger volume copper plate as a heat sink with a temperature sensor (Fig. 1.3). High purity copper plates are used to enhance the heat transfer, to maintain temperature uniformity across the Peltier surfaces, and to provide the physical housing for the thermal sensors. Four bolts are used to support the heat sink to increase the surface area for air convection. This configuration of two stage Peltiers is set up to enhance the thermal efficiency of each Peltier with reduced operating temperature differential.

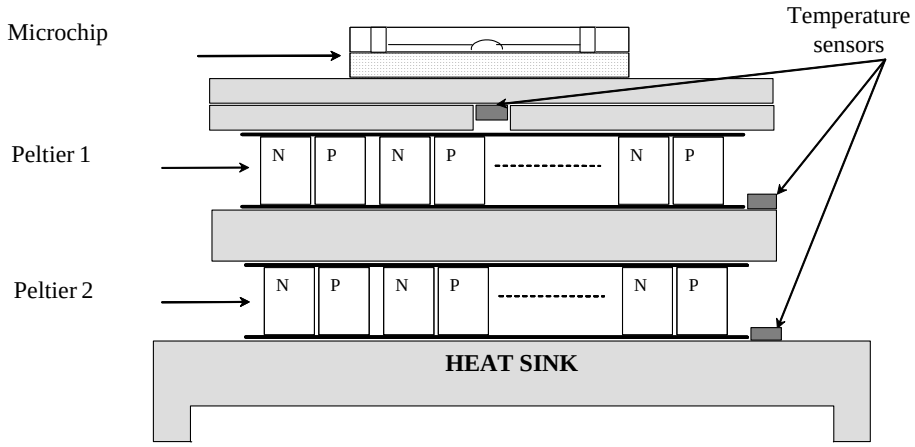

Figure 1.3: Schematic representation of the cascade stack of Peltier modules and copper plates along with embedded temperature sensors.

A Peltier module consists of multiple N-type/P-type semiconductor material-made couples which are thermally connected in parallel and electronically connected in series. Fig. 1.4 shows a schematic diagram of a Peltier module with four N/P couples which are mounted between two ceramic substrates. The substrates serve to hold the overall structure together mechanically and to insulate the individual elements electrically from one another and from external mounting surfaces.

N-type material is doped so that it will have an excess of electrons (more electrons than needed to complete a perfect molecular lattice structure) and P-type material is doped so that it will have a deficiency of electrons (fewer electrons than are necessary to complete a perfect lattice structure). The extra electrons in the N material and the ”holes” resulting from the deficiency of electrons in the P material are the carriers which move the heat energy through the thermoelectric material [14].

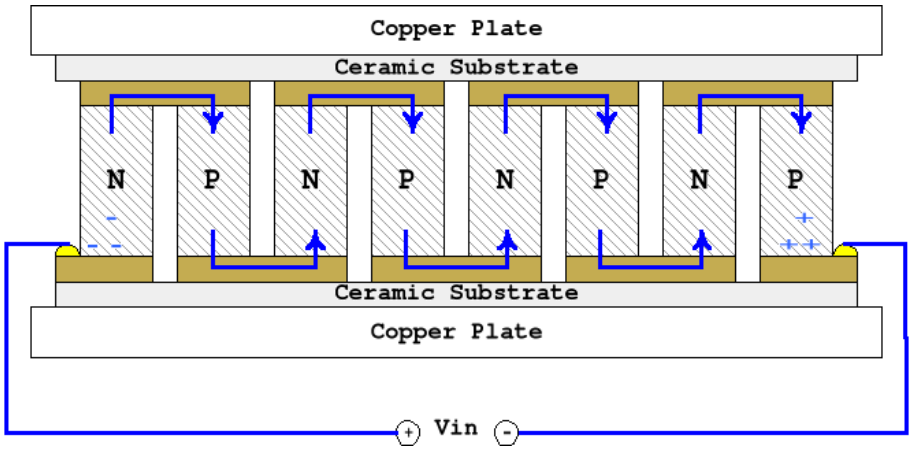

Figure 1.4: Schematic diagram of the configurations of a single Peltier module including four N-type/P-type couples. When an external voltage is applied, heat moves through the module in one direction according to the sign of the voltage while the electrical current moves back and forth alternately between the top and bottom substrates through each N and P element.

Peltier modules from FerroTec (9500/127/085B) are chosen in our device. Three temperature sensors from National Semiconductor (LM50) are connected to A/D converters from Texas Instruments (TLC2543). Numerical mapping between the temperature within the chamber of a PCR chip and the temperature of the chip holder is estimated by finite element analysis [27]. A PIC micro-controller from Microchip Technology Inc. (PIC18F458) generates digital control signals for the Peltier modules, whose digital control outputs are fed into a 12-bit D/A converter from Linear Technology Corp. (LTC1590) to drive maximum ± 10V bi-polar power amplifiers for the voltage inputs to the Peltiers. The details of the actuator design will be discussed later in Chapter 2. Data recording and external human-machine interfacing are provided through a computer using an RS232 serial connection.

1.5 Controller designs for Peltier-based thermal devices

For single-stage Peltier-based device in temperature regulation/tracking, linear PID controllers or switching PID controllers are commonly used due to their simplicities in both design and implementation [37, 56]. Such controllers are also available in off-the-shelf IC chips (e.g. IC Module MAX1978/MAX1979 [12]). For Peltier-based devices with multiple inputs, the design is more complicated as there are strong couplings between Peltier modules during extreme heating/cooling transitions and the system is nonlinear. For some two-stage Peltier-based device developed for microfluidic application in the literature [55], conventional single-input-single-output (SISO) model-based PID controllers are used in a decentralized framework. Separated linear controllers are applied to each Peltier without considering the coupling, in which the bottom Peltier is assumed to be maintained at a constant temperature while the top Peltier is controlled by a SISO model-based controller. However, without incorporating the coupling effects in the controller design, the performance in transition is not carefully controlled and intensive tuning of PID parameters are required.

To reduce the tuning effort and include the coupling and other nonlinear characteristics of the Peltier module into the controller, multiple-input-multi-output (MIMO) models are considered. Due to the limited time to have a feasible thermal device available for disease diagnostic tests in our earlier prototype development, linear system modeling and controller techniques are used. Three local MIMO models are developed using the temperature difference of the two sides of a Peltier module as the output. The model parameters around the three set-points are obtained by linear system identification. Using the local linear model, internal model control (IMC)-based PID controllers are designed for local stabilizations, while interpolations of local controllers combined with counter-coupling elements are applied during transitions. Mixed state/ time-based switching rules are introduced to set different controllers for the PCR cycling, while a few look-up tables of parameter resetting values are used to reflect coupling and other nonlinear characteristics

in the switching setting. This switching decentralized controller was simulated and tuned in simulation and further implemented in the micro-controller. The experimental results achieved faster transitions and smaller overshoots than the earlier SISO model-based design [55]. The effectiveness of the thermal device for PCR cycling in our microfluidic platform is further validated by the successful application of amplification of some viral DNA sample from patients' urine sample [35]. The details of the linear model formulation, the system identification method, and the switching linear MIMO model-based design are illustrated in Part I of this thesis.

Linear model-based controller designs have certain limitations when applied to the Peltier-based device. To obtain fast transitions using linear controllers, usually higher gains to generate large control signals are designed which on the other hands may lead to large overshoots and subsequent oscillations at the end of each step change. Large overshoots in temperature are undesirable because they can reduce the activity of the Taq polymerase (enzyme necessary for PCR) and while the subsequent oscillations will extend the settling time, thus forcing the designer to suppress oscillations by using slow transitions. Slow transitions, on the other hand, are also undesirable since they increase the overall test time, thus defying the goal of rapid microfluidics-based medical diagnostics. Therefore, achieving the trade-off between the opposing constraints on overshoot and transition time based on linear models will be difficult and may require intensive tuning by trial-and-errors. In addition, slowing temperature increasing (or creeping) of the heat sink and other nonlinear phenomena of the Peltier device are not accounted for in the linear models. Other techniques such as look-up tables may be required which will increase the tuning effort. Furthermore, linear controllers are designed based on linear models identified at specific operating regions. When the set-point changes, the same controller parameters may not achieve the desired performance and new system identifications may be required, which will hinder the extensions of the Peltier-device to other temperature settings. To overcome these intrinsic limitations, we consider to develop a theoretical model for the two-stage Peltier-based device and design nonlinear model-based controllers to improve the transition performance and

reduce the tuning efforts.

To the best of the author's knowledge, there is no nonlinear model of multi-stage Peltier devices available for controller design. Developing a nonlinear model will be crucial for the feasibility of nonlinear model-based controller design. The thermoelectric phenomena of individual Peltier modules and the thermodynamics of the interfacing materials in equilibrium are studied, and a nonlinear MIMO state-space model for our two-input-two-stage Peltier device is developed by first principles [31]. In this nonlinear model formulation some model parameters are temperature (state)-dependent. Mathematical functions from manufacturer's specifications and empirical rules are used to calculate these temperature-dependent parameters. Some model simplifications and parameter approximations are further applied to some parts of the nonlinear dynamics for the convenience in both model simulation and controller designs. Open-loop and closed-loop experiments are used to obtain model parameters and the comparisons of the model outputs and the experimental data validate the effectiveness of the nonlinear model.

The developed model of the Peltier device is not affine on control, instead the model is affine on both u and u^2. Various nonlinear controllers designed for nonlinear affine on control system cannot be directly applied to this type of system. However, this model is in strict feedback form, which can be partially decoupled. Therefore, the MIMO controller design problem can be transformed to a few sequential SISO designs. Through the changing of variable on the control signal of each SISO sub-system, a nonlinear sequential design is proposed which extends the conventional input-to-state feedback linearization method to a class of nonlinear systems that is not only affine on u but also affine on u^2. An equivalent algorithm to the feedback linearization controller is also developed through the Lyapunov stability theory to analyze the parameter variation ranges. Simulation results show improved transition performance with faster settling time and much smaller temperature variation range than the switching decentralized PID controller design in [35]. No discernable overshoot and steady-state errors are observed in the top Peltier after each temperature transition, however, small steady-state errors are observed in the bottom Peltier. The possible parameter deviation levels are calculated and the

effects on the closed-loop performance due to model parameter deviations are studied in simulation. A local high gain proportional controller is proposed to be added on the feedback linearization-based controller to reduce the steady-state errors due to parameter mismatches [31].

To further reduce the online calculation burden at local regions and utilize integral control to minimize steady-state errors, a mixed switching nonlinear/linear controller is formulated [31]. At first, a pseudo-PID type nonlinear controller is developed, which is composed of a state feedback part, a bias term, and an extra derivative part for the top Peltier. A Lyapunov function method is used to develop a parameter algorithm for this controller. Then the parameters of the nonlinear controller at some pre-determined switching times are fixed and used as the parameters of local PI/state feedback controllers. Under this switching strategy, steady-state errors can be eliminated with the integral control in an ideal case, while online calculations of the nonlinear algorithm can be replaced with simple PI algorithm with fixed parameters at local regions. Simulated closed-loop response using this switching controller achieved the desired performance with minimized steady-state error and improved transition performance. Closed-loop simulations with model parameter deviations are also performed. Simulation results validated the robustness of the design.

These two nonlinear model-based controllers are both implemented in our microfluidic platform for PCR applications. Fast and smooth transitions with small overshoots are achieved in the top Peltier, and much smaller variation range is observed in the bottom Peltier (reduced from ± 5°C to ± 2°C), thus facilitating smooth transitions. Oscillations that appeared when using a linear PID design are eliminated, thus reducing the settling time of the top Peltier by 8-10 seconds (using ± 0.5°C as the criteria for calculating the settling time). Reduced settling time leads to faster transition, which will further reduce the overall reaction time. Also smaller variation ranges are obtained around the set-points, therefore achieving better reaction results.

1.6 Summary

In this thesis, a custom-made two-stage Peltier-base thermal device is developed in a microfluidic platform for disease diagnostic tests. The main focus here is to model the device and design controllers to achieve fast transition and precise temperature regulation, thus facilitating rapid and low-cost disease detection. In practical applications, both the linear model-based switching controllers and the nonlinear switching/ non-switching controllers can be used for PCR cycling depending on the different design and performance requirements. The linear controller is easy to design and implement but usually will have larger overshoot and more oscillation. Intensive trial-and-error tuning effort may be required if the desired performance requirement is stringent. Furthermore, linear model-based controllers are tuned for specific operating point. If the temperature reference changes, new model identifications and controller parameter calculations may be required. On the contrary, the two nonlinear controllers utilize the nonlinear model information and therefore can achieve better transition performance while minimizing the tuning effort. These two controllers can be also used for other reference tracking applications beyond PCR without further tuning or re-modeling. Therefore, nonlinear controllers are preferred if the device is used for different thermal applications.

The rest of the thesis will be organized into two parts. Part I includes the linear system formulation, the identification-based modeling and the linear switching controller design. The theoretical modeling and the two nonlinear model-based designs are illustrated in Part II followed by the conclusions in the last chapter.

Part I

System identification-based modeling and linear switching controller design

Chapter 2

System identification-based modeling

As mentioned in the introduction, to obtain an effective controller for PCR cycling in the cancer diagnostic project in limited time, we initially considered linear system modeling and attempt to obtain multiple linear multi-input-multi-output (MIMO) models for controller designs.

2.1 System formulation

Due to the existence of the strong thermal couplings between the two Peltiers during transitions, a MIMO system formulation is preferred over SISO model formulations to better describe the interactions between different sub-systems. For the current two-stage setting, it is intuitive to choose the surface temperatures of the Peltier modules as the state variables (here the temperatures of the three copper plates in contact with the Peltier surfaces are used assuming there exists no temperature difference between the copper plate and the Peltier surface). While either the current inputs or the voltage inputs to the Peltier modules can be chosen as the input variables depending the circuit design. Many thermoelectric properties such as the *Joule* heat have direct relations with the current flows or the voltage differential. These relations are usually nonlinear. Furthermore a few other thermal properties such as thermal conductance or thermal resistance are nonlinear functions of the temperatures. These parameters will vary as the temperatures change during the transitions. Therefore, the Peltier-based device is nonlinear in general. A state

space model of the system can be formulated in the following form,

$$\begin{aligned} \dot{x} &= f(x, u, \theta(x), d), \quad x \in R^3,\ u \in R^2,\ \theta(x) \in R^6,\ d \in R \\ y &= x + n, \quad y, n \in R^3 \end{aligned} \tag{2.1}$$

Here the state x_i, $i = 1, 2, 3$ and the output y_i, $i = 1, 2, 3$ represent the actual and the measured temperatures of three copper plates from top to bottom, the difference between x_i and y_i is the noise term denoted by n_i, $i = 1, 2, 3$. u_i, $i = 1, 2$ represents the input of the top or the bottom Peltier module, d is the ambient temperature in the vicinity of the heat sink, and $\theta(x)$ contains all of those temperature-dependent parameters which include the *Seebeck* coefficient S_M, the module thermal conductance K_M, and the module thermal resistance R_M. According to the *Seebeck* effect, a *Seebeck* voltage will appear between the two surfaces when there exists a temperature difference which will counteract the external voltage input and thus affecting the heat flow. The ratio between the *Seebeck* voltage and the temperature difference is the *Seebeck* coefficient whose value is a function of the temperatures. The other two module parameters K_M and R_M will affect the heat flow through the conduction and the heat generation through the *Joule* heating, which however are also functions of the temperatures. Therefore, for the two-stage device $\theta(x)$ includes six state-dependent elements and can be formulated as $\theta(x) = [S_{M1}, K_{M1}, R_{M1}, S_{M2}, K_{M2}, R_{M2}]^T$.

In the actuator implementation, the digital control signal is converted into a voltage signal which is fed as the input of bi-polar power amplifiers to generate the voltage output to drive the Peltier-module (Fig. 2.1). In the electric circuit schematics, the input $V_{in} = -V_{ref}\frac{Din}{4095}$, where D_{in} is the digital control input to a 12-bit D/A converter in the range [0,4095]. The input voltage to the second op-amp is $(\frac{D_{in}}{4095} - 0.5)V_{ref}$. The Darlington NPN and PNP power transistor pair works as a voltage follower and provides electric current to drive the Peltier. The load resistance is the Peltier resistance R_L, which is connected to the ground through a current sensing resistor R_{CS}. The relative voltage V_{out} can be approximated by $(2\frac{D_{in}}{4095} - 1)V_{ref} - V_r - V_{BE}$. Therefore the external voltage over the Peltier V_L and the current flow through the Peltier I_L can also be approximately calculated as

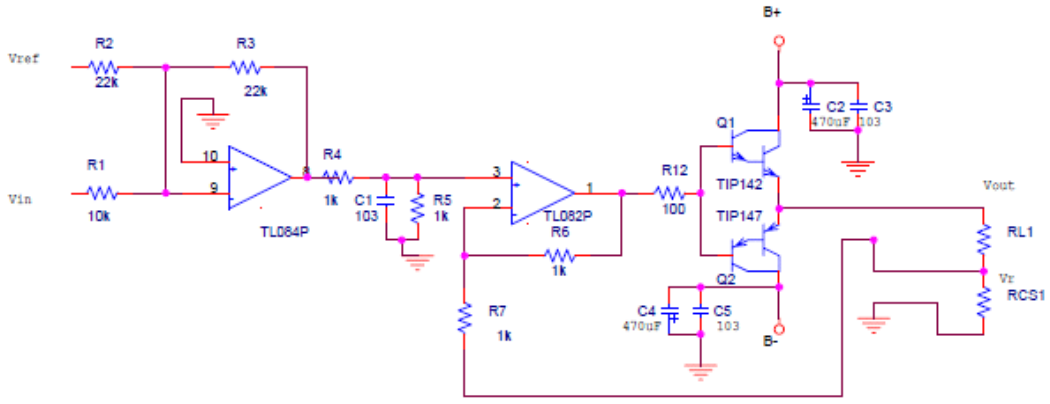

Figure 2.1: Schematic diagram of the power amplifier circuit for one channel of actuator. V_{in} is the scaled DAC output which is further amplified and shifted into a range between $\pm V_{ref}$.

follows:

$$\begin{aligned} V_L &\approx (2\frac{Din}{4095} - 1)V_{ref} - 2V_r - V_{BE} \\ I_L &\approx ((2\frac{Din}{4095} - 1)V_{ref} - V_{BE})/(R_L + 2R_{CS}) \end{aligned}$$

When D_{in} is applying some voltage to the Peltier, heat will be generated due to the *Peltier* effect which causes the temperature difference between the two surfaces of a Peltier module. The existence of a temperature difference between the two surface will cause the generation of an electric potential voltage (the *Seebeck* voltage) within the Peltier, which counteracts the external voltage V_L and reduce the current follow I_L. Therefore, the actual voltage over the Peltier or the current flow through the Peltier will slowly change as the temperature difference changes until reaching a new balance point. The relation between the D_{in} and the V_L or I_L is varying. Furthermore, due to the temperature-dependent property of the resistance of R_L, the relation between I_L and V_L is also nonlinear. Choosing I_L or V_L as the inputs will not simplify the system dynamics. Here, we choose to use to control the voltage due to the consideration on the circuit implementation.

The specifications of the Peltier module (9500/127/85B from FerroTec) used in our device is listed in Table 2.1 [11]. In our design, the maximum/minimum current input is $\pm$6.5A and the maximum/minimum voltage input is $\pm$10V, which are both

Table 2.1: Specifications of Peltier module (9500/127/85B) at T_{hot}=50°C [11]

Parameter	Description	Value
I_{max}(A)	Maximum input current at Q_c=0 and ΔT=ΔT_{max}	8.50
V_{max}(V)	Maximum DC input voltage at Q_c=0 and $I = I_{max}$	17.50
ΔT_{max}(°C)	Maximum temperature differential at Q_c=0 and $I = I_{max}$	72.00
Q_{cmax}(Watt)	Maximum heat pump capacity at $I = I_{max}$ and ΔT=0	80.00

inside the operating boundary of the Peltier module. The maximum temperature differential recorded on each Peltier during PCR thermal cycling is about 38°C, which is almost half of the maximum differential and higher thermal efficiency is achieved at this temperature differential level for this Peltier module. Therefore the current two-stage setting can achieve higher thermal efficiency in PCR application ideally if the controller can tracking the reference closely.

Although the system dynamics is nonlinear, and the relation between the digital control input and the voltage input is also varying, there exist some equivalent points for each control input (the system is stabilizable). Usually inside a small region around an equivalent point, nonlinear systems can be approximated by local linear models. Therefore, we considered to study the local models of the system.

2.2 Multiple model formulation

Multi-model approximations of the nonlinear system are commonly used in controller design, different model approximations such as the Takagi-Sugeno fuzzy model approximation [67, 5] and linear parameter varying (LPV) system [62, 63, 16] can be found in the literature. Usually in the T-S fuzzy model or the LPV model formulation, the system is assumed to be operated in a convex polytope, and the model inside the polytope can be interpolated using the linear models at the boundary vertexes. Stability can be guaranteed if the system is inside the convex polytope. Other groups considered multiple models along the non-constant trajectory [46, 48]. Two adjacent local models share some common domains therefore the system can transit from one model to another through the common domain. However, the stability of the this general multiple model system following a trajectory is difficult to prove. Some researchers studied the input-output stability problem of multiple

model systems over a stable motion and proposed to design controllers based on control-Lyapunov functions [46, 48].

According to the PCR cycling requirements, our Peltier-based device will operate between three stable equilibrium points and three transitions. It is intuitive to use the three operating points as the equilibrium points of the local models. For the transition regions, initially we consider to find the effective range of each model and use some weighted average of two adjacent models to approximate the transition. However, the derivatives of the temperature should be considered in the state to differentiate the heating and cooling regions (same temperature region but different derivative values), the weighted average approximation will be challenging. Since PCR cycling expects fast and smooth transition, usually extreme control actions will be preferred at most of the transition time, such as bang-bang control (control values set at either the maximum or the minimum). Controller designs will be focusing on the short time span at the end of the transition for smooth transition. Therefore, models at the local regions can still be utilized for controller design during the transition (larger control values will be truncated by the hardware limitation).

Focusing on the system operating in close vicinity of each local operating point $(x_{\text{ss}}, u_{\text{ss}}, d_{\text{ss}})$, the nonlinear function of parameter $\theta(x)$ in Eqn. (2.1) can be treated as a constant vector in each local region. Therefore, the system dynamics function $f(x, u, d, \theta(x))$ can be linearized locally ideally. Here, u is the digital signal D_{in}. The actual relation between V and D_{in} is included into the nonlinear dynamics. If D_{in} is far away from the value that is corresponding to zero voltage, the relation between D_{in} and V can be approximated by some linear function as $V = aD_{in} + b$. The slope a is not constant and the term b is close to the boundary of the small dead zone due to the existence of V_{BE} of the Darlington power amplifiers and the voltage drop over the current sensing resistor V_r. This could happen during the 60°C region when V is close to zero. Additional attentions are required for this region.

Without the explicit expression of the system dynamic function f, the feasibility and the modeling accuracy of linear model approximation can not be known *in prior*. Black-box system identification methods are considered to obtain local

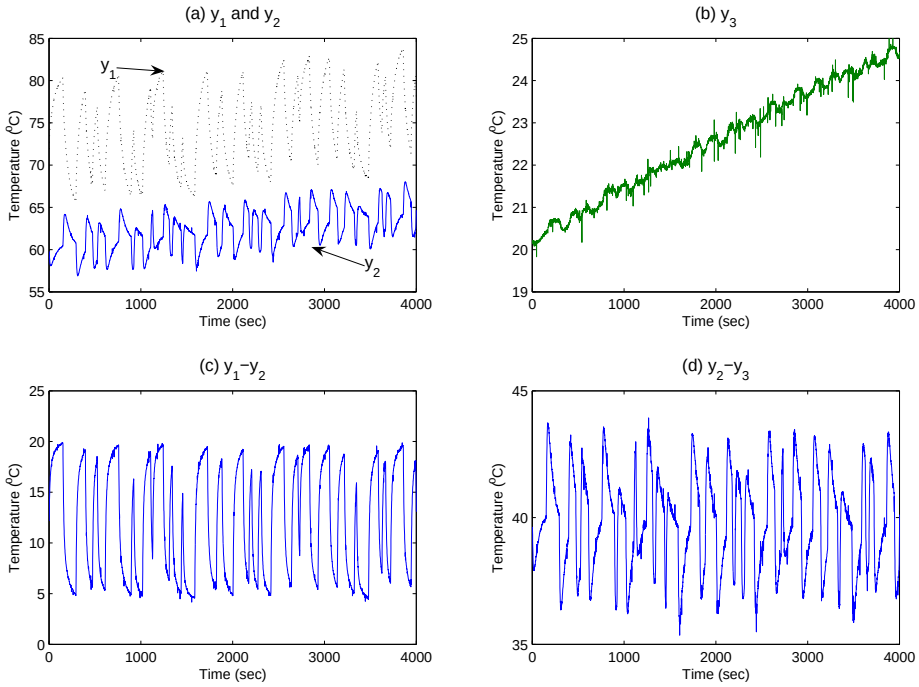

Figure 2.2: Open-loop responses at 72°C region with a standard RBS input applied to the top Peltier : (a) are the temperatures of the top sides of the two Peltier modules y_1 and y_2; (b) is the heat-sink temperature y_3; (c) is the plot of the temperature difference between the top and the bottom Peltier ($y_1 - y_2$); (d) is the plot of the temperature difference between the bottom Peltier and the heat sink ($y_2 - y_3$).

model information. Here, input/output models are chosen for system identification where the measurement noises are neglected ($y = x,\ n = 0$). Three operating points (y_{ss}, u_{ss}) are determined from experimental data. Here, u_{ss} is actually not constant which is due to the slowing rising heat sink temperature over the time. The u_{2ss} will decrease due to the increasing y_3. However, since the variation of y_3 is relatively slow compared to the change of the PCR reference, constant y_3 is assumed and so is the u_{2ss}. For each operating points, RBS tests with $(u_{1ss} + \delta u_1, u_{2ss})$ and $(u_{1ss}, u_{2ss} + \delta u_2)$ are applied separately. The open-loop responses with the RBS input applied on u_{1ss} around 72°C region are shown in Fig. 2.2(a) and (b). Slowing drifts are observed on the heat sink temperature y_3 over the operating time and small surges are observed during those extreme temperature transitions in each cycle (Fig. 2.2(b)). The y_3 value increases from 20 to 25 °C over an hour long RBS

testing. Since only natural cooling through air convection and radiation is adopted here for the heat sink, no dedicated control input is available to control the heat sink temperature, further improvement will rely on the physical design.

To remove the trend, two options are considered: (1) subtracting y_3 from both y_1 and y_2, or (2) subtracting y_2 from y_1 and y_3 from y_2. From the experimental data, it is found that the temperature difference between two sides of a Peltier module exhibits more symmetric profile around the operating point than the case with direct substraction of heat sink temperature. Fig. 2.2(c) and Fig. 2.2(d) show the responses of the two temperature differences. Furthermore, a few heat phenomena such as thermal conduction, heat convection and the *Seebeck* voltage are almost linearly dependent on the temperature difference between the two sides of a Peltier (here these temperature-dependent coefficients are assumed constant within a small local region). Choosing the temperature difference as the new fictitious system outputs is expected to achieve better linear approximation results. Therefore, the second option is chosen and a new linear local model using the temperature difference of each Peltier as the output is derived as follows,

$$\Delta y = \tilde{G}u = \begin{bmatrix} \tilde{G}_{11} & \tilde{G}_{12} \\ \tilde{G}_{21} & \tilde{G}_{22} \end{bmatrix} u. \tag{2.2}$$

where $\tilde{G}$ is a 2×2 transfer function matrix, the non-controllable term y_3 does not appear explicitly. The actual output can be calculated from the difference model as

$$\begin{aligned} \begin{bmatrix} y_1 - y_3 \\ y_2 - y_3 \end{bmatrix} &= \begin{bmatrix} y_1 - y_2 + y_2 - y_3 \\ y_2 - y_3 \end{bmatrix} \\ &= \begin{bmatrix} \tilde{G}_{11}u_1 + \tilde{G}_{12}u_2 + \tilde{G}_{21}u_1 + \tilde{G}_{22}u_2 \\ \tilde{G}_{21}u_1 + \tilde{G}_{22}u_2 \end{bmatrix} \\ &= \begin{bmatrix} \tilde{G}_{11} + \tilde{G}_{21} & \tilde{G}_{12} + \tilde{G}_{22} \\ \tilde{G}_{21}u_1 & \tilde{G}_{22}u_2 \end{bmatrix} \begin{bmatrix} u_1 \\ u_2 \end{bmatrix} \\ \begin{bmatrix} y_1 \\ y_2 \end{bmatrix} &= \begin{bmatrix} G_{11} & G_{12} \\ G_{21} & G_{22} \end{bmatrix} u + \begin{bmatrix} 1 \\ 1 \end{bmatrix} y_3 \\ &= \begin{bmatrix} \tilde{G}_{11} + \tilde{G}_{21} & \tilde{G}_{12} + \tilde{G}_{22} \\ \tilde{G}_{21} & \tilde{G}_{22} \end{bmatrix} u + \begin{bmatrix} 1 \\ 1 \end{bmatrix} y_3, \end{aligned} \tag{2.3}$$

where y_3 is treated as a fictitious input.

Although this model from (u, y_3) to (y_1, y_2) is expressed in the linear transfer function form, the existence of different delay times in the two transfer functions in

the first row of the transfer function matrix may destroy the linearity. If the delay time is negligible compared to the time constant of the model, it can be discarded in the summation operation. If the delay time is relative large, other approximation techniques may be used to approximate the summation.

2.3 System identification results

Many linear and nonlinear black-box identification techniques (e.g. linear and nonlinear ARX (Auto Regression with eXternal input) models, subspace identification, and Hammerstein-Wiener model [44]) can be implemented using commercial software toolboxes. However, the choice of model structure depends on both the system dynamics and the experimental data sets. In our case, due to the non-controllable heat sink temperature y_3, the actual u_{2ss} value may be different in each cycle. In addition, during the transition under extreme heating/ cooling conditions, the Peltier system is operated far away from the steady state, and the input to output relation is not one-to-one mapping (y and u are different between the heating and the cooling). Furthermore, the control inputs at many cases reach the hardware limitations to achieve maximum heating or cooling, where no δu can be applied to the boundary input signals. For these reasons, we focus on the system in a small range around some local stabilization points and attempt to identify three temperature difference models as in Eqn. (2.2).

For the RBS signals, magnitude and frequency are two main considerations of the input signal design. An empirical rule of using [0.01, 0.05] of the Nyquist frequency as the frequency for the RBS data is chosen and a unit RBS signal with 4000 data length is generated whose values are either +1 or -1. Generally speaking, the magnitude of the excitation signal should be chosen to be small enough to minimize nonlinear effects while to be sufficiently large to minimize the noise effect [24]. For our Peltier device where exists a small dead zone around the zero input to the Peltier due to the power amplifiers, special considerations are required for the 60/60°C region. The range of u is [0,4095] which is the input to a 12-bit D/A IC chip and the digital value for the zero voltage input is about 1830-1850.

Next we apply different δu magnitude such as 100, 200, 300, 400 to some local u_{ss} and found that δu =200 can avoid the dead zone while still achieving the balance between the model approximation range and the accuracy at the 60/60°C region. For consistency, we also choose the same δu =200 for the other two regions for generating RBS signal. Due to the uncontrollable y_3 values, the steady-state values of u_i may be different at different runs. Before applying the RBS input, some stabilizing controllers are used to reach the target x_{ss}. After the initial warmup of the bottom Peltier to 60°C, two PI controllers are used to stabilize the Peltier modules to the target temperatures x_{ss}. When the steady state is reached (variation is very small), the arithmetic average of the last 20 input values is used as the actual u_{ss} and the RBS signal is applied on top of the u_{ss}. Here, we choose to only apply an RBS signal in one Peltier while maintaining constant control input in the other Peltier. Two sets of data are collected for every RBS input.

Applying various discrete-time model structures and continuous-time models on the RBS response data, different model approximation results are obtained. The model approximation with the highest accuracy is achieved with DT ARX models. The typical DT ARX model has the following structure

$$\begin{aligned} A(q)y(k) &= B(q)u(k-n_k) + e(k) \\ A(q) &= 1 + a_1 q^{-1} + \cdots + a_{n_a} q^{-n_a} \\ B(q) &= b_1 q^{-1} + \cdots + b_{n_b} q^{-n_b} \end{aligned}$$

where q is the delay operator, n_a is the number of poles, n_b is the number of zeros plus 1, and n_k is the input-output delay denoted in the number of samples [44]. For each element of the 2×2 system, the corresponding model orders and I/O delays $[n_a, n_b, n_f]$ for the ARX model are [4,4,1]. The model fit rates using ARX models for different regions are between 93-99%. Here, the fit is the percent of the output variation that is explained by the model, which is calculated as,

$$fit = \frac{(1 - ||y_{data} - y_{model}||_2)}{||y_{data} - \text{mean}(y_{data})||_2} \times 100\%$$

where y_{data} is the output of the validation data and y_{model} is the model output. mean(y_{data}) is the average of the validation data and $||\cdot||_2$ is the 2-norm of a sequence. The above 90% fit percentage results validated that the designed RBS input

can excite the system sufficiently for identification with the high model accuracy. Some complicated input signals such as pseudo-RBS or inverse repeat pseudo-RBS are not further considered since the current modeling approximation results are good enough for controller design. Although usually discrete time models can obtain the higher modeling accuracy from the sampled data, continuous parameter models are easier for controller design. Furthermore, using a CT model-based controller, no further model identifications are required when the sampling time is changed. Also CT model structures used for system identification are usually lower order transfer function models with fewer parameters. However, the simplicity of the model is probably associated with limitations on the model accuracy. The feasibility of CT model identification needs to be verified with specific experimental data.

Transfer function models of each sub-system are to be determined first. Here, the candidate models are limited to only first order, second order, third order transfer models for simplicity in model-based controller design. Step inputs are applied to each input of the device and the step responses are used to determine the model order and structure. By comparison, the first order with delay model is chosen for the two diagonal elements, and the second order with left-half-plane zero and delay model are chosen for the off-diagonal elements. The diagonal and off-diagonal elements of $\tilde{G}$ are expressed in Eqn. (2.4) and Eqn. (2.5) respectively.

$$\tilde{G}_{\text{diag}}(s) = \frac{K}{1+T_{p1}s}e^{-T_d s}, \tag{2.4}$$

$$\tilde{G}_{\text{off}}(s) = \frac{K(1+T_z s)}{(1+T_{p1}s)(1+T_{p2}s)}e^{-T_d s}. \tag{2.5}$$

K, T_{pi}, T_z, and T_d are the system gain, the pole related time constant, the zero related constant and the time delay. The appearance of the left-half-plane zero term in $\tilde{G}_{\text{off}}$ partially accounts for the inverse response observed in step response, which is mainly caused by the interaction between the two Peltier modules.

Prediction Error Method (PEM) tool from MATLAB is applied to the first half of RBS data, and the other half of data is used for validation. The three local linear

difference models obtained from system identification are listed below:

$$\tilde{G}_{60} = \begin{bmatrix} \frac{0.02213}{35.54s+1} & \frac{-1.44s-0.001568}{727.5s^2+78.45s+1}e^{-1.41s} \\ \frac{-0.5469s+0.0001738}{578.8s^2+76.67s+1}e^{-1.11s} & \frac{0.03677}{24.81s+1} \end{bmatrix}, \quad (2.6a)$$

$$\tilde{G}_{72} = \begin{bmatrix} \frac{0.03438}{17.35s+1} & \frac{-1.031s-0.001137}{563.2s^2+68.57s+1}e^{-1.34s} \\ \frac{-0.7407s+0.001507}{488.4s^2+65.61s+1}e^{-0.757s} & \frac{0.03537}{27.05s+1} \end{bmatrix}, \quad (2.6b)$$

$$\tilde{G}_{94} = \begin{bmatrix} \frac{0.03167}{29.74s+1} & \frac{-2.386s+0.003143}{1054s^2+138.7s+1}e^{-1.77s} \\ \frac{-0.5309s+0.076240}{471.0s^2+66.01s+1}e^{-0.557s} & \frac{0.03668}{29.86s+1} \end{bmatrix}. \quad (2.6c)$$

To validate the effectiveness of the model on approximating the actual temperatures, we further constructed the Peltier system as Eqn. (2.3) in Simulink®. Measured y_3 is used as an additional input, and the time delays in each sub-blocks of the transfer function are implemented using input-out-delay modules. The simulated open-loop model outputs using the validation data are shown in the following group of figures. Fig.2.3 and Fig.2.4 are the results with the RBS input applied around the 60/60°C region. Fig.2.5 and Fig.2.6 are the results around the 72/60°C region, and Fig.2.7 and Fig.2.8 are the results around the 94/60°C region respectively.

The open-loop model simulation results show that model fit rates around different regions are more than 88%. The highest modeling accuracy is achieved at the 72°C region where the fit rate is 95%. The worse modeling accuracy is obtained in the u_1 to y_2 subsystem at the 94°C region where the fit rate is 88%. Although higher order process models could be used to improve the modeling accuracy, we prefer to keep the consistency in model structure for all three local regions. The simulated model output results around the three operating points validated the feasibility of using the intermediate linear temperature difference model to approximate the nonlinear system.

2.4 Summary

The two-stage Peltier-based device is formulated in the state-space form, whose dynamics is highly nonlinear. Multiple linear local models are used to approximate the system. A two-step linear modeling method is chosen in which linear temperature difference models are identified and the actual temperature models are constructed from the intermediate models. Continuous-time transfer function models are obtained for each element of the 2×2 difference model. Simulation results verified

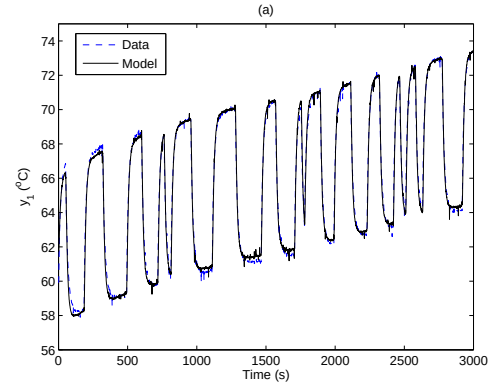

Figure 2.3: Model validation results at 60 ^oC region with an RBS input applied to u_1: (a) y_1 ; (b) y_2; (c) u_1.

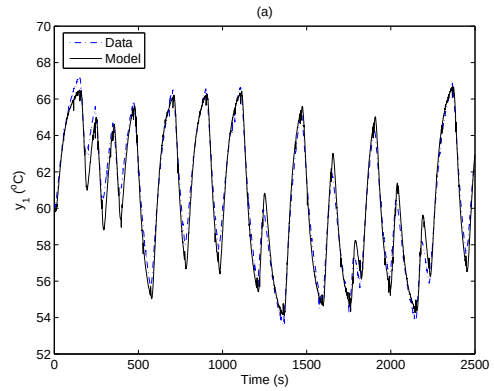

Figure 2.4: Model validation results at 60 ^oC region with an RBS input applied to u_2: (a) y_1 ; (b) y_2; (c) u_2.

the feasibility of this modeling method with acceptable approximation accuracy. Although not achieving the highest modeling accuracy, low-order continuous-time models are preferred over other discrete-time models for the convenience in controller design.

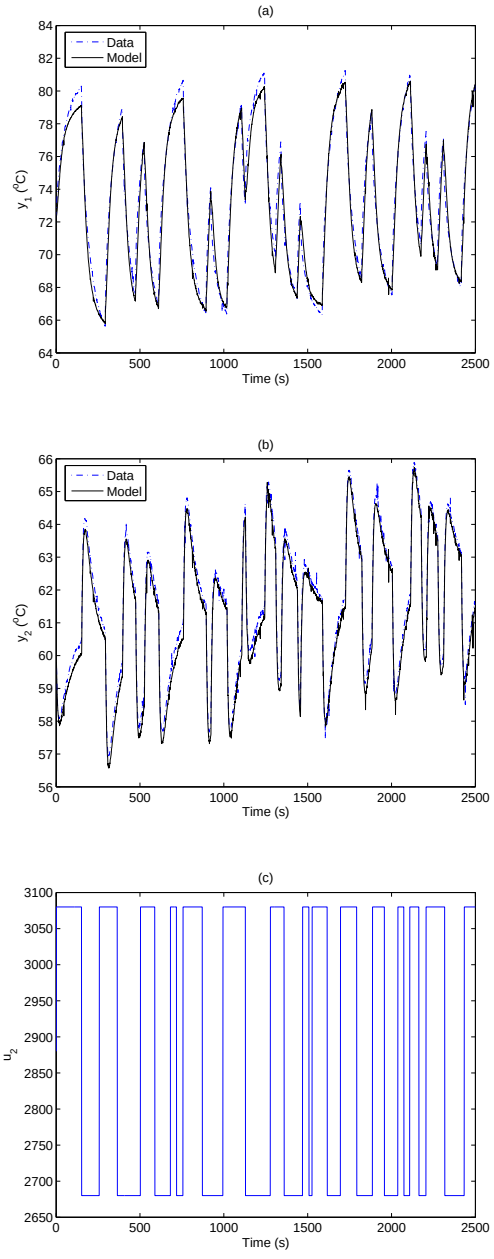

Figure 2.5: Model validation results at 72 ^oC region with an RBS input applied to u_1: (a) y_1 ; (b) y_2; (c) u_1.

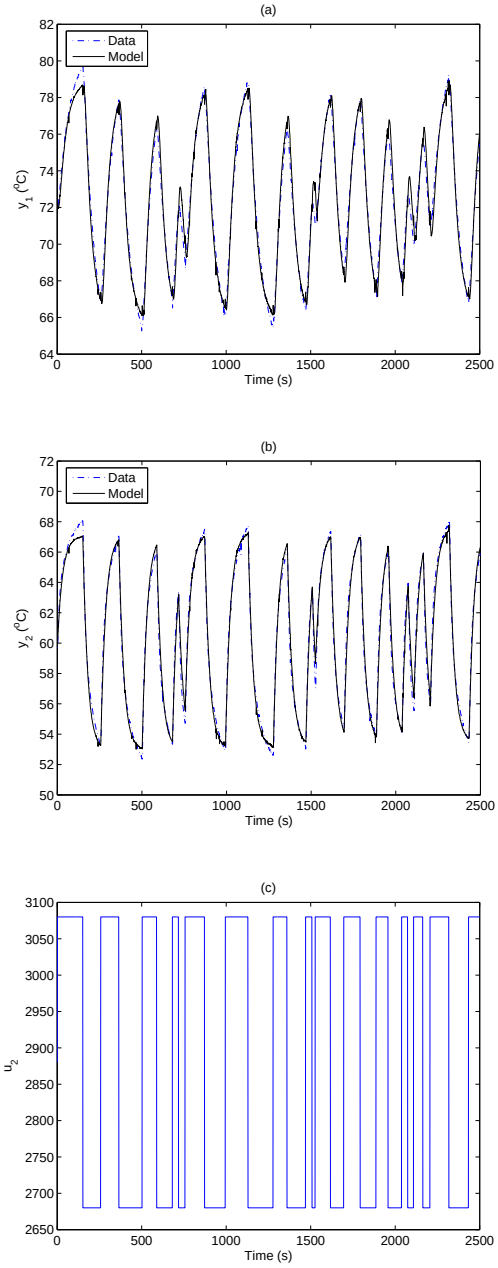

Figure 2.6: Model validation results at 72 ^oC region with an RBS input applied to u_2: (a) y_1 ; (b) y_2; (c) u_2.

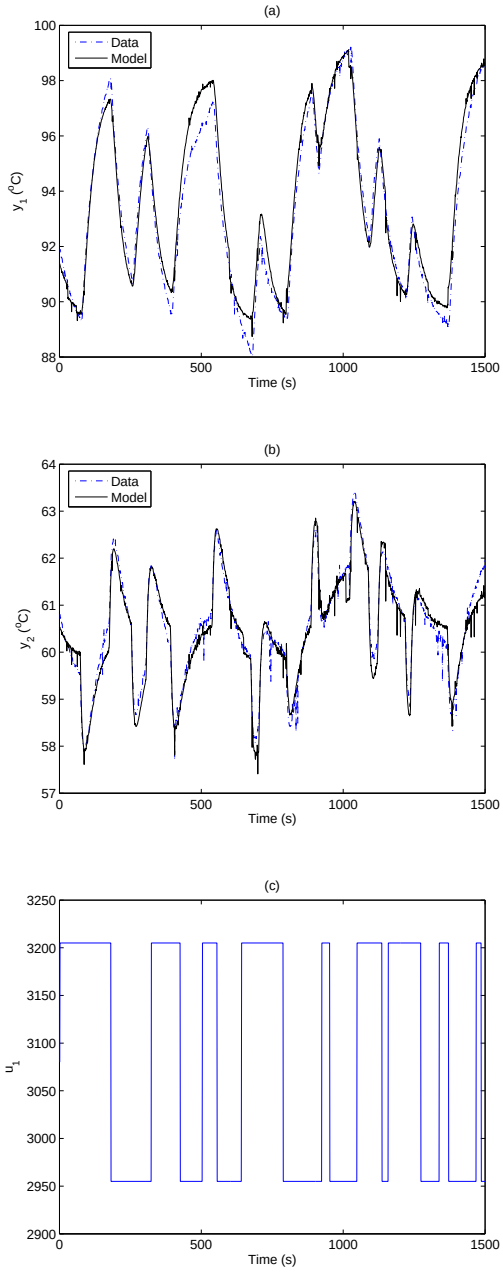

Figure 2.7: Model validation results at 94 ^oC region with an RBS input applied to u_1: (a) y_1 ; (b) y_2; (c) u_1.

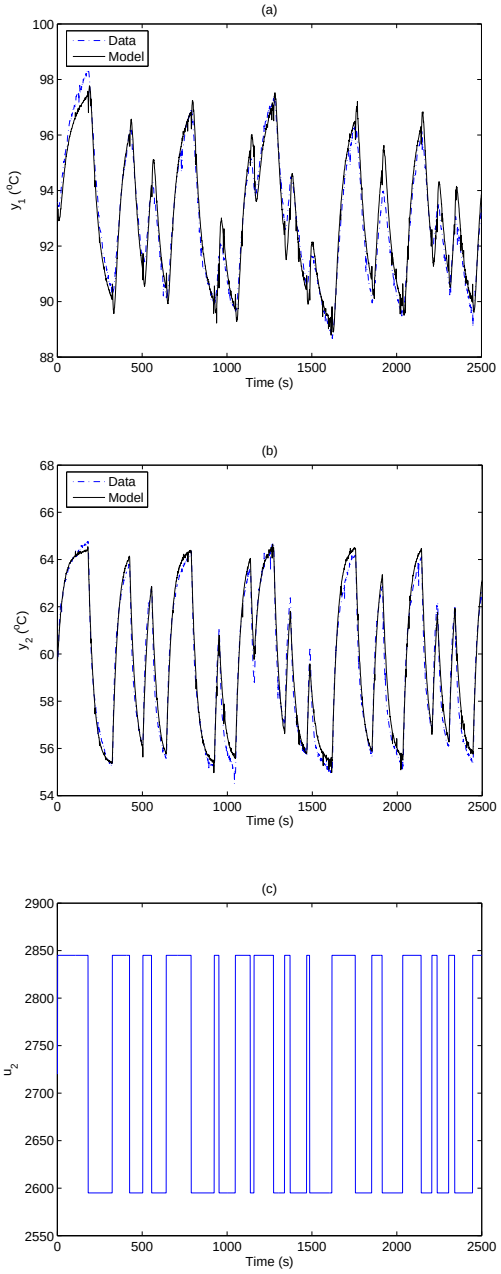

Figure 2.8: Model validation results at 94 ^oC region with an RBS input applied to u_2: (a) y_1 ; (b) y_2; (c) u_2.

Chapter 3

Switching PID controller design

In the previous chapter, three linear MIMO temperature difference models are identified in the continuous-time input/output transfer function formulation. The complete model from input to temperature output is obtained by the summation operation. Although, the existence of different delay times in the transfer functions can be realized in simulation, to obtain a new transfer function from the direct summation will require further approximation. The approximated model will be used for the local controller design. For the transition regions, there is no single local model or any combinations of multiple local models can approximate the system because of the strong nonlinearity during the transition. However, the input signal during most of transition time is set at the maximum heating or cooling value. The design problem will mainly focus on the smooth transition at the end of the transition. Therefore, local models at the target set-point could be used for controller design for the top Peltier. Based on these system operating characteristics, a switching controller design is considered here for tracking a typical PCR temperature profile.

For the switching design, naturally we could divide one PCR cycle into six sub stages as shown in Fig. 3.1. Here, we isolated the first heating transition from 60 to 94°C and denoted it as “transition 0” as it is different with other cycles. Therefore, the beginning of a regular cycle is set at the start of the local region at 94°C and the end of a cycle is set at the end of the transition from 72 to 94°C. Other partitions can also be used depending the controller design. For every local regions and transitions, different controllers are designed.

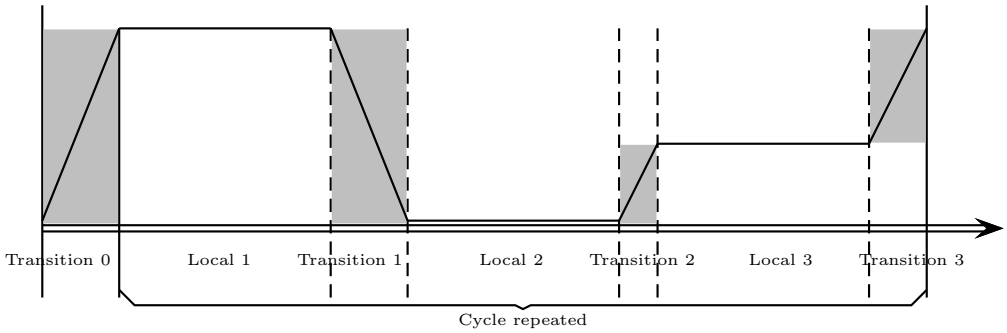

Figure 3.1: Partition of the operating regions of a PCR cycle for a switching design. The first heating region is denoted by "transition 0" and is excluded from regular cycles; A regular cycle has three local regions each followed by a transition region (grey areas).

3.1 Controller design in local regions

3.1.1 Characteristics of local linear models

As mentioned earlier, the transfer function from the summation of two transfer functions with different delay times is approximated for controller design. Lower order $Padé$ approximations are used to approximate the delays. Normally, the new transfer function will be higher order as the two transfer functions usually have different poles and zeros. Therefore, further model order reduction may be necessary depending on the choice of controller designs.

Next, we study the strength of the coupling based on the steady-state gains of the approximated MIMO model using the relative gain array (RGA) matrix. The RGA matrix was introduced by Bristol, and is used to measure the coupling of a MIMO system at steady-state [65]. For a square non-singular matrix A, the RGA(A) is defined by

$$\text{RGA}(A) \triangleq A \times (A^{-1})^T$$

where the operation "$\times$" denotes element multiplication (Schur product). Most of the properties of the RGA matrix follow directly if we write the RGA-elements in the following form,

$$\lambda_{ij} = a_{ij} \cdot \tilde{a}_{ji} = (-1)^{i+j} \frac{a_{ij}\ detA^{ij}}{detA}$$

where $\tilde{a_{ji}}$ denotes the *ji*th element of the matrix A^{-1}, A^{ij} denotes the matrix A with row i and column j deleted. "det" is the determination operation. Many properties of the RGA matrix can be found in the literature [65]. For the 2×2 system we studied here, the calculation of the elements of the RGA matrix can be simplified due to the property that the summations of elements of every row or column are always equal to one. We only need to calculate the $(1,1)$ element (λ_{11}) of our 2×2 RGA matrix and obtain other elements from λ_{11}. The corresponding λ_{11} values of the RGA matrices of three local models at steady-state are 1.0075, 1.0424, and 1.2669 respectively for 60, 72 and 94°C regions. From the RGA matrix theory, if $\lambda_{11} = 1$, the system is totaly decoupled, the closer the value is to one, the less the coupling interaction. Therefore, with λ_{11} values close to one at the 60 and 72°C regions, the couplings are not significant at close vicinity of these local operating regions. A larger value of λ_{11} is found at the 94°C region, which means the coupling is stronger than the other two regions. However, for the λ_{11} ≈1.25 (which is relative close to unity), the strength of coupling is not significant and we can still apply decentralized designs.

For each identified local MIMO model, various MIMO controller designs can be applied, such as MIMO IMC design, MIMO H_∞ design. By transforming the transfer function matrix into a state-space formulation, other optimization based robust controller design can also be applied locally. However, the optimal controllers usually have higher order of dimension, which will need large memory space and complicated matrix operations. Therefore the implementation of these higher order controller in micro-controllers with limited memory space may be difficult. Therefore, local decentralized PID controller designs are preferred.

3.1.2 Review of PID controller designs

Proportional-Integral-Derivative (PID) controller design is the most-used controller design in industry, which has a simple structure and a small number of parameters. Furthermore, in many advanced control designs, PI controllers are also used as the lower level controllers [1].

One of the reasons of the widespread applications of PID design is the conve-

nience for non-control experts to use with various simple and easy to implement design rules. Specific PID designs usually depend on specific system models, both in transfer function form or state-space form. Commonly used transfer function models for PID designs are summarized in Table 3.1.

Table 3.1: Typical lower order plant models used in PID design

Transfer function models	Description
$G_1(s) = \frac{K}{sL}e^{-sL}$	1st order pure integrator model
$G_2(s) = \frac{K}{1+sT}e^{-sL}$	1st order model with delay
$G_3(s) = \frac{K}{(1+sT)^2}e^{-sL}$	2nd order model with identical poles
$G_4(s) = \frac{K}{(1+sT_1)(1+sT_2)}e^{-sL}$	2nd order model with different real poles
$G_5(s) = \frac{K}{s(1+sT)}e^{-sL}$	2nd order model with one pole at origin
$G_6(s) = \frac{K\omega^2}{s^2+2\zeta\omega s+\omega^2}$	2nd order model with different complex poles

K is usually the system gain, T is the time constant, and L is the delay time. Many earlier design rules are developed for SISO lower order transfer function models such as the pure integrator model with delay (G_1), the first order model with delay (G_2) or without delay, the second order model with identical poles (G_3) or different poles with delay (G_4). Other variants of 2nd-order models including the second order model with delay and with one pole at the origin (G_5), and the second order model with two complex poles (G_6, whose poles are $-\zeta\omega \pm \ i \ \sqrt{1-\zeta^2}\omega$) can be also found in some applications. Corresponding PID parameter values are obtained from these model parameters from empirical rules.

The first available PID design rule is proposed by Ziegler and Nichols in 1942,

which is an open-loop design and has two classical methods based on either the time-domain response or the frequent domain response. The time domain rule is based on the step response, which assumes that the system is a first order model with time delay as $G_2(s)$. The plant model parameters such as T and L can be obtained from the step-response, and the relations between the PID parameters to the model parameters are provided. The second Z-N rule is a frequency response method, in which magnitude and frequency are obtained from the response to determine the controller parameters. These two methods usually generate different parameter values due to the different objectives and have their own application regions.

Another group of PID tuning techniques is developed based on the closed-loop loop-shaping technique, which includes the loop shaping designs based on minimizing some integral of errors, λ-tuning, pole-zero cancelation etc. [1]. By extending the pole-zero cancelation idea to the cancelation of the entire system model, internal model-based (IMC)-PID controller is developed where the inverse of the system model and a filter are introduced into the controller to cancel the plant model and obtain exact tracking in an ideal case [58]. The idea of the internal model-based controller is illustrated in Fig. 3.2 [20, 21]. The initial design idea appears as the block diagram in Fig. 3.2(a), where an approximated plant model $\tilde{P}$ is introduced and only the error between the system output and the model output is used in the feedback loop. The block diagram in Fig. 3.2(b) shows the equivalent system of the internal model design in the traditional unit negative feedback formulation where the controller in the forward path is composed of an internal feedback loop [20]. If the approximated model $\tilde{P}$ in Fig. 3.2(a) equals to the actual model P, the error is always zero, and the feedback loop is cutoff. Then the transfer function is PQ. By choosing $Q = P^{-1}$, we can achieve step tracking and disturbance rejection. This is the extension of the zero/pole cancelation idea to the exact model cancelation. Usually the plant model P is strictly proper, the inverse of P has higher order in the numerator than the denominator, therefore some filter block is introduced to obtain proper or strictly proper Q. When implementing the internal model-based controller, we would like to formulate a single controller in the forward path as C,

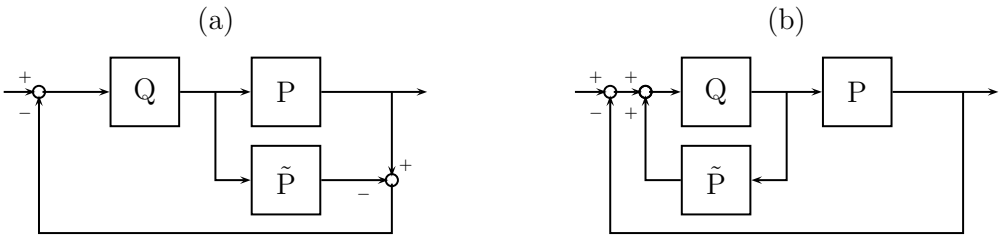

Figure 3.2: Illustrative block diagrams of internal model-based controller design: (a) The block diagram of internal model control design; (b) An equivalent block diagram of conventional feedback control. P is the plant model, $\tilde{P}$ is the approximated plant model, Q is the intermediate controller. The internal feedback loop composed of Q and $\tilde{P}$ in (b) can be viewed as a new controller in forward path.

the expression of C can be derived using the block diagram in Fig. 3.2(b) as,

$$c(s) = \frac{q(s)}{1 - \tilde{p}(s)q(s)}, \text{ if } q(s) \neq \tilde{p}^{-1}(s) \tag{3.1}$$

Depending on the plant structure, such as whether there are right-half plane zeros, first order or second order models, etc., different filter transfer functions with a tuning parameter λ are used in obtaining the intermediate controller Q as,

$$q(s) = \tilde{q}(s)f(s), \quad f(s) = \frac{1}{(\lambda s + 1)^n} \tag{3.2}$$

For a group of specific plant models, by choosing some appropriate intermediate controller $\tilde{q}$ and filter f, we can obtain the corresponding controller $c(s)$ in standard PID controller structure. Typical SISO plant models and the corresponding IMC-PID controllers are summarized in [58]. From the IMC design theory, if $\tilde{P}$ is the exact model, the closed-loop achieves perfect tracking. However IMC based rule may result poor closed-loop performance in some load disturbance scenarios when some canceled poles are slower compared to dominate poles. Also for system with delay or high-orders, model approximations are usually required.

Similar to the loop-shaping based PID rules, a new group of rules is proposed based on minimizing some user defined performance objective by optimization. To derive the analytical solution of the optimization method, the system models can not be too complicated. Also some rules based on pole placement or dominant pole designs are proposed in the literature [1].

PID rules for multi-variable system are also developed in the literature, in which the system is formulated as a state-space model. To design a PI controller in state-space formulation, the integral part of the controller usually is treated as a new augmented state. In [29], the parameters K_p and K_i of a PI controller are formulated as the output feedback gain matrix, and designed by LQR/LTR loop shaping technique.

3.1.3 Internal model-based PID controller design

Considering the characteristics of the identified local models and the convenience of implementing a switching strategy, we choose to use decentralized IMC-based PID controllers for the local stabilization. The feasibility of decentralized design relies on the observed results that the λ_{11} elements of all three RGA matrices are relatively close to unit. The choice of IMC rules are two fold. First, the IMC-PID controller can be used on wider plant models than traditional Ziegle-Nichols rule-based design, and it has the additional filter block to smooth the noise effect. Secondly, due to the essential design logic to exactly cancel the plant, IMC-PID rule-based controller usually have superior closed-loop reference tracking performances.

Here Padé approximations of the time delays are used to derive the summation operation. The obtained transfer function G_{11} and G_{12} are usually higher orders. For the diagonal terms, we considered to further reduce the model order. G_{11} into A second order model $G_{11\text{a}}$ with one left-half-plane zero is proposed to approximate the G_{11} by frequency domain curve fitting. A Bode plot of the 4th order G_{11} and a 2nd order $G_{11\text{a}}$ at 72°C region is shown in Fig. 3.3. At high frequency and low frequency, both the magnitude curves and the phase curves are almost coincided. No model approximation is required for the diagonal G_{22} term as $G_{22} = \tilde{G}_{22}$. The two diagonal transfer functions of the approximated system have the following structure

$$G_{11\text{a}}(s) = \frac{K(T_z\, s+1)}{(T_{p1}\, s+1)(T_{p2}\, s+1)},\ T_z, T_{pi} > 0 \tag{3.3}$$

$$G_{22}(s) = \frac{K}{T_p\, s+1},\ T_p > 0 \tag{3.4}$$

where the subscript “a” denotes the approximated model.

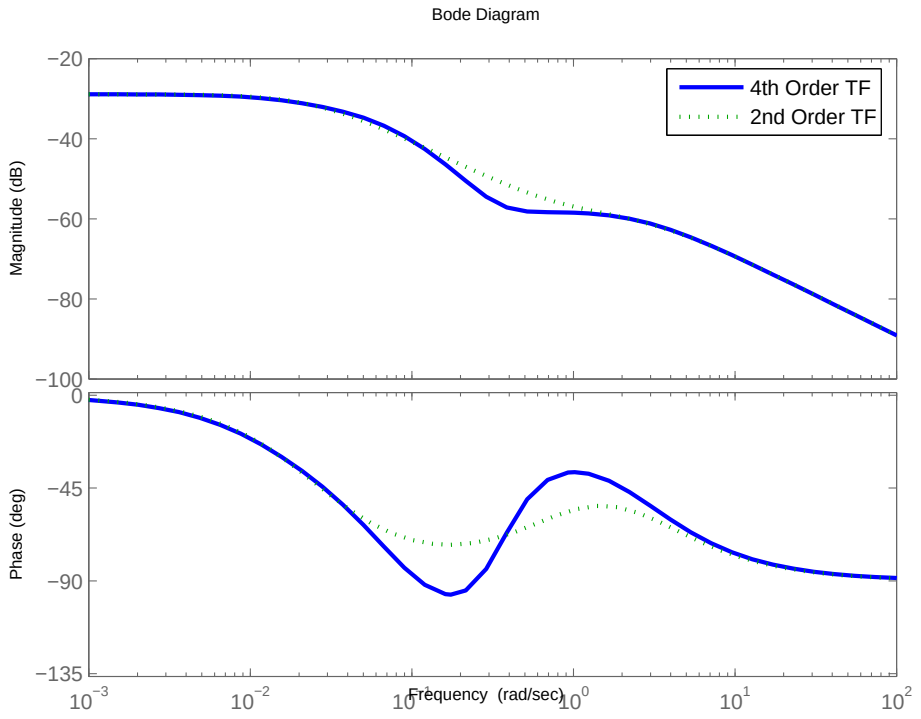

Figure 3.3: Bode plots of the original 4th order G_{11} transfer function model (solid line) and the reduced 2nd order approximated $G_{11\text{a}}$ transfer function model (dotted line) at 72°C region.

The corresponding parameters values of $G_{11\text{a}}$ and G_{22} at three operating points are listed in Table 3.2.

Table 3.2: Parameter values of the diagonal models for IMC-PID design

T (°C)	$G_{11\text{a}}(s) = \frac{K(T_z\, s+1)}{(T_{p1}\, s+1)(T_{p2}\, s+1)}$				$G_{22}(s) = \frac{K}{T_p\, s+1}$	
	K	T_{p1}	T_{p2}	T_z	K	T_p
94	0.0393	49.92	0.45	1.23	0.0367	29.86
72	0.0359	38.28	0.33	1.25	0.0354	27.05
60	0.0223	60.91	0.29	1.25	0.0368	24.81

Applying the IMC-PID rules in [58], the corresponding PID controllers can be

formulated as follows,

$$C_{11}(s) = K_c\left(1+\frac{1}{\tau_I s}+\tau_D\, s\right)\left(\frac{1}{\tau_F\, s+1}\right), \tag{3.5}$$
$$K_c = \frac{T_{p1}+T_{p2}}{\lambda K},\ \tau_I = T_{p1}+T_{p2},$$
$$\tau_D = \frac{T_{p1}T_{p2}}{T_{p1}+T_{p2}},\ \tau_F = T_z.$$

$$C_{22}(s) = K_c\left(1+\frac{1}{\tau_I s}\right),\ K_c = \frac{T_p}{\lambda K},\ \tau_I = T_p. \tag{3.6}$$

where K_c is the gain of proportional part, τ_I and τ_D are the integration constant and the differential constant, τ_F is the filter constant, λ is the free design parameter for tuning the performance in IMC structure. The designed parameters values of $C_{11}(s)$ and $C_{22}(s)$ are listed in Table 3.3.

Table 3.3: Parameter values of the IMC-PID controllers

T (°C)	$C_{11}(s) = K_c\left(1+\frac{1}{\tau_I s}+\tau_D\, s\right)\left(\frac{1}{\tau_F\, s+1}\right)$						$C_{22}(s) = K_c\left(1+\frac{1}{\tau_I s}\right)$			
	K_c	τ_I	τ_F	τ_D	λ	u_{init}	K_c	τ_I	λ	u_{init}
94	639.13	50.25	1.23	0.33	2	2950	407.05	29.86	2	2950
72	213.32	38.27	1.25	0.33	5	2350	254.93	27.05	3	2950
60	687.10	60.97	1.25	0.33	4	1950	449.75	24.81	1.5	2950

The value of the tuning parameter λ in Table 3.3 is determined by trial-and-error through simulation. Because there is no model available for the transition regions, we choose to use the local model around 72°C to simulate the system. The λ values for the 72°C region are relatively larger and the controller gains are relatively smaller compared to the other two regions. Next, we further remove the derivative term from the local PID controller. For the C_{11} controller, since $T_{p2} \ll T_{p1}$, τ_D term in G_{11a} is very small, the D term can be neglected. Therefore, three local PI controllers are designed accordingly. For the C_{22} controller, since the time constant T_p in G_{22a} at three local models are very close, only one set of PI parameters is used for all three regions. The parameters of the model for the middle temperature 72°C are chosen except different initial integrator values are set to reflect the different operating conditions. Details of the rules of the determination of initial integrator values are discussed in the transition controller design.

Since there are hardware limitations on the magnitudes of the control signal, anti-windup designs for the integral control should be considered. A conditioning scheme [39] to derive the limits of the reference signal from the bounds of the control signal is applied. All of the three reference set-points are far away from the constraints derived from the boundary conditions, therefore under normal conditions integrator windup will not happen with a local PID controller. As a preventive measure, the integrator values will be reset to the boundary value when the saturation happens.

3.2 Controller design in transition regions

As mentioned before, there is no single model available from system identification during the transition region, and only the local models at the steady-state are available. A combination of a PD controller for the top Peltier and a PI controller for the bottom Peltier is chosen and the switchings of the controllers for the two Peltier modules take effect simultaneously. For the top Peltier, the PD controller is applied before the switching whose parameters are derived based on the local model of the target temperature. For the bottom Peltier, same PI controller parameters from the local regions are used except some special initial integrator value settings to reflect the couplings. Fixed y_1 values are chosen as the switching criteria at the end of the transition, which can be essentially viewed as state-based when neglecting the measurement noise term from the output ($y_1 = x_1 + n_1$). The switching from each local region to the next transition is time-based and the time spans are determined by end-users. Therefore, the switching strategy is mixed state and time based. The choice of the critical y_1 value for switching will affect the actual transition time and the settling time after the switch. In some case with inappropriate setting, chattering around the switching y_1 value may happen, which should be avoided by careful tuning of the local controller parameters.

To determine the parameters of the PD controller before the switching, we use the controller parameters from the next local PID controller as the initial candidate. The reason is that at the earlier stage of transition maximum speed is desired,

therefore maximum or minimum control value is applied. On the other side, fast transition usually will lead to larger overshoot after transition. We choose to design the PD controller whose control values are out of the bound in earlier transition and are slowly approximating the boundary from outside. Only at very short time span before the state-based switching, the control values of the PD controllers are inside the boundary for smooth transition. K_c values of the PD controllers are set to be same as the K_c for the PI controller of next local region and further tuned with a scaling coefficient. T_D values are also obtained from the IMC-PID controllers for the next local region.

After the switching, the earlier designed IMC-PI controller is applied and the initial integrator values are reset for different local regions. We initially determine the initial integrator values from the steady-state values, and further tune them under the switching strategy by trial-and-errors in simulation. The tuning of integral values is mainly focusing on the smooth transition and the avoidance of possible chattering. By enforcing the initial integrator value to be large enough to drive the state away from the switching temperature toward the set-point temperature, the chattering could be avoided. Meanwhile, we also want to keep the control values close to the value before switching to obtain bumpless transfer. Best-tuned initial integral values of the three local controllers are listed in the Table 3.3.

Although the objective of the controller of the bottom Peltier is to maintain the temperature at the constant reference temperature, strong couplings between the two Peltiers under extreme heating/ cooling conditions should be considered. The gain values of PI controllers are always the same, while different rules of initial value setting are applied for different transition regions. For the 60 to 72°C transition with a small set-point change, only minor change on the initial integrator value is applied. For the other two transitions with larger step changes, we intentionally enforce maximum heating or cooling in the earlier transition region by setting the initial integrator values close to the boundary values. Due to the limited thermal mass of the Peltier modules, instant temperature surges in x_2 are inevitable even when extreme heating/coolings are applied in both Peltier modules. For the 94 to 60°C transition, we extended the extreme cooling in C_{22} for a longer time span to

achieve faster transition and reduce the overshoot in x_1 while sacrificing the performance in x_2. Trial-and-errors in simulation are used to determine the settings with our main objectives on the performance of the top Peltier.

3.3 Simulation results

To test the performance of the designed switching controller, the closed-loop system is simulated in Simulink® for a typical thermal cycling reference profile encountered in a PCR-based amplification reaction (94, 60, 72°C). Since there is no single identified model suitable for the transition region, we use the identified local MIMO model around 72°C for the plant simulation. The actual differences between the three local models are attributed to the uncertainties in the model parameters. In addition, since in the system formulation, there are no models to for the dynamics of the heat sink temperature y_3, a constant y_3 value is used as an input in the simulation which may affect the performance of the temperature output of the bottom Peltier. This simplification of y_3 is justified by the relatively small drifting magnitude over a few cycles and the almost negligible effect of y_3 on u_1 and x_1.

In the implementation of the switching controller, a pre-warmup stage is required before the regular PCR cycling. Since same controllers are used for the first 60 to 94 transition and the following 72 to 94 transition despite the difference of the step size, the partition can be adjusted which "transition 0" is not isolated. Instead, it is included in regular cycles as the first stage of a regular cycle. Therefore, the first transition in the first cycle starts from 60 to 94°C. In the later cycles, the first transition starts from 72 to 94°C. Although the covered temperature range is different and the transition time span is also different, the controller implementation is the same since we use state-based criteria to switch at the end of transition. The switching from local region to transition is determined by pre-set operating time span. A flowchart of the switching controller implementation is shown in Fig. 3.4.

Decentralized switching controller is applied. During the warm-up stage, fixed control inputs are used to heat the bottom Peltier to the operating temperature. After the warm-up, a PD controller is applied in u_1 and a PI is applied in u_2. For the local

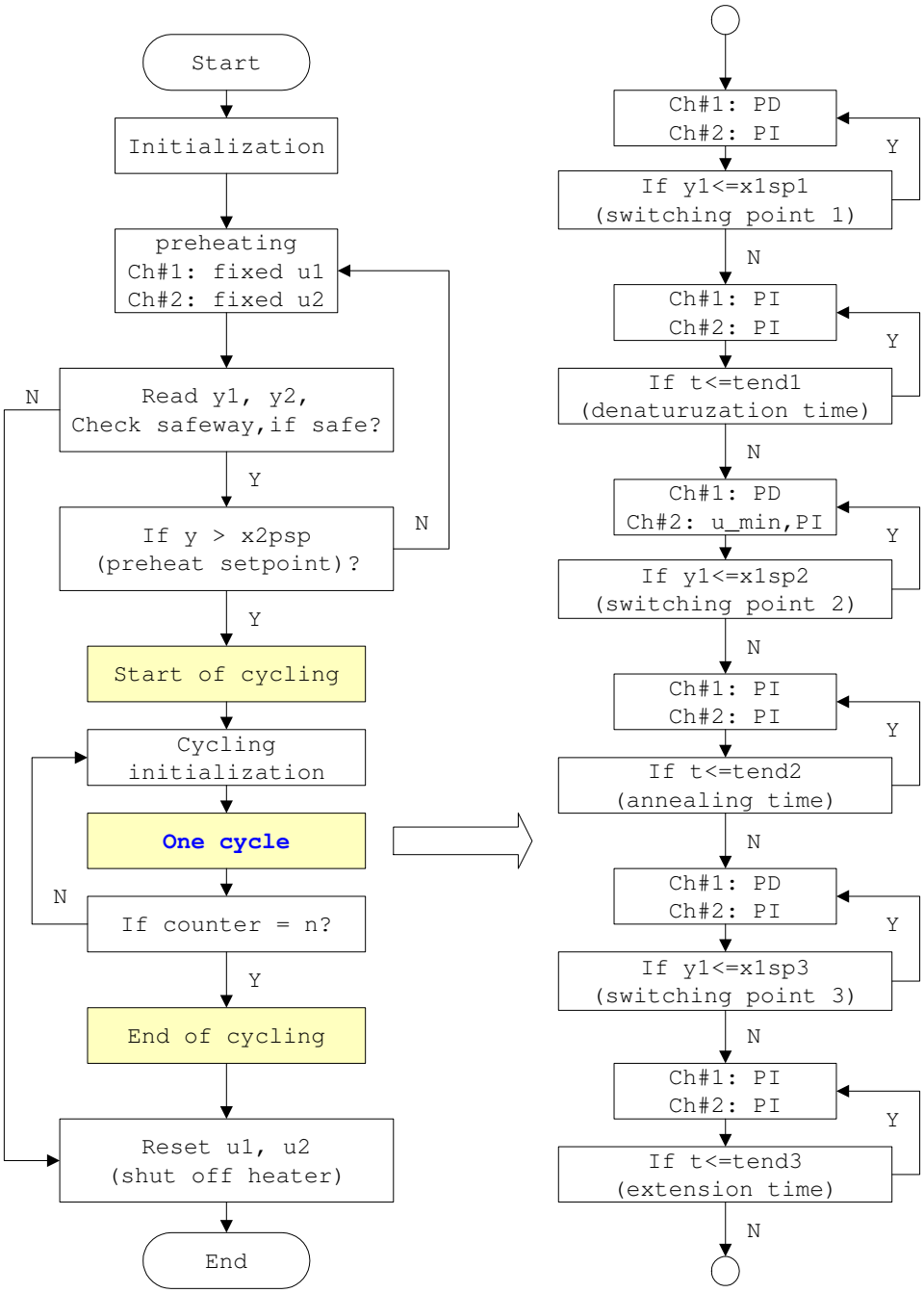

Figure 3.4: Flowchart diagram of the decentralized switching controller. The block denoted as “One cycle” represents the internal cycle which starts with a transition region until the temperature-based switching happens, the local stabilization range ends with user specified time. Three local regions are reached sequentially inside the cycle.

regions, an IMC-PI controller with a filter is applied on the top Peltier and another IMC-PI controller is applied on the bottom Peltier. To facilitate the simulation, the

filter part is implemented as a separate transfer function block.

The simulated closed-loop results using this decentralized switching controller in one cycle are shown in Fig. 3.5. Only the response of one cycle is shown here as the results of multiple cycles are same because no noise terms are added and constant y_3 is used (no drifting of heat sink temperature). For comparison, we also included the closed-loop response of a non-switching decentralized PID(C_{11})/ PI(C_{22}) controller. The initial values of integrators are based on experimental observation and trial-and-errors. From the output of y_1 in Fig. 3.5(a), a large improvement of the rise time by using the switching strategy is observed compared to the non-switching PID design. Using ± 1°C bound around the 94°C set-point as the boundary, the rise times of the non-switching PID controller and the switching PID controller are 24s and 15s respectively. For the 60°C and 72°C set-points, the rise times of the non-switching PID are larger than 20s, while the rise times of the switching controller are 14s and 11s respectively, which are almost half the rise times of the non-switching controllers. The observed improvement on rise time is as expected since maximum heating/cooling lasts longer time during the transition in the switching design. However, usually faster rise time will lead to large overshoot. By careful tuning of the switching parameters, the overshoots using the switching controller are further reduced, which are not higher than using the single non-switching controller in 94°C region in our simulation, this region is most critical for the performance of DNA amplification. At the other two regions, the overshoots are higher than non-switching cases, but still within 1°C range. This results could be partially due to the difference between the model used in the simulation (at 72°C) and the actual local model. Here, we use the simulation mainly for obtain tuning parameters and switching parameters. The relatively larger overshoot is the tradeoff of the faster rise time compared to the non-switching design. In addition, we further tune the controller of the bottom Peltier to obtain the small overshoot and fast settling time in the top Peltier while sacrificing the performance of the bottom Peltier. In Fig. 3.5(b), instant temperature surges are found in y_2 in every 94 to 60°C transition, and relatively larger oscillations in y_2 are observed after the transition which is partially due to limited thermal mass of the Peltier and our

introduced additional counter-coupling actions in u_2 (Fig. 3.5(d)). In this situation, u_2 is forced to stay in extreme cooling value for a longer time to absorb the heat from top Peltier during the cooling of y_1 to expedite the transition speed.

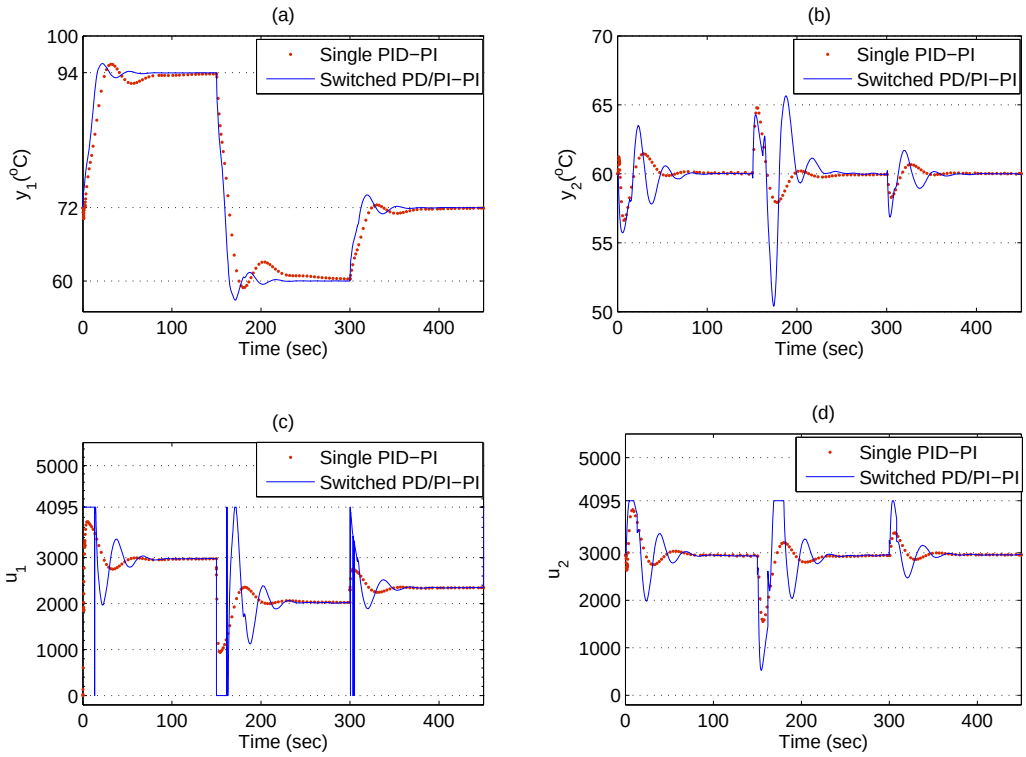

Figure 3.5: Simulated closed-loop input and output responses with two linear model-based controllers of one PCR cycle. (a) y_1; (b) y_2; (c) u_1; (d) u_2. (dot) Decentralized PID(top)-PI controller(bottom); (solid) Switching PD/PI(top)-PI/PI(bottom) controller.

3.4 Experimental results

3.4.1 PCR thermo-cycling results

The parameters of the switching controller obtained from the simulation are used in experimental set-up. Since the designed controller is continuous-time (CT) based, discretization is processed in the sampled-data system implementation. For PI controllers, the same K_c and K_c/τ_I values from the CT model can be used in the DT

controller with merely the substitution of the integral operation $\int e\,dt$ with a summation $\sum eT_s$. Our internal data sampling rate T_{s1} is 100ms which is much faster than the time constant of the plant, therefore the effect of the discretization is insignificant. For data monitoring and off-line analysis, we choose a slower sampling rate T_{s2} which is 1s and the data for system identification use the this sampling rate. Since our identification is based on the data with slower sampling rate T_{s2} while the controller implementation is based on the faster sampling rate T_{s1}, using a CT model-based controller design can circumvent the multi-rate issue and subsequently provide extra implementation freedom (such as changing T_{s1} without controller re-design).

Secondly, the first order filter introduced in the IMC design for $C_{11}(s)$ is separated with the PI controller, and realized by the weighted average of two consecutive samples, which is a simple approximation of the CT low-pass filter. Using impulse invariance design, a simple low-pass filter in continuous time can be transformed into its discrete counterpart with the same impulse response [45],

$$CT:\ H(s) = \frac{1/\tau_F}{s + 1/\tau_F} \ \Rightarrow\ DT:\ H(z) = \frac{T/\tau_F}{1 - e^{-T/\tau_F} z^{-1}}$$

Here, $H(s)$ is the CT transfer function by Laplace transform of and $H(z)$ is the DT transfer function where z^{-1} means the previous sampling instant. Replacing the $H(z)$ with $Y(z)/U(z)$, the filtered signal in time-domain can be expanded as

$$y_f(k) = \frac{T}{\tau_F} u(k) + e^{-T/\tau_F} y_f(z-1) \tag{3.7}$$

By approximation of the e^{-T/τ_F} term with $1 - T/\tau_F$, we implemented the filter on the sampled error signals using the following the formula,

$$e_f(k) = \alpha e(k) + (1-\alpha) e_f(k-1), \quad \alpha \in [0,\ 1]. \tag{3.8}$$

where $\alpha = T/\tau_F = 0.85$. In determining the value of α, $T = T_{s2} = 1$ is chosen based on the sampling rate and τ_F are obtained from simulation. Although there is no extra filter required in $C_{22}(s)$, we also apply the same filter in $C_{11}(s)$ to the measured signal of the bottom Peltier to attenuate the noise effect.

Another difference between the implementation and the simulation is the drifting observed in the heat sink temperature, while constant values are used in simula-

tion. Since the heat sink temperature y_3 is available from the measurement, y_3 value is incorporated in the controller with a pre-calculated look-up table of y_3 and u_{2ss} pairs stored in the PIC micro-controller. The corresponding u_{2ss} with different y_3 measurement will affect the initial integral values of the PI controller of the bottom Peltier at the end of a transition region.

The closed-loop performance of the Peltier-based device using the decentralized switching controller to track a typical PCR cycling profile is shown in Fig. 3.6, which includes the measured temperatures of the two Peltier modules and the heat sink over seven PCR cycles. The corresponding control values (DAC input value) are shown in Fig. 3.7. Since the reference has frequent step changes, the error magnitude during transitions will be relatively large. The temperature outputs of the top Peltier around the three set-points are shown in Fig. 3.8(a)-(c) respectively, while the temperature output of the bottom Peltier is shown in the zoomed-in range in Fig. 3.8(d). The target temperature output y_1 can track the PCR cycle reference fast and accurately. The maximum overshoot at 94°C is about 0.5 while the undershoot at 60°C region is relatively larger (about 0.8°C). But in all three local regions, errors are within 1°C bound around the set-points, which is acceptable for some DNA amplification operations. The variation range of y_2 is larger than y_1, the largest errors during transition is about 4°C. Since we intended to sacrifice the performance of y_2 to tune y_1, the larger variation is expected. The performances on the rise times and the overshoot magnitudes observed in the experiments are similar to the simulation results. The control signals reach the hardware limitation during the transition. Especially during the 94 to 60°C transition, constant zero values are set for u_2 for a relative longer time span, which is enforced to counteract the coupling effect. Besides the transition regions, the u_2 values are close to the u_{2ss} value for stabilizing y_2 to the constant reference when the coupling from y_1 and u_1 is negligible.

It is found that using the parameters obtained from the simulation the switching controller could still achieve the desired performance in experiments with only a few minor tuning adjustments, which means the system is robust at the local regions. This results validated the effectiveness of the model-based controller switching controller design. The feasibility of the Peltier-based PCR thermal cycler in

disease diagnosis is further illustrated by some viral DNA detection experiments in the following section.

3.4.2 PCR-based genetic amplification results

[1]The validation of the controller design, the instrumentation and the microchip is provided by the successful amplification of viral DNA for detection of BK virus in patient's urine samples. To perform this microfluidics-based virus detection, 2μL of purified DNA from patient's urine sample is included to a final volume of 25μL PCR mixture. To detect the 293 base pair (bp) long on-chip amplified sequence of DNA, the PCR reaction mix contains a final concentration of 1X PCR buffer, 2.8 mM $MgCl_2$. The forward and reverse primers required to selectively bracket the desired regions in the entire DNA strand are found to be optimal at 300nM. Amplification is carried with 1U Platinum Taq DNA polymerase. Thermo-cycling is performed as follows: 5 minutes of denaturation at 94°C, followed by 35 cycles of denaturation at 94°C for 40 seconds, annealing at 60°C for 50 seconds, and extension at 72°C for 40 seconds, and ends with an extension step of 72°C for 3 minutes. Further details of the PCR protocol can be found in [34]. A cross-channel glass capillary electrophoresis (CE) microchip (Micralyne, Edmonton, Canada) is used to verify the PCR amplified product in the microfluidic platform. The electrophoretic run is 240 seconds in duration. The analysis and detection of the amplified DNA is performed by a laser induced fluorescence (LIF) system, which uses the excitation at a wavelength of 532 nm and detection at 578nm. The fluorescence signal is recorded in volts and is graphed as relative fluorescence units (rfu). Further details about this procedure are provided in [15].

Fig. 3.9 shows the electropherogram by the CE analysis using a microfluidic toolkit, the μTK from Micralyne Inc. The first peak in Fig. 3.9 represents the (unused) primers that migrate relatively quickly due to their smaller length, and the second peak represents the fluorescently labeled amplified DNA (fragment of the virus genome), thus indicating a successful microchip-based PCR.

[1]This section includes some results from a published article co-authored with Kaigala et al. [35]. Copyright permission is granted from the co-author.

In this demonstration, the overall reaction time from start to finish is several times slower than the fastest microchip-based demonstrations in the literature [59]. There are mainly two reasons. First of all, we used Peltier-based heater instead of the rapid thin-film element based heater. Using Peltier-based heater instead of the embedded thin film heater, the micro-fabrication cost the microchip has much cheaper micro-fabrication cost thus can be disposable and can reach more general populations. Secondly, in this specific virus detection case, due to the low copy number of viral target of DNA in the urine sample, we have to use relatively large sample volumes and reaction chamber (2μL) and therefore need a relatively large volume of PCR mix (thus a larger thermal mass). This larger thermal mass is the primary rate-limiting factor for the PCR cycling demonstration. Judging from the physical design and the thermal efficiency of the device and its dedicated controller, the thermal heating and cycling speed is only limited by the hardware limitation, we envisage the reaction time and transition time to be significantly reduced in other applications with smaller sample volume.

3.5 Summary

In this chapter, we analyze the characteristics of the three identified local MIMO models and proposed decentralized IMC-PID controller designs for each Peltier module of the two-stage Peltier device. Mixed state-based and time-based switching strategy is adopted to achieve fast transition and precise set-point regulations. Coupling effect and drifts of the heat sink temperature are further included in the switching design to improve the closed-loop performance.

We use the local model at the middle temperature range to simulate the device and test the proposed switching controller. Simulation results show the improvement of the switching controller over non-switching controller on the transition speed and overshoot magnitude. In addition, with the coupling effect and anti-windup included in the switching design, the transition is not only fast but also smooth. Overshoots and oscillations around the set-points are observed, however their magnitudes are below 1°C which are within the current DNA amplification

requirement. Further tuning may be necessary if higher accuracy is expected. Overall, the proposed switching controller can achieve the PCR cycling requirement for DNA amplification, which is validated by the closed-loop tracking performance from repeated experiments. The applications of the Peltier-based device with the switching controller for disease detection is further validated by successful DNA amplification observed after PCR-CE tests. Although, the current controller can satisfy the requirement, which is designed to test the feasibility of microfluidic-based PCR reaction of the custom-made Peltier-device. Further study of the system dynamics and other controller designs are expected to improve the transition performance and reduce the tuning effort.

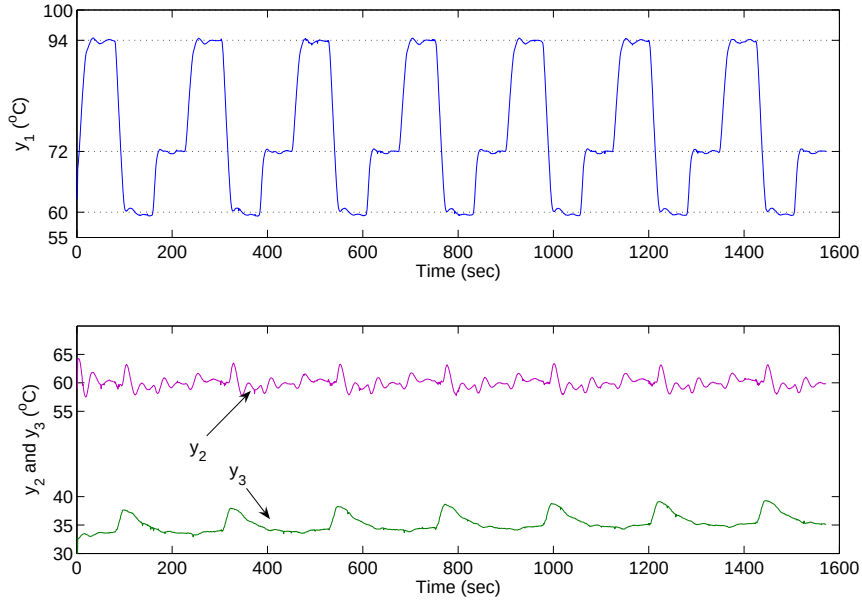

Figure 3.6: Measured temperature outputs of the Peltier-based device for seven representative PCR cycles using a switching PID controller. The top graph shows the temperature output of the top Peltier tracking the desired references at 94°C, 60°C, 72°C, the bottom graph shows the temperature outputs of the bottom Peltier and the heat sink.

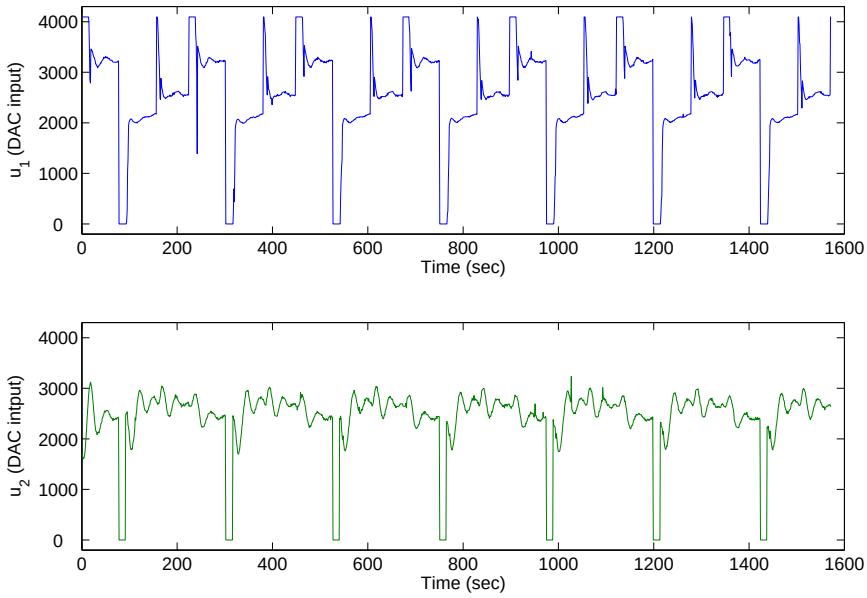

Figure 3.7: Digital control inputs to the Peltier-based device for seven representative PCR cycles using a switching PID controller. The top graph shows the DAC input for the top Peltier, the bottom graph shows the DAC input for the bottom Peltier.

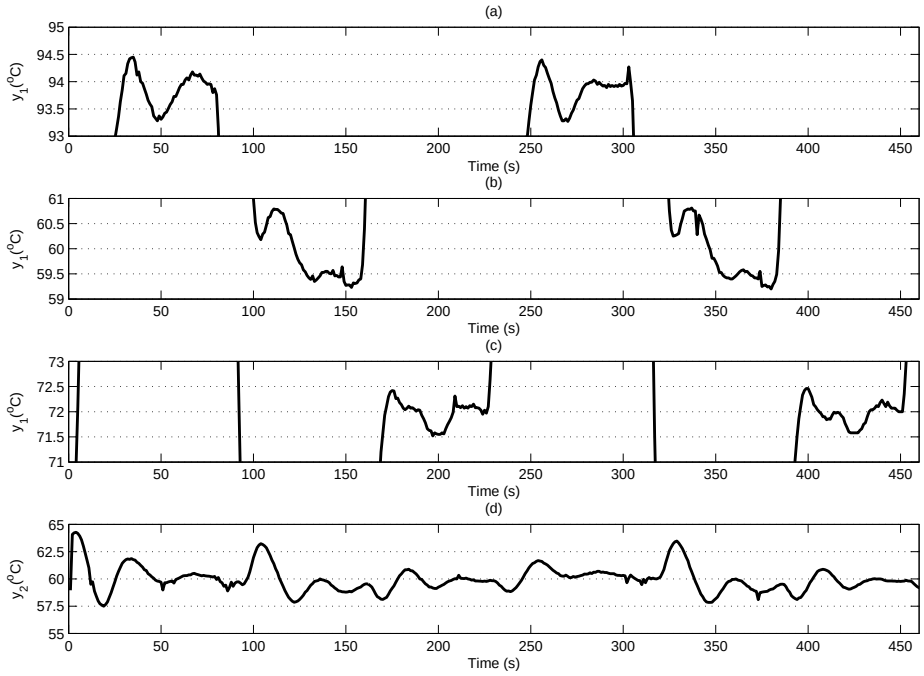

Figure 3.8: Measured outputs at local regions for two representative PCR cycles using a switching PID controller. (a) y_1 around the 94°C region; (b) y_1 around the 60°C region; (c) y_1 around the 72°C region; (d) y_2 around the 60°C region;

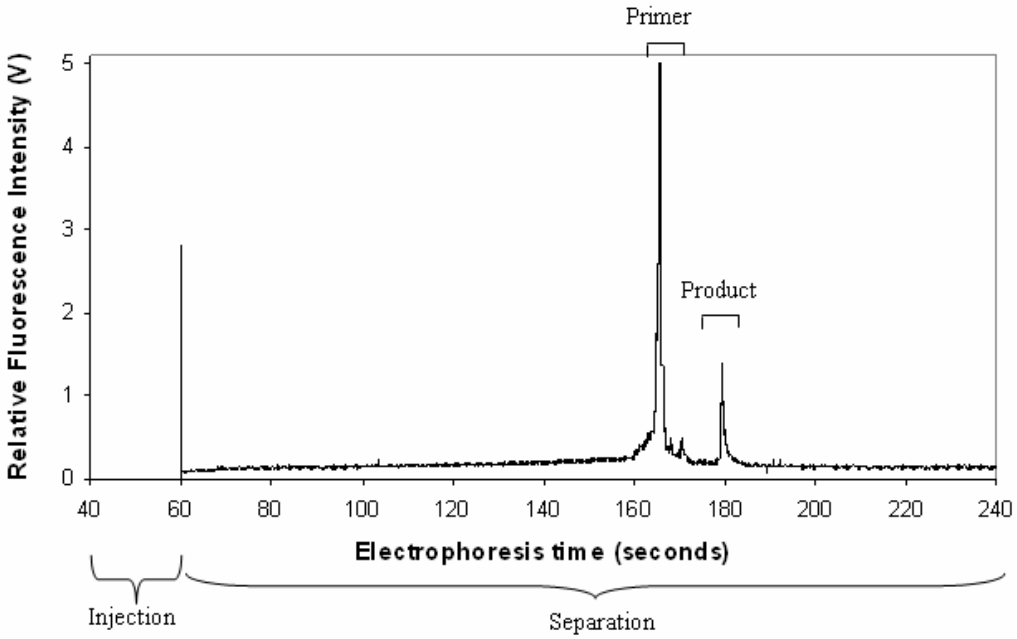

Figure 3.9: Electropherogram of the amplification of a 293bp sample containing a specific virus using the microfluidic platform [35].

Part II

Theoretical modeling and nonlinear controller designs

Chapter 4

Theoretical modeling of the two-stage Peltier-based device

In the first part of the thesis, we briefly studied the characteristics of the nonlinearity of the Peltier-based system. However, due to the limited time for designing a feasible controller to use in the cancer diagnosis project, we chose the linear system identification method to obtain three local models. Although the proposed switching decentralized controller can achieve the PCR cycling performance requirement, the determination of the switching conditions and parameters and the tuning of the PD controllers in transitions require intensive off-line trial-and-errors. In addition, the opposite conditions of fast transition and small overshoot requirements are difficult to satisfy simultaneously using linear model based controllers. Furthermore, since the switching conditions and local model parameters rely on the specific references and operating points. If the reference changes, then new local model identification may be required and the controllers need to be tuned accordingly. To achieve better trade-off between fast transition and small overshoot in the tracking performance and also to avoid further model identification and controller re-designs when the reference changes, we further studied the physical principles of the Peltier-based device and developed a first principle-based nonlinear model for the entire operating range in this chapter. Using this new nonlinear model, nonlinear controller designs can be developed and closed-loop simulations can be performed which could provides more controller options and design convenience for the Peltier-based thermal applications.

4.1 Physical model of a Peltier module

A Peltier module is often composed of multiple N-type and P-type semiconducting elements electrically connected in series and thermally connected in parallel (Fig. 1.3). The heat flux and direction are controlled by the input current flow. Four main thermoelectric effects govern the thermodynamics of a Peltier module: the *Seebeck* effect, the *Peltier* effect, the *Thomson* effect and the *Joule* effect. The *Seebeck* effect is the conversion of temperature differences directly into electricity. If there exists a temperature difference between the two ends, an electrical voltage will be generated in the module which counteracts the external voltage input. This electrical voltage is defined as the *Seebeck* voltage which is the product of the *Seebeck* coefficient and the temperature difference. The *Peltier* effect accounts for the heat pump functionality. When an external voltage is applied to an N-type/P-type thermal couple, heat will be absorbed on one end and pumped out through the other end. The *Joule* effect is the heat generation by an electric current flow and the *Thomson* effect describes the heating or cooling of a homogeneous current-carrying conductor with a temperature gradient [51, 60].

Considering all these effects, electrothermal models of an N-type/P-type couple have earlier been developed in [13, 41] for electronic circuit simulation. In practical applications, a simplified bulk model for heat flux in either heating or cooling mode is adopted, in which the *Thomson* effect is neglected due to its relatively small magnitude [49, 14]. In these bulk models, the heat flux is determined by the electric potential energy due to the absolute *Seebeck* effect, the *Joule* heat, and the heat conduction inside the module. The electric potential energy is the product of the the *Seebeck* potential and the current flow. The *Joule* heating has the fixed direction and half of the overall *Joule* heating travels to each of the junctions, which will enhance the heating effect but diminish the cooling effect [60]. The heat conduction at both junctions are assumed equal, whose direction is always opposite to the heat pump direction. Therefore the heat flux model at two sides of a single Peltier module in

heating mode (top side heating) can be formulated as

$$Q_t = S_M T_t I + 0.5 R_M I^2 - K_M(T_t - T_b) \quad (4.1a)$$

$$Q_b = S_M T_b I - 0.5 R_M I^2 - K_M(T_t - T_b) \quad (4.1b)$$

where Q is the heat flux, T is the absolute temperature, and I is the current flow in the circuit. The subscripts t and b represent the top side and the bottom side of a Peltier. S_M, R_M and K_M are three temperature-dependent bulk parameters of a Peltier module denoting the *Seebeck* coefficient, the module electric resistance, and the module thermal conductance respectively. Here, the subscript M indicates the parameter value of a module instead of a P/N couple. In these heat flux equations, the current flow I is used for calculation as essentially these effects are functions of the internal current flow. Furthermore, except for the *Joule* effect, the other three effects are reversible when the current flow reverses the direction. Therefore, we use the current flow direction to determine whether the Peltier is operated in heating and cooling mode.

During the cooling mode, the current flow direction and the heat flow direction are opposite to those in heating mode, which will affect the sign of some effects too. We define the current flow direction and the heat flow direction in heating mode as positive, and verify Eqn. (4.1a) and (4.1b) with negative current and negative heat flow for the cooling mode. The results show that the same equations from heating mode can be used for cooling mode with this sign definition.

In our actuator implementation, the digital control output from the micro-controller is used to control the voltage input of a Peltier (V_{in}), which is counteracted by the *Seebeck* voltage. Therefore, the relation between the current and the external voltage input can be described as

$$I = (V_{in} - S_M(T_t - T_b))/R_M \quad (4.2)$$

By substituting the current terms in Eqn. (4.1a) and (4.1b) with Eqn. (4.2), the heat flux at each side of a single Peltier with voltage inputs now is formulated as

$$Q_t = -K_M(T_t - T_b) - \frac{S_M^2}{2R_M}(T_t^2 - T_b^2) + \frac{S_M}{R_M} T_b V_{in} + \frac{1}{2R_M} V_{in}^2 \quad (4.3a)$$

$$Q_b = -K_M(T_t - T_b) - \frac{S_M^2}{2R_M}(T_t^2 - T_b^2) + \frac{S_M}{R_M} T_t V_{in} - \frac{1}{2R_M} V_{in}^2 \,. \quad (4.3b)$$

4.2 System formulation

The heat balance equations of the copper plates in direct contact with the top surface of each Peltier are furthers studied to develop the model of the two-stage Peltier-based device. These copper plates are very thin (improving the thermal uniformity along the heat flow direction), have more than 85% of its surface area in direct contact with the adjacent Peltier surface (improving the thermal uniformity along the lateral directions), and have high thermal conductivity. Therefore, we assume that the temperature profile inside each copper plate is uniformly distributed. Under this assumption, the heat flux is proportional to the temperature change rate as $Q = dH/dt = 1/C(dT/dt)$. The parameter $C = 1/(\rho\kappa V)$ is defined as the reciprocal of the thermal mass of the copper plate, where ρ is the material density, κ is the specific heat capacity, and V is the volume of the copper plate. Considering the thermodynamics of each plate in equilibrium, the following equations are derived to describe the net heat flux of these copper plates in contact with the two Peltiers (subscript 1 denotes the top Peltier and 2 denotes the bottom Peltier),

$$\frac{dT_1}{dt} = C_1 s_{1t} Q_{1t} - C_1 Q_{1m} \tag{4.4a}$$

$$\frac{dT_2}{dt} = C_2 s_{2t} Q_{2t} - C_2 s_{1b} Q_{1b} - C_2 Q_{2m} \tag{4.4b}$$

where Q_{it}, Q_{ib} ($i = 1, 2$) are the heat fluxes at the two sides of the ith Peltier, determined by Eqn. (4.3a) and (4.3b). Q_{im} ($i = 1, 2$) is the heat transfer to ambient environment through heat convection and radiation, with heat loss from the copper plate to the environment defined as the positive direction. s_{1t}, s_{1b}, and s_{2t} are three experimentally determined scaling factors introduced to account for the non-ideal heat transfer between Peltier and copper plate.

The heat loss flux Q_m usually is through heat convection and heat radiation, which is calculated by the following equations,

$$Q_m = h\, A_e(T - T_a) + \varepsilon\, \sigma\, A_e(T^4 - T_a^4) \tag{4.5}$$

where h is the heat convection coefficient, σ is the Stefan-Boltzmann constant, ε is the emissivity of the material, and A_e is the effective exposed area. T and T_a are the

surface temperature and ambient temperature respectively [40]. The $(T^4 - T_a^4)$ term in Eqn. (4.5) can be expanded into $(T - T_a)(T + T_a)(T^2 + T_a^2)$, therefore we could isolate $(T - T_a)$, and combine $(T + T_a)(T^2 + T_a^2)$ with $\varepsilon\sigma$ forming a new fictitious coefficient similar to the heat convection coefficient as $h_r = \varepsilon\sigma(T + T_a)(T^2 + T_a^2)$. To evaluate the relative heat loss strength, the heat loss of the two copper plates from convection Q_{conv} and radiation Q_{rad} at three steady-state points are calculated. Nominal values are shown in Table 4.1. An additional term Q_{cond} (heat loss from

Table 4.1: Nominal heat transfer Q_m (J/s) of two copper plates at ambient temperature $T_a = 20$°C

	Copper plate 1					Copper plate 2		
°C	Q_{conv}	Q_{rad}	Q_{cond}	$\frac{Q_{total}}{Q_{conv}}$	°C	Q_{conv}	Q_{rad}	$\frac{Q_{total}}{Q_{conv}}$
94	7.6960	0.3180	0.3461	1.0863	65	1.9800	0.0710	1.0359
72	5.4080	0.2007	0.2596	1.0851	60	1.7600	0.0615	1.0350
60	4.1600	0.1455	0.1731	1.0766	55	1.5400	0.0525	1.0341

conduction) is added into Q_m of the top copper plate, which is included to account for the heat transfer from the top plate to the microfluidic chip. Here, constant temperature difference between the copper plate and the microchip is assumed. The ratios of total heat loss versus heat loss through convection are also listed in Table 4.1. All these values are less than 1.1, which verify that the heat loss by convection is dominant at our operating conditions. Therefore, we choose to approximate the heat transfer flux Q_m by a scaled Q_{conv} with the scaling ratio defined as $r(T) = 1 + h_r/h$. The corresponding quasi-linear model for the total heat loss is expressed as

$$Q_m = r(T)h\,A_s\,(T - T_a) \tag{4.6}$$

In addition, the differences among the values of the ratio $r(T)$ at these three operating points are relatively small (less than 0.1%), therefore we may use constant $r(T)$ in this application.

To derive the state-space formulation of the system, we define $x_1 = T_1$, $x_2 = T_2$, $u_1 = V_{in1}$, $u_2 = V_{in2}$, $d = T_3$ (subscripts 1, 2 denote the top Peltier and the bottom Peltier, and subscript 3 denotes the heat sink). Substituting the Q_t and Q_b with Eqn. (4.3a) and (4.3b), and the heat loss Q_m with Eqn. (4.6), and regroup the coefficients

of the terms , the state-space model of the two-input two-stage Peltier device is formulated as follows,

$$\dot{x}_1 = -q_1 x_1 + q_1 x_2 - q_2 x_1^2 + q_2 x_2^2 + q_3 x_2 u_1 + q_4 u_1^2 - q_5 x_1 + q_5 T_a \quad (4.7a)$$

$$\dot{x}_2 = -q_6 x_2 + q_6 d - q_7 x_2^2 + q_7 d^2 + q_8 u_2 d + q_9 u_2^2 - q_{10} x_2 + q_{10} T_a \quad (4.7b)$$
$$+ q_{11} x_1 - q_{11} x_2 + q_{12} x_1^2 - q_{12} x_2^2 - q_{13} u_1 x_1 - q_{14} u_1^2$$

where $q_{i,\ i=1,\cdots,14}$ are the new coefficients whose definitions are listed in Table 4.2). The definitions of two parameters q_5 and q_{10} are different with other parameters

Table 4.2: Definition of $q_{i,\ i=1,\cdots,14}$ of the two-stage Peltier model

q_1	q_2	q_3	q_4	q_5
$C_1 s_{1t} K_{M1}$	$\frac{C_1 s_{1t} S_{M1}^2}{2R_{M1}}$	$\frac{C_1 s_{1t} S_{M1}}{R_{M1}}$	$\frac{C_1 s_{1t}}{2R_{M1}}$	$C_1 r_1 f_1 h A_{s1}$
q_6	q_7	q_8	q_9	q_{10}
$C_2 s_{2t} K_{M2}$	$\frac{C_2 s_{2t} S_{M2}^2}{2R_{M2}}$	$\frac{C_2 s_{2t} S_{M2}}{R_{M2}}$	$\frac{C_2 s_{2t}}{2R_{M2}}$	$C_2 r_2 f_2 h A_{s2}$
q_{11}	q_{12}	q_{13}	q_{14}	
$C_2 s_{1b} K_{M1}$	$\frac{C_2 s_{1b} S_{M1}^2}{2R_{M1}}$	$\frac{C_2 s_{1b} S_{M1}}{R_{M1}}$	$\frac{C_2 s_{1b}}{2R_{M1}}$	

as each of them includes an additional scaling function (f_1 in q_5 and f_2 in q_{10}). $f_i(x, \dot{x}, u),\ i = 1, 2$ are introduced mainly for the extreme heating/cooling regions, where the control value u may saturate at the hardware limitation, and the values of temperature change rate $\dot{x}$ are far away from normal values in local regions. The heat loss of a copper plate with large $\dot{x}$ or u values will have some irregular results, which are further obtained from experimental data.

4.3 Model implementation and validation

The dynamic state-space model is coded as an S-function in Simulink® 7.0 from Mathworks. Fixed material property dependent parameters such as A_{s1}, A_{s2}, h are calculated in the S-function initialization. The dimensions of the microchip, the Peltier module and the copper plates are listed in Table 4.3, which are used to calculate the effective contact area for heat transfer A_{s1}, A_{s2} and the volume of

the copper plates V_1 and V_2. Using $\rho_{cu} = 8.9\text{g/cm}^3$, $\kappa_{cu} = 0.385\text{J/g/K}$ and the corresponding V_1/V_2, C_1/C_2 can be also calculated in the initialization.

Table 4.3: Physical dimension of the Peltier module and copper plates

	Width (mm)	Length (mm)	Height (mm)
Microchip	31.00	11.00	2.00
Peltier module	39.70	39.70	3.94
Top plate	50.00	50.00	2.00
Middle plate	50.00	50.00	1.00
Bottom plate	140.00	130.00	15.00

The temperature-dependent parameters S_M, K_M, and R_M of each Peltier are calculated at each simulation step using a 3rd order polynomial function based on an empirical formula from the manufacturer [14]. When the temperature difference between the two sides of a Peltier module is zero, the module parameters can be calculated as

$$x_M(T) = x_1 + x_2T + x_3T^2 + x_4T^3 \tag{4.8}$$

where x can be $S/K/R$, and the coefficients in the polynomial function are obtained by approximation from experimental data, and T is the absolute temperature of either surface of the Peltier. When there is temperature difference between two sides, we calculate $x_M(T_t)$ and $x_M(T_b)$ first using the formula in Eqn. (4.8), and obtain the overall x_M as

$$x_M = \frac{x_M(T_t) - x_M(T_b)}{T_t - T_b} \tag{4.9}$$

From the manufacturer, nominal values of $x_i, \imath = 1, \cdots, 4$ for a 71 couple/ 6 ampere module is provided which is listed in Table 4.4 [11]. To derive S_M, K_M, and R_M of the 127 couple/ 8.5 ampere module used in our device, we assume the linear relation and scale the x_i values by the ratio of the couple numbers $127/71$. The accuracy of this approximation is verified at some typical operating temperatures.

The scaling factors s_{1t}, s_{1b}, s_{2t}, $f_1(x, \dot{x}, u)$ and $f_2(x, \dot{x}, u)$ are initially set to unity. Random Binary Signal (RBS) input tests around the three local operating points are applied, and the responses are used to find a single set of values of (s_{1t}, s_{1b}, s_{2t}) to be used in three local models. $s_{1t} = 0.9$, $s_{1b} = 0.75$ and $s_{2t} = 1.0$ are

Table 4.4: Coefficient values of the empirical polynomial approximations of three temperature-dependent parameters.

x	s_i(V/K)	k_i(W/K)	r_i(Ohm)
x_1	1.33450$\times 10^{-2}$	4.76218$\times 10^{-1}$	2.08317
x_2	-5.37574$\times 10^{-5}$	-3.89821$\times 10^{-6}$	-1.98763$\times 10^{-2}$
x_3	7.43731$\times 10^{-7}$	-8.64864$\times 10^{-6}$	8.53832$\times 10^{-5}$
x_4	-1.27141$\times 10^{-9}$	2.20869$\times 10^{-8}$	-9.03143$\times 10^{-8}$

chosen to approximate the models at the three operating ranges with least errors. The values of r_1 and r_2 at the intermediate temperature 72°C are used in the heat loss calculations, which are $r_1 = 1.085$ and $r_2 = 1.035$ respectively. Using this set of (s_{1t}, s_{1b}, s_{2t}) and (r_1, r_2) values, the single simulated nonlinear model can approximate three local systems separately, the model output of six different RBS input responses are compared with measured data and shown in Fig. 4.1-4.6. For any individual RBS response, the model/data errors are higher than the best linear model system identification results. However, as we limit the usage of scaling factors to one set in our model for six different scenarios, the modeling errors are tolerable.

To find the values of $f_i(x, \dot{x}, u)$ during transitions, a closed-loop response using the previously designed decentralized PI/PD switching controller for PCR cycling in [35] is used. Measured u and the heat-sink temperature d are used as the inputs, and simulations with different f_i are repeated to find f_i values with the least integral of model/data error over each transition region. However, due to the complexity of the dynamics during transitions, the expression of f_i is not smooth and a simplified look-up table with different conditions is developed.

Simulated model outputs of three PCR cycles are plotted in Fig. 4.7 (as solid lines) together with measured outputs (as dotted lines). In local regions around 94°C and 72°C, simulated results of x_1 are within ± 1 °C bound of the actual output. The model errors around 60°C are within $\pm$ 1.5°C bound. The difference in the error magnitudes is because that model parameters $f_1(x, \dot{x}, u)$ and $f_2(x, \dot{x}, u)$ have larger approximation errors at the 60°C region where u_1 is close to zero voltage input. The modeling errors of x_2 are bounded by ± 2 °C with a few exceptions. These exceptions are mainly due to the strong coupling from u_1 to the dynamics of

x_2. Although the modeling errors of x_2 are relatively larger, the modeling error of x_1 compared to the variation range of x_1 is much smaller. Since in PCR application, the target PCR temperature is x_1, relative larger errors in x_2 are acceptable. Considering the tradeoff between model accuracy and parameter complexity, the modeling errors with the proposed structure and parameter values can be tolerated. Overall, this theoretical model can capture the characteristics of both the transition and the steady-state responses of the cascade Peltier module-based device and provide a test-bench for closed-loop simulations of different controller designs.

4.4 Summary

A nonlinear theoretical model of the two-stage Peltier-based device is developed, an empirical parameter calculation method is introduced in the model to account for those state-dependent parameters. Considering the convenience for model-based controller designs, higher order functions are further approximated with lower order functions which is the trade-off between model accuracy and model simplicity. The basic principles used for this modeling are the thermodynamics of the interfacing materials and the bulk models of individual Peltier modules, difficulties lie in the determination of the heat transfer amount to the environment during extreme heating/cooling situations. In these situations, we introduced two nonlinear gain ratio function f_1 and f_2 to account for non regular heat loss and determine their values through data analysis by minimizing the integral of the error of the closed-loop simulation results. Relatively higher model accuracy is achieved in the top Peltier than the bottom Peltier as the dynamics of x_2 is more complicated during transitions especially when both x_1 and x_2 are operating around the 60°C regions. In the simplified model, the dynamics includes only first order and second order terms of x and u, and the parameters numbers are minimized. Using the simplified model, designing single or switching nonlinear controllers for the entire operating range are feasible, which will be discussed the later chapters.

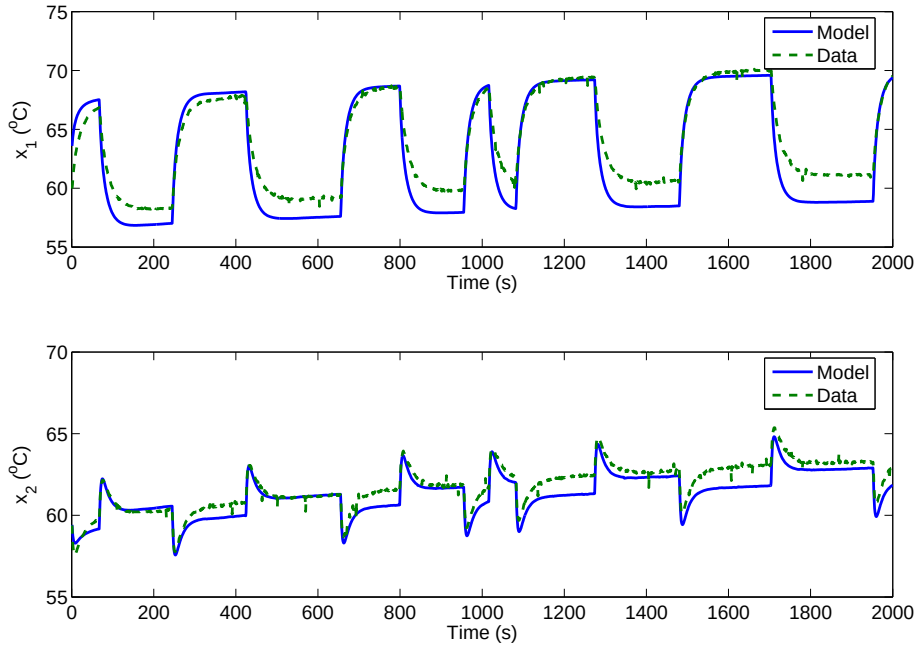

Figure 4.1: Open-loop model output vs. experimental data around 60°C region with an RBS input in u_1: top Peltier temperature x_1 (top graph), bottom Peltier temperature x_2 (bottom graph). (solid) Model output; (dashed) measured output.

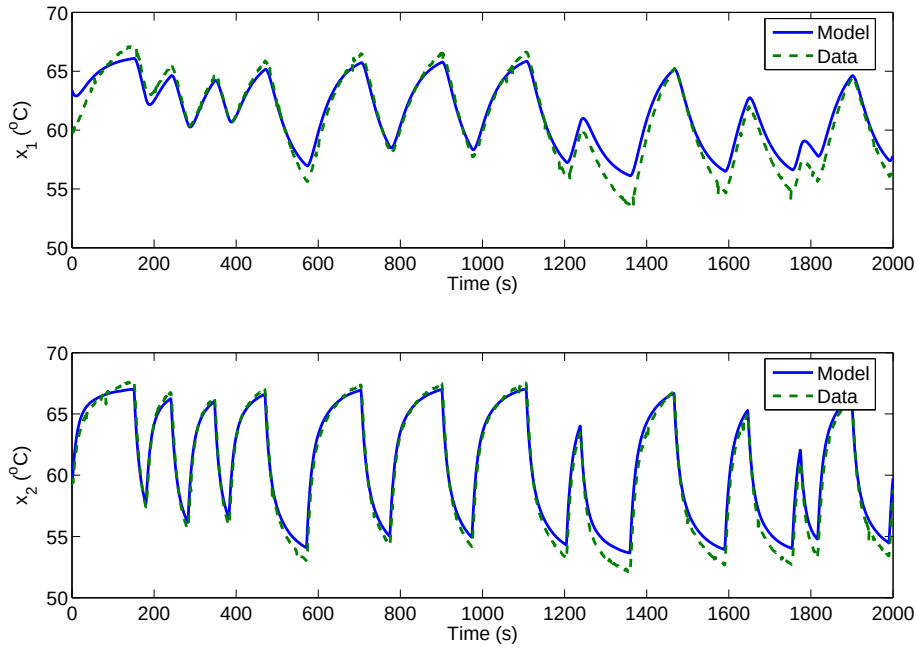

Figure 4.2: Open-loop model vs. experimental data around 60°C region with an RBS input in u_2: top Peltier temperature x_1 (top graph), bottom Peltier temperature x_2 (bottom graph). (solid) Model output; (dashed) measured output.

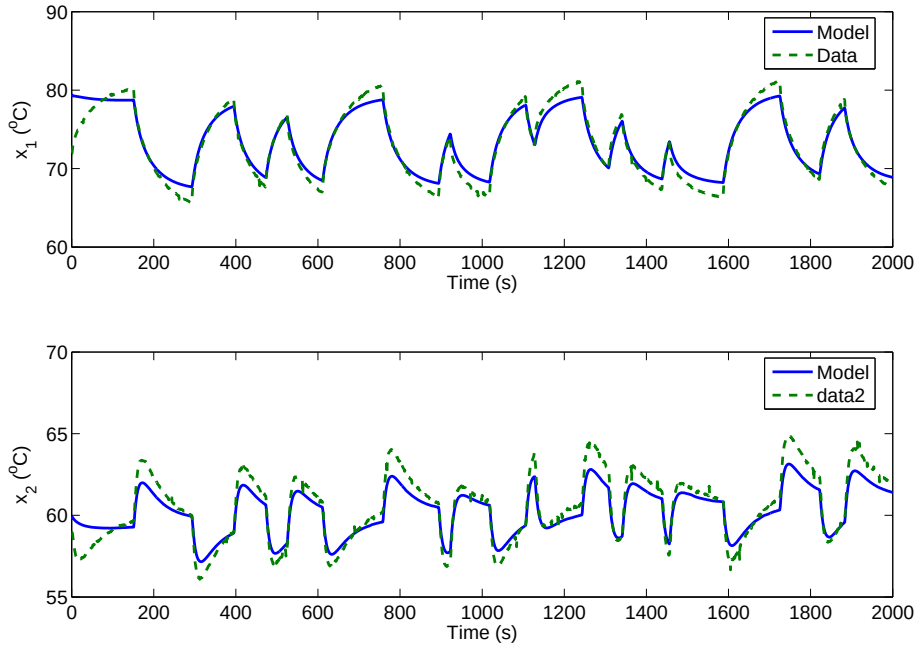

Figure 4.3: Open-loop model vs. experimental data around 72°C region with an RBS input in u_1: top Peltier temperature x_1 (top graph), bottom Peltier temperature x_2 (bottom graph). (solid) Model output; (dashed) measured output.

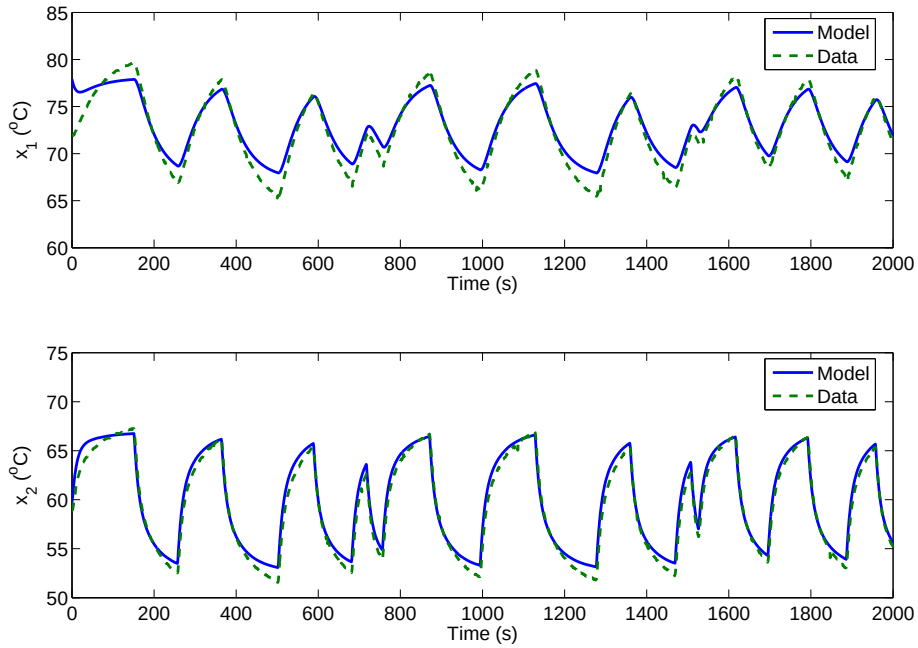

Figure 4.4: Open-loop model vs. experimental data around 72°C region with an RBS input in u_2: top Peltier temperature x_1 (top graph), bottom Peltier temperature x_2 (bottom graph). (solid) Model output; (dashed) measured output.

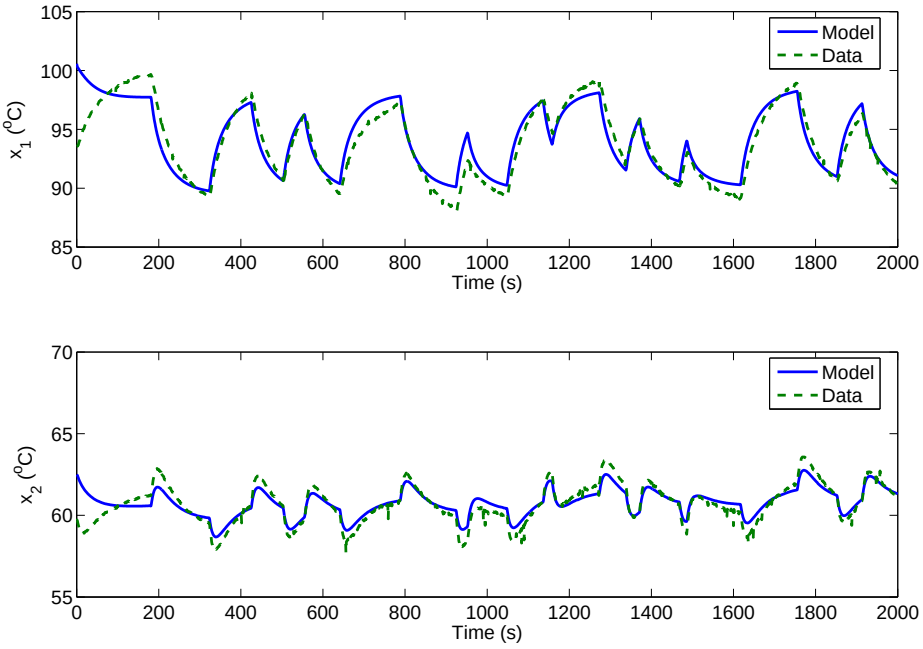

Figure 4.5: Open-loop model vs. experimental data around 94°C region with an RBS input in u_1: ttop Peltier temperature x_1 (top graph), bottom Peltier temperature x_2 (bottom graph). (solid) Model output; (dashed) measured output.

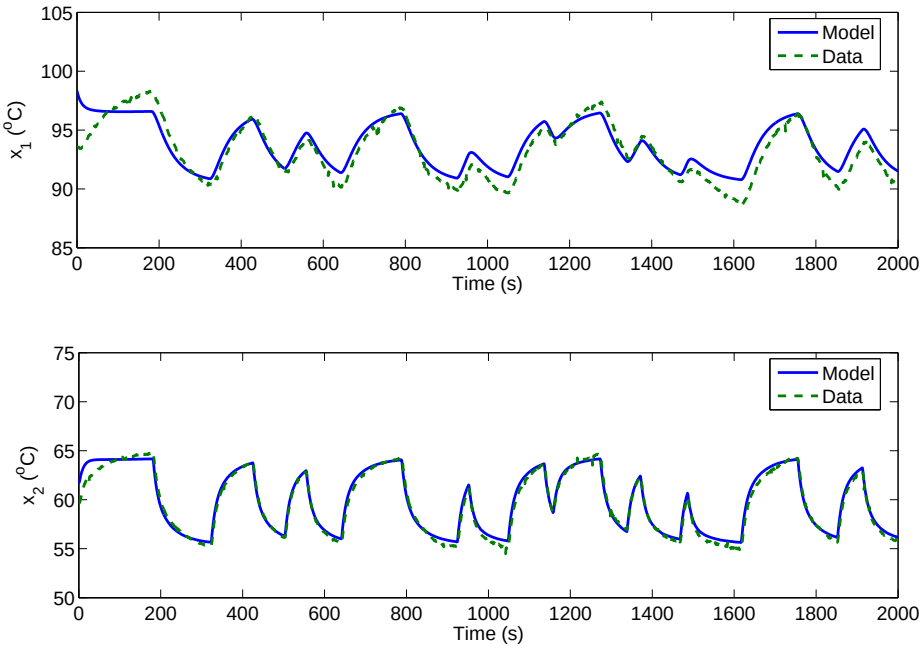

Figure 4.6: Open-loop model vs. experimental data around 94°C region with an RBS input in u_2: top Peltier temperature x_1 (top graph), bottom Peltier temperature x_2 (bottom graph). (solid) Model output; (dashed) measured output.

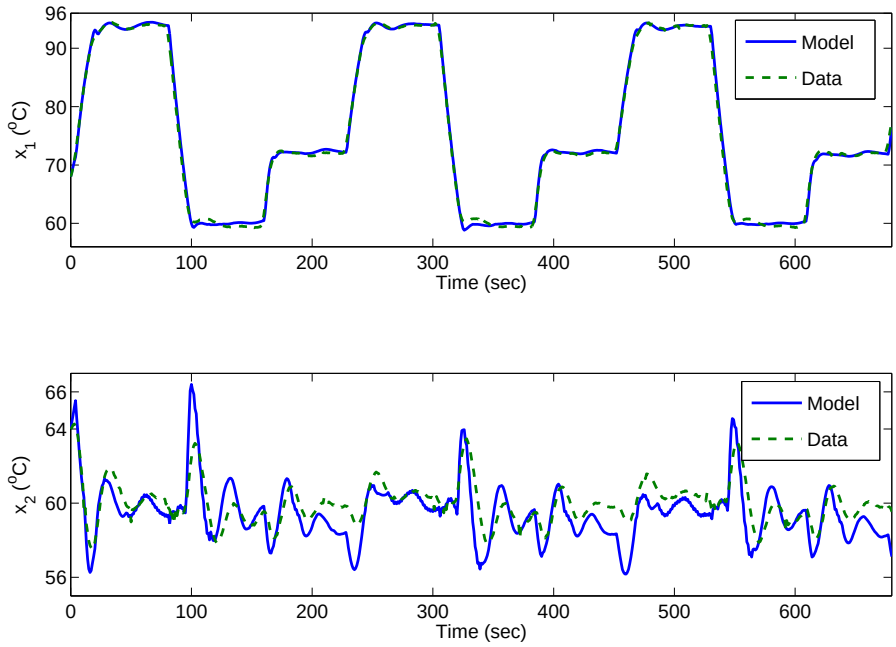

Figure 4.7: Closed-loop model output vs. experimental data with three PCR cycles of the Peltier system using a switching decentralized PID controller: the temperature of the top Peltier x_1 (top graph), the temperature of the bottom Peltier x_2 (bottom graph). (solid) Simulated model output, (dashed) measured output.

Chapter 5

Extended feedback linearization-based design

The state-space model of the Peltier device represented in Eqn. (4.7a) and (4.7b) is not a typical nonlinear control affine system. The dynamic equations depend not only on u, but also on u^2. Techniques using the inverse of the coefficient of u to isolate u for further design will be more difficult in a MIMO system with the appearance of u_i^2. Therefore, special transformation of the control signal will be necessary. One technique is to augment the control signal as $[u_i; u_i^2]$. Although the augmented system is in normal control affine form, the constraints on the control signal are not expressed explicitly which make the controller design challenging. In this chapter, we consider another approach by changing of variable on the control input to transform the system model to the control affine form without augmenting the dimension. The feasibility of this change of variable depends on the two conditions. First of all, the system can be partially decouple which means the MIMO controller design can be transformed into sequential SISO design. Secondly, there exist some real solution of the square root of the newly transformed control variable. The existence conditions of real solution depend on the system dynamics and the operating conditions which usually are not guaranteed globally. For each SISO sub-system of the transformed dynamics in control affine form, we can choose various nonlinear controller design. An input-to-state feedback linearization technique is considered here for the SISO subsystem due to its simplicity in design and the convenience in extension to high order systems.

5.1 Error dynamics

Defining the error signals as $e_1 = r_1 - x_1$ and $e_2 = r_2 - x_2$, the error dynamics of the system are derived from the simplified state space equations in Eqn. (4.7a) and (4.7b) as

$$\dot{e}_1 = \dot{r}_1 + q_1 x_1 - q_1 x_2 + q_2 x_1^2 - q_2 x_2^2 + q_5 x_1 - q_5 T_a - q_3 x_2 u_1 - q_4 u_1^2 \quad (5.1a)$$

$$\dot{e}_2 = q_6 x_2 - q_6 d + q_7 x_2^2 - q_7 d^2 + q_{10} x_2 - q_{10} T_a - q_{11} x_1 + q_{11} x_2 \quad (5.1b)$$
$$- q_{12} x_1^2 + q_{12} x_2^2 + q_{13} u_1 x_1 + q_{14} u_1^2 - q_8 d u_2 - q_9 u_2^2$$

We keep both x_i and e_i terms in the equations for simplifying the notation. Also there is not $\dot{r}_2$ term in the error dynamics since $\dot{r}_2 = 0$.

For non-constant tracking application of the typical PCR cycling reference, we would need to have a reference with analytic first derivatives for the derivation of the error dynamics. Because at these step times the derivatives of the step reference are impulse functions. This type of $\dot{r}$ cannot be used over large variation ranges during transitions. Instead, we design a new reference signal using a combination of a ramp function and a sigmoid function to approximate each step change. The derivative of this new reference is smooth almost everywhere except a few points where the switching from the ramp to the sigmoid function happens and the switching from the sigmoid function to the constant set-point happens. The slope of the ramp function is set at the maximum temperature change rate limited by the hardware when the target temperature is far away. When the reference is close to the target temperature, either a full sigmoid function or a half sigmoid function is used to approximate the smooth transition, which has a descending slope and the value of the slope can be calculated easily [71]. In addition, the shape of the sigmoid function can be further adjusted by a scaling factor s (also known as the steepness factor). The new reference signal for one transition region is formulated as

$$r(t) = r_0 + K(t - t_0) \quad \text{when } t_0 \le t \le t_s \quad (5.2a)$$

$$r(t) = r(t_s) + \frac{2D}{1 + e^{-(t - t_s)/s}} - \sigma D \quad \text{when } t_s < t \le t_e \quad (5.2b)$$

where t_0, t_s and t_e denote beginning, switching and ending times of a transition region. Other parameters in Eqn. (5.2a) and (5.2b) are determined according to

the requirements imposed by thermal cycling and hardware. $|D|$ is the distance to be covered by the sigmoid function and the sign of D is determined by the slope direction. σ can be set to 0 or 1 to determine whether half or full sigmoid function is used ($\sigma = 1$ denotes half sigmoid function is used).

The reference of an entire cycle is constructed by three transitions followed by three constant set-point regions. The partition of an entire cycle of a PCR reference is illustrated in Fig. 3.1, and the parameters to construct the reference of each transition region from transition 0 to transition 3 are listed in Table 5.1.

Table 5.1: Parameter values of the constructed reference in different transition regions

Transition region	r_0	t_s	$r(t_s)$	K	D	s	σ
T_0: 60°C→94°C	60	9.6	84	2.5	10	1.6	1
T_1: 94°C→60°C	94	9.6	70	-2.5	-10	1.6	1
T_2: 60°C→72°C	60	5	60	0	6	1.0	0
T_3: 72°C→94°C	72	4.8	84	2.5	10	1.6	1

For example, to construct the reference of the transition from 60 to 94°C, $r_0 = 60$, $t_s = 9.6$, $r(t_s) = 84$, $K = 2.5$, $D = 10$, $\sigma = 1$ and $s = 1.6$ are used, which means a ramp function is used for the reference between 60 to 84°C and a half sigmoid function is used to approximate the transition from 84 to 94°C. The steepness factor s of the sigmoid function is 1.6, which can be further tuned depending on the requirement of transition time. For the short transition from 60 to 72°C, no ramp function is used, therefore both t_s and K are zeros. And a full sigmoid function covers the entire step-size, so $D = 6$ is the distance covered by half sigmoid function. $t_s = 5$ is used to set middle point of curve instead of the switching (which means the overall transition time is set at 10 seconds). σ is set to zero which removes the shifting of the middle point. Each transition is followed by a constant set-point, therefore the reference of an entire cycle can be constructed and used in controller designs.

5.2 Extended input-to-state feedback linearization

We find that the derivatives of the errors in Eqn. (5.1a) and (5.1b) not only depend on the u_i terms but also the u_i^2 terms. Controller design for this type of system is challenging. General properties of this type of systems are studied, and a matrix formulation of these systems is expressed as

$$\dot{x} = F(x) + G(x)\begin{bmatrix} u_1 \\ \vdots \\ u_n \end{bmatrix} + H(x)\begin{bmatrix} u_1^2 \\ \vdots \\ u_n^2 \end{bmatrix}, \quad x \in R^n,\ u \in R^n \tag{5.3}$$

where $F(x)$, $G(x)$ and $H(x)$ are matrices with each element being a scalar function of state. We also observe that $\dot{e}_1$ relies on (e, u_1, u_1^2) and $\dot{e}_2$ relies on $(e, u_1, u_1^2, u_2, u_2^2)$. This type of property is very similar to the definition of the strict feedback form for nonlinear control affine systems. Here we define the strict feedback form for a class of nonlinear systems not only affine on the control but also affine on the higher orders of control inputs.

Definition 1. ***Strict feedback form:*** *For a nonlinear system with n states and n inputs that is not only affine on the control but also affine on the higher orders of control inputs (up to m), if* $\dot{x}_1$ *only depends on* $(x, u_1, \cdots, u_1^m)$, $\dot{x}_2$ *depends on* $(x, u_1, \cdots, u_1^m, u_2, \cdots, u_2^m)$, *and* $\dot{x}_n$ *depends on* $(x, u_1, \cdots, u_1^m, u_2, \cdots, u_2^m, \cdots, u_n, \cdots, u_n^m)$, *then the system is in* ***strict feedback form****.*

For systems formulated in matrix form as Eqn. (5.3), the conditions of strict feedback form can be described as $G(x)$ and $H(x)$ are lower triangular.

If a nonlinear control affine system is in strict feedback form, it can be stabilized by recursive application of backstepping [18]. Similarly, if a nonlinear system that is affine on the control and the higher orders of control is in strict feedback form, it can be stabilized by recursive individual controller designs. Thus the MIMO controller design is reformulated into sequential SISO designs. To obtain the SISO version of Eqn. (5.3), $F(x)$, $G(x)$, and $H(x)$ are replaced with scalar $f(x)$, $g(x)$ and $h(x)$. By completing the square on u in the SISO case, we introduce a new control variable $\bar{u}(u, x) = (u + a(x))^2$, where $a(x) = h^{-1}(x)g(x)/2$. Using this

new control variable, the SISO system is transformed into control affine form,

$$\dot{x} = \bar{f}(x) + \bar{g}(x)\bar{u} \tag{5.4}$$

where $\bar{f}(x) = f(x) - h(x)a(x)^2$ and $\bar{g}(x) = h(x)$. Many nonlinear controller design methods can be applied to the SISO subsystem under the constraint $\bar{u} \geq 0$. We choose the input-state feedback linearization design. The idea behind the input-to-state feedback linearization is to use coordinate transformation $z = T(x)$ to transform the original nonlinear control affine system as Eqn. (5.4) into a linear system as [47, 36],

$$\dot{z} = Az + B\omega(x)(\bar{u} - \phi(x)) \tag{5.5}$$

and the transformation $T(z)$ satisfies the following equality,

$$\frac{\partial T}{\partial x}\left(\bar{f}(x) + \bar{g}(x)\bar{u}\right) = AT(x) + B\omega(x)(\bar{u} - \phi(x)) \tag{5.6}$$

For the transformed new linear system in z-coordinate, we can design the control as $\bar{u} = \phi(x) + \omega^{-1}(x)v$, and render the system into $\dot{z} = Az + Bv$, which is in standard linear system formulation.

The sufficient and necessary conditions of the nonlinear system is input-to-state feedback stabilizable is that $\bar{f}$ and $\bar{g}$ satisfies two conditions. The following theorem describes the conditions.

Theorem 5.1. *[47] The nonlinear control affine system as*

$$\dot{x} = f(x) + g(x)u$$

is input-to-state linearizable on $D_0 \subset D$ if and only if the following conditions are satisfied:

(i) The vector fields $\left\{g(x), ad_f g(x), \cdots, ad_f^{n-1} g(x)\right\}$ are linearly independent in D_0. This condition is equivalent to the matrix $C = [g(x), ad_f g(x), \cdots, ad_f^{n-1} g(x)]_{n\times x}$ has rank n for all $x \in D_0$.

(ii) The distribution $\Delta = span\left\{g, ad_f g, ad_f^{n-2} g\right\}$ is involutive in D_0.

The proof is omitted here, which can be found in many nonlinear control books as [47, 36]. The two conditions guarantee the existence of the transformation T and T^{-1} and the existence of inverse of $\omega(x)$.

For the special case in our system, each SISO system has only one state variable, so the feasibility of the input-state feedback linearization is guaranteed by the existence of the inverse of $\bar{g}(x) = h(x)$. Here, the inverse of $h(x)$ exists almost everywhere except a few points when $h(x) = 0$. When $h(x) = 0$, which means u^2 will not affect the dynamics, the original SISO system is already in control affine form. Therefore, we will only consider $h(x) \neq 0$ scenarios. We choose to use a simple design to cancel the nonlinear term and assign the dynamics to $-A(t)x$. Non-constant $A(t)$ is used here to include more general cases. The corresponding controller has the following structure

$$\bar{u} = -\bar{g}^{-1}(x)(\bar{f}(x) + A(t)x), \quad A(t) > 0 \quad \text{and} \quad \bar{u} \geq 0 \tag{5.7}$$

The stability of this feedback linearization design can be guaranteed if $A(t), t \geq 0$ is always positive. The constraint of $\bar{u} \geq 0$ is equivalent to the inequality $\bar{g}(x)(\bar{f}(x) + A(t)x) \leq 0$, which is the sufficient condition of the existence of a solution of $\bar{u}$. Therefore the range of $A(t)$ relies on the signs of $\bar{g}(x)$, x and the magnitude of $-\bar{f}(x)/x$. As far as $\bar{u}_i \geq 0$, we can design u_1 first and design u_i sequentially while treating $u_j,\ j = 1, \cdots, i-1$ as known parameters.

To derive a general form of control of each subsystem in the feedback linearization based controller, we expand the two lower triangular G and H matrices in Eqn (5.3) and obtain the dynamic equations as

$$\begin{aligned}
\dot{x}_1 &= f_1(x) + g_{11}(x)u_1 + h_{11}(x)u_1^2 \\
\dot{x}_2 &= f_2(x) + g_{21}(x)u_1 + g_{22}(x)u_2 + h_{21}(x)u_1^2 + h_{22}(x)u_2^2 \\
\vdots &= \vdots \\
\dot{x}_n &= f_n(x) + g_{n1}(x)u_1 + g_{n2}(x)u_2 + \cdots + g_{nn}u_n + h_{n1}(x)u_1^2 + h_{n2}(x)u_2^2 \\
&\quad + \cdots h_{nn}(x)u_n^2
\end{aligned} \tag{5.8}$$

If $h_{ii}, i = 1, \cdots, n$ in Eqn. (5.8) are non-zeros, we can define some new functions $a_i(x) = g_{ii}(x)/h_{ii}(x)/2$ and choose some α_i for the i-th sub-system and

obtain the corresponding input-to-state feedback linearization based controller as follows,

$$\begin{aligned}
\bar{u}_1 &= -h_{11}^{-1}(x)(f_1(x) - h_{11}(x)a_1^2(x) + \alpha_1 x_1) \\
\bar{u}_2 &= -h_{22}^{-1}(x)(f_2(x) - h_{22}(x)a_2^2(x) + g_{21}(x)u_1 + h_{21}(x)u_1^2 + \alpha_2 x_2) \\
\vdots &= \vdots \\
\bar{u}_n &= -h_{nn}^{-1}(x)(f_n(x) - h_{nn}(x)a_n^2(x) + \sum_{j=1}^{n-1} g_{nj}(x)u_j + \sum_{j=1}^{n-1} h_{nj}(x)u_j^2 + \alpha_n x_n)
\end{aligned} \tag{5.9}$$

where $\alpha_i, i = 1, \cdots, n$ are controller tuning parameters. To guarantee the existence of solution u_i for the original system, $\bar{u}_i \geq 0$ is the sufficient condition. Assuming $\bar{u}_i \geq 0$, then the feedback linearization-based controller can be calculated as,

$$\begin{aligned}
u_1 &= -a_1(x) \pm \sqrt{\bar{u}_1} \\
u_2 &= -a_2(x) \pm \sqrt{\bar{u}_2} \\
\vdots &= \vdots \\
u_n &= -a_n(x) \pm \sqrt{\bar{u}_n}
\end{aligned} \tag{5.10}$$

The stability of the closed-loop system using this sequential feedback linearization-based controller design is proved in the following theorem.

Theorem 5.2. *For a nonlinear system defined in Eqn. (5.8) with $h_{ii}(x) \neq 0$, if there exists some $\alpha_i > 0,\ i = 1, \cdots, n$ satisfies that*

$$\alpha_i x_i + \left(f_i(x) - \frac{g_{ii}^2(x)}{4h_{ii}(x)} + \sum_{j=1}^{i-1} g_{ij}(x)u_j + \sum_{j=1}^{i-1} h_{ij}(x)u_j^2 \right)$$

has an opposite sign of $h_{ii}(x)$, then the extended feedback linearization-based controller defined in Eqn. (5.9) and (5.10) can stabilize the system.

Proof. Since the system is in strict feedback form, the entire system can be stabilized by recursive individual controllers.

If $h_{ii}(x) \neq 0$ and $\alpha_i x_i + \left(f_i(x) - \frac{g_{ii}^2(x)}{4h_{ii}(x)} + \sum_{j=1}^{i-1} g_{ij}(x)u_j + \sum_{j=1}^{i-1} h_{ij}(x)u_j^2 \right)$ has an opposite sign of $h_{ii}(x)$, then $\bar{u}_i >= 0$ is guaranteed.

Next, we substitute $\bar{u}_i$ into the dynamics equations sequentially. When $i = 1$, we have $\dot{x}_1$ as

$$\begin{aligned}\dot{x}_1 &= f_1(x) - \frac{g_{11}^2(x)}{4h_{11}(x)} + h_{11}(x)\left(u_1 + \frac{g_{11}(x)}{2h_{11}(x)}\right)^2 \\ &= f_1(x) - h_{11}(x)a_1^2(x) + h_{11}(x)\bar{u}_1 \\ &= -\alpha_1 x_1\end{aligned}$$

Since $\alpha_1 > 0$, the subsystem of x_1 is exponentially stable with u_1.

When $i = 2$, u_1 is available, fill in u_1 and $\bar{u}_2$ into the dynamic equation, and we have $\dot{x}_2$ as

$$\begin{aligned}\dot{x}_2 &= f_2(x) + g_{21}(x)u_1 + h_{21}(x)u_1^2 - \frac{g_{22}^2(x)}{4h_{22}(x)} + h_{22}(x)\left(u_2 + \frac{g_{22}(x)}{2h_{22}(x)}\right)^2 \\ &= f_2(x) + g_{21}(x)u_1 + h_{21}(x)u_1^2 - \frac{g_{22}^2(x)}{4h_{22}(x)} + h_{22}(x)\bar{u}_2 \\ &= -\alpha_2 x_2\end{aligned}$$

Therefore the subsystem of x_2 is exponentially stable under control (u_1, u_2). Similarly for $i = 3, \cdots, n$, $\dot{x}_i$ equals to $-\alpha_i x_i$. If $\alpha_i > 0$, then the ith subsystem is stable.

Finally choose a Lyapunov function as $V = \frac{1}{2}\sum_{i=1}^{n} x_i^2$, it is straightforward that

$$\dot{V} = \sum_{i=1}^{n} x_i \dot{x}_i = -\sum_{i=1}^{n} \alpha_i x_j^2 \leq 0$$

and $\dot{V} = 0$ if and only if $x = 0$. Therefore, the stability of the entire system is proved. □

Applying the sequential extended feedback linearization-based control design to the error dynamics of the Peltier device, the following algorithm is developed:

Algorithm: Extended Feedback Linearization-based controller

1. Choose some positive values α_1 and α_2

2. Calculate the value of c_1 defined as

$$c_1 = \dot{r}_1 + q_1 r_1 + q_2 x_1^2 + q_5 r_1 - q_1 x_2 - q_2 x_2^2 - q_5 T_a$$

3. Fill in the values of c_1 and e_1 into the following equality

$$\left(u_1 + \frac{q_3 x_2}{2q_4}\right)^2 = \left(\frac{q_3 x_2}{2q_4}\right)^2 + \frac{c_1 + \alpha_1 e_1}{q_4} \tag{5.11}$$

and solve for u_1. The sign of u_1 is determined by the operating condition and the magnitude is limited by constraints. $\tilde{u}_1 = \min(u_{1max}, u_1)$, if $u_1 \geq 0$, and $\tilde{u}_1 = \max(u_{1min}, u_1)$, if $u_1 < 0$.

4. Fill in the value of $\tilde{u}_1$ and calculate c_2 as

$$\begin{aligned} c_2 &= q_6(r_2 - d) + q_7(x_2^2 - d^2) - q_{11}(x_1 - x_2) - q_{12}(x_1^2 - x_2^2) + q_{10}(r_2 - T_a) \\ &\quad + q_{13} x_1 \tilde{u}_1 + q_{14} \tilde{u}_1^2 \end{aligned}$$

5. Fill in the values of c_2 and e_2 into the following equality

$$\left(u_2 + \frac{q_8 x_d}{2q_9}\right)^2 = \left(\frac{q_8 d}{2q_9}\right)^2 + \frac{c_2 + \alpha_2 e_2}{q_9} \tag{5.12}$$

and solve for u_2. Apply the constraints to u_2 and get $\tilde{u}_2$.

Remark 5.1. *Comparing the error dynamics of the Peltier system in Eqn. (5.1a) and (5.1b) with the general form in Eqn. (5.8), we have* $a_1(x) = q_3 x_2/q_4/2$, $h_{11} = -q_4$, $a_2(x) = q_8 d/q_9/2$, $h_{22} = -q_9$, $g_{21} = q_{13} x_1$, $h_{21} = q_{14}$, *and*

$$\begin{aligned} f_1(x) &= \dot{r}_1 + q_1 r_1 + q_2 x_1^2 + q_5 r_1 - q_1 x_2 - q_2 x_2^2 - q_5 T_a \\ f_2(x) &= q_6(r_2 - d) + q_7(x_2^2 - d^2) - q_{11}(x_1 - x_2) - q_{12}(x_1^2 - x_2^2) + q_{10}(r_2 - T_a) \end{aligned}$$

From Eqn. (5.9) of the expression of $\bar{u}_i$, *we have*

$$\begin{aligned} \bar{u}_1 &= -h_{11}^{-1}(f_1 - h_{11} a_1^2(x) + \alpha_1 e_1) \\ &= (f_1 + q_3^2 x_2^2/4q_4 + \alpha_1 e_1)/q_4 \\ \bar{u}_2 &= -h_{22}^{-1}(f_2 - h_{22} a_2^2(x) + g_{21} u_1 + h_{21} u_1^2 + \alpha_2 e_2) \\ &= (f_2 + q_{13} x_1 u_1 + q_{14} u_1^2 + q_8^2 d^2/4q_9 + \alpha_2 e_2)/q_9 \end{aligned}$$

Compare $\bar{u}_i$ *with the definition of* $\bar{u}_i$ *as* $(u_i + a_i(x))^2$, *we will have the following equalities*

$$\left(u_1 + \frac{q_3 x_2}{2q_4}\right)^2 = \frac{q_3^2 x_2^2}{4q_4^2} + \frac{f_1 + \alpha_1 e_1}{q_4} \tag{5.13}$$

$$\left(u_2 + \frac{q_8 d}{2q_9}\right)^2 = \frac{q_8^2 d^2}{4q_9^2} + \frac{f_2 + q_{13}x_1u_1 + q_{14}u_1^2 + \alpha_2 e_2}{q_9} \tag{5.14}$$

By direct comparison, we can find that $c_1 = f_1$ and $c_2 = f_2 + q_{13}x_1u_1 + q_{14}u_1^2$, therefore the equalities (5.11) and (5.12) are equivalent to equalities (5.13) and (5.14), which means this algorithm is in fact an extended feedback linearization-based design.

Remark 5.2. *Since the solutions of u_1 and u_2 are obtained from second order equations with parameters depending on the temperatures and errors, the existence of a solution cannot be determined* a priori. *However, since h_{11} and h_{22} are negative, the existence conditions for u_i can be reduced to the positiveness of the right hand side of Eqn. (5.13) and (5.14). Inside the operating range of the system, f_1 and $f_2 + q_{13}x_1u_1 + q_{14}u_1^2$ are positive, therefore for positive errors, the existence conditions of u_i are always satisfied. For negative errors with relatively small magnitude (in our case <5), we can always find a positive upper bound of α_i to guarantee the positiveness. If for some initial value of α_i the existence conditions are not satisfied, we can reduce the α_i value to satisfy the condition (we assume that this case only happens when $e_i < 0$). On the other hand, as the α_i value controls the convergent rate of errors, we would prefer larger α_i values for faster responses. Therefore, the choice of α_i value is a compromise of different requirements and mainly limited by the magnitude of negative errors.*

Remark 5.3. *To decide the sign of the square roots of $(u_i + a_i(x))^2$, signal magnitude and the hardware limitations are considered. At local range with very small e_i, we prefer the one with smaller magnitude for u_1 except the 60°C region, and the one with larger magnitude for u_2. Special attention is focused on the system around 60°C region, where u_1 is close to zero input and may change signs frequently. In this case, we choose the sign of u_1 to be opposite to the sign of $e_1 - e_2$. During transitions, the heat transfer direction is also considered, we will verify the sign of u_1 to be the same as $\dot{r}_1$ if the two roots have different signs. Furthermore in some cases, one of the solution of u_2 may be out of hardware limitation, then we will choose the other solution within the bound during the transition. In most cases, we prefer to use the same sign choice of the square root to avoid jumps on control values.*

The main advantage of this extended feedback linearization-based design is using one controller for all the regions, therefore eliminating the need for multiple sets of controllers for different regions. The coupling effects between two Peltiers and nonlinear characteristics are internally reflected in the controller design. However, the feasibility of this design depends on the existence of a solution of $\bar{u}_i$ which depends on the model parameters, process variables, and tuning parameters. Typical Peltier systems are usually stabilizable, and hardware limitation will be the main limitation on the convergent rate. Since some of the model parameters are state-dependent, robustness analysis will be subjected to different operating conditions, we will discuss this issue by numerical simulations in section 5.4.

5.3 Equivalent design by Lyapunov function theory

The extended feedback linearization-based design assigns negative eigenvalues to the error dynamics to achieve the asymptotic stability of the error system. Similar designs can be obtained from the Lyapunov function method. An equivalent design to the extended feedback linearization design is studied here using a simple control Lyapunov function $V(e, \dot{e}) = \frac{1}{2}(e_1^2 + e_2^2) = V_1 + V_2$. The controller algorithm is developed by forcing the derivatives of each sub-Lyapunov functions to be negative. The viability of this sequential design lies on the strict feedback property of the system. The following theorem provides a set of sufficient conditions for the general controller to stabilize the error dynamics of our Peltier device.

Theorem 5.3. *For the nonlinear system in Eqn.(5.1a) and (5.1b), closed-loop stability is guaranteed if the controller satisfies the following conditions:*

(i) $\begin{cases} q_4 u_1^2 + q_3 x_2 u_1 - (c_1 + \beta_1 e_1) \geq 0 & \textit{if } e_1 \geq 0 \\ q_4 u_1^2 + q_3 x_2 u_1 - (c_1 + \beta_1 e_1) \leq 0 & \textit{if } e_1 < 0 \end{cases}$

(ii) $\begin{cases} q_9 u_2^2 + q_8 d u_2 - (c_2 + \beta_2 e_2) \geq 0 & \textit{if } e_2 \geq 0 \\ q_9 u_2^2 + q_8 d u_2 - (c_2 + \beta_2 e_2) \leq 0 & \textit{if } e_2 < 0 \end{cases}$

where $\beta_1 > -(q_1 + q_5)$ *and* $\beta_2 > -(q_6 + q_{10} + q_{11})$ *are two tuning parameters, and*

$$
\begin{aligned}
c_1 &= \dot{r}_1 + q_1 r_1 + q_2 x_1^2 + q_5 r_1 - q_1 x_2 - q_2 x_2^2 - q_5 T_a \\
c_2 &= q_6(r_2 - d) + q_7(x_2^2 - d^2) - q_{11}(x_1 - x_2) - q_{12}(x_1^2 - x_2^2) + q_{10}(r_2 - T_a) \\
&\quad + q_{13} x_1 u_1 + q_{14} u_1^2
\end{aligned}
$$

are two intermediate variables defined as functions of state, reference and control.

Proof. For the first sub-Lyapunov function V_1, replacing corresponding terms of $\dot{e}_1$ with Eqn. (5.1a), the derivative of this Lyapunov function is

$$\begin{aligned}\dot{V}_1(e_1, e_2) &= -(q_1 + q_5)e_1^2 + (\dot{r}_1 + q_1 r_1 + q_2 x_1^2 + q_5 r_1 - q_1 x_2 - q_2 x_2^2 \\ &\quad -q_5 T_a - q_4 u_1^2 - q_3 x_2 u_1)e_1\end{aligned}$$

which is organized in a descending order of e_1. We define $F_0 = q_1 + q_5$ and F_1 as the coefficient of the e_1 term for simplification. Since $q_1 + q_5 > 0$ is determined by the material property and operating conditions, $F_0 > 0$ is guaranteed. From the definition of c_1, we have $F_1 = -(q_4 u_1^2 + q_3 x_2 u_1 - c_1)$. Therefore, the condition (i) is equivalent to

$$-F_1 \geq \beta_1 e_1, \text{ if } e_1 \geq 0, \quad \text{and} \quad -F_1 \leq \beta_1 e_1, \text{ if } e_1 < 0$$

which is equivalent to $F_1 e_1 \leq -\beta_1 e_1^2$.

If $\beta_1 > -(q_1 + q_5)$, then $\dot{V}_1 \leq -(q_1 + q_5 + \beta_1)e_1^2 \leq 0$.

Similarly for V_2, we assume u_1 is known and substitute $\dot{e}_2$ term with Eqn. (5.1b), we have

$$\begin{aligned}\dot{V}_2(e_1, e_2) &= -(q_6 + q_{10} + q_{11})e_2^2 + (q_6 r_2 - q_6 u_3 + q_7 x_2^2 - q_7 d^2 \\ &\quad -q_{11} x_1 + q_{11} x_2 - q_{12} x_1^2 + q_{12} x_2^2 + q_{13} x_1 u_1 + q_{14} u_1^2 \\ &\quad +q_{10} r_2 - q_{10} T_a - q_8 d u_2 - q_9 u_2^2)e_2\end{aligned}$$

Similar to $\dot{V}_1$, we define $G_0 = q_6 + q_{10} + q_{11}$ and G_1 as the coefficient of e_2. For the Peltier device, G_0 is always positive by the material properties and operating conditions, therefore the first term -$G_0 e_2^2$ is always negative with nonzero e_2. Since the condition (ii) is equivalent to the inequality $G_1 e_2 < -\beta_2 e_2^2$, the derivative of the Lyapunov function V_2 satisfies the following equality,

$$\dot{V}_2 = -G_0 e_2^2 + G_1 e_2 \leq -(q_6 + q_{10} + q_{11} + \beta_2)e_2^2$$

If $\beta_2 > -(q_6 + q_{10} + q_{11})$, then $\dot{V}_2 \leq 0$.

The entire Lyapunov function V can be expressed in matrix form as $\frac{1}{2}e^T e$, and its derivative is expressed as

$$\dot{V} = \dot{V}_1 + \dot{V}_2 \leq -\alpha_1 e_1^2 - \alpha_2 e_2^2 = -\begin{bmatrix} e_1 & e_2 \end{bmatrix} \begin{bmatrix} \alpha_1 & 0 \\ 0 & \alpha_2 \end{bmatrix} \begin{bmatrix} e_1 \\ e_2 \end{bmatrix}$$

where $\alpha_1 = F_0 + \beta_1$ and $\alpha_2 = G_0 + \beta_2$. The overall system is stable by Lyapunov stability theory. □

We can develop a controller by solving the inequality conditions of Theorem 5.3. Equality conditions could be used for simplicity if the existence conditions are satisfied, following sequential algorithm is proposed for the Peltier system.

Algorithm: Lyapunov function-based design

1. Calculate $c_3 = q_1 + q_5$ and $c_4 = q_6 + q_{10} + q_{11}$ and choose $\beta_1 > -c_3$ and $\beta_2 > -c_4$. Although c_3 and c_4 are non-constant, we keep β_i value constant unless we can not obtain a solution with the initial β_i value. Decrease β_i value if no solution exists.

2. Calculate $c_1 = \dot{r}_1 + q_1 r_1 + q_2 x_1^2 + q_5 r_1 - q_1 x_2 - q_2 x_2^2 - q_5 T_a$.

3. Fill in the values of c_1 and e_1 into the following equality

$$\left(u_1 + \frac{q_3 x_2}{2q_4}\right)^2 = \left(\frac{q_3 x_2}{2q_4}\right)^2 + \frac{c_1 + \beta_1 e_1}{q_4} \tag{5.15}$$

   and solve the equation to obtain u_1. The sign of u_1 is determined by the operating condition and the magnitude is limited by constraints. $\tilde{u}_1 = \min(u_{1max}, u_1)$, if $u_1 \geq 0$, and $\tilde{u}_1 = \max(u_{1min}, u_1)$, if $u_1 < 0$.

4. Calculate $c_2 = q_6(r_2 - d) + q_7(x_2^2 - d^2) - q_{11}(x_1 - x_2) - q_{12}(x_1^2 - x_2^2) + q_{10}(r_2 - T_a) + q_{13} x_1 \tilde{u}_1 + q_{14} \tilde{u}_1^2$.

5. Fill in the values of c_2 and e_2 into the following equality

$$\left(u_2 + \frac{q_8 x_d}{2q_9}\right)^2 = \left(\frac{q_8 d}{2q_9}\right)^2 + \frac{c_2 + \beta_2 e_2}{q_9} \tag{5.16}$$

   and solve the equation to obtain u_2. Apply constraints of u_2 to the solution and get $\tilde{u}_2$ similarly.

Remark 5.4. *The replacement of inequalities in Theorem 5.3 with equality conditions can avoid the pre-determination of the sign of e_i and simplify steps for testing of the inequality conditions. However, the new equality constraints reduce the search range, and may be insolvable in specific problems. We assume the existence of a solution in this algorithm description.*

Remark 5.5. *The equivalence of this Lyapunov function-based design to the extended feedback linearization-based design is straightforward by comparing Eqn. (5.15) and (5.16) to Eqn. (5.11) and (5.12). However, since the parameter β_i in this algorithm is not defined as the closed-loop eigenvalue, it partially utilizes the characteristics of the error dynamics and therefore has a larger range than α_i (Term $F_0 e_1^2$ and $G_0 e_2^2$ provide some stability margins).*

We introduced a Lyapunov function-based designs here to provide more control design options over the feedback linearization-based which will depend on the selection of specific Lyapunov function. Here a simple Lyapunov function candidate is used to develop an equivalent algorithm to the feedback linearization design. Using the same Lyapunov function with some pre-determined controller structure restrictions, other controllers can be developed and their performance are comparable with the feedback linearization-based design with same tuning parameters.

5.4 Simulation results and robustness analysis

5.4.1 Simulation results under perfect model assumption

We apply the extended feedback linearization-based controller algorithm to the theoretical model simulated in Simulink® 7.0. Fixed-step size simulation is chosen to match with the sampling time used in the measurement. A new reference is introduced in the nonlinear design to generate error signal, and the values of the reference and the first derivative signal are calculated at each simulation step and used in the controller algorithm. Since the first heating before the 94°C set-point starts from 60°C while in later cycles the heating starts from 72°C. A separate reference signal is also developed for the initial transition from 60 to 94°C and we

exclude this transition from regular cycle and use the beginning of the 94°C local region as the start of a cycle and end the cycle after the transition from 72 to 94°C, which is different with the linear switching controller. The flowchart of the controller implementation is illustrated in Fig. 5.1.

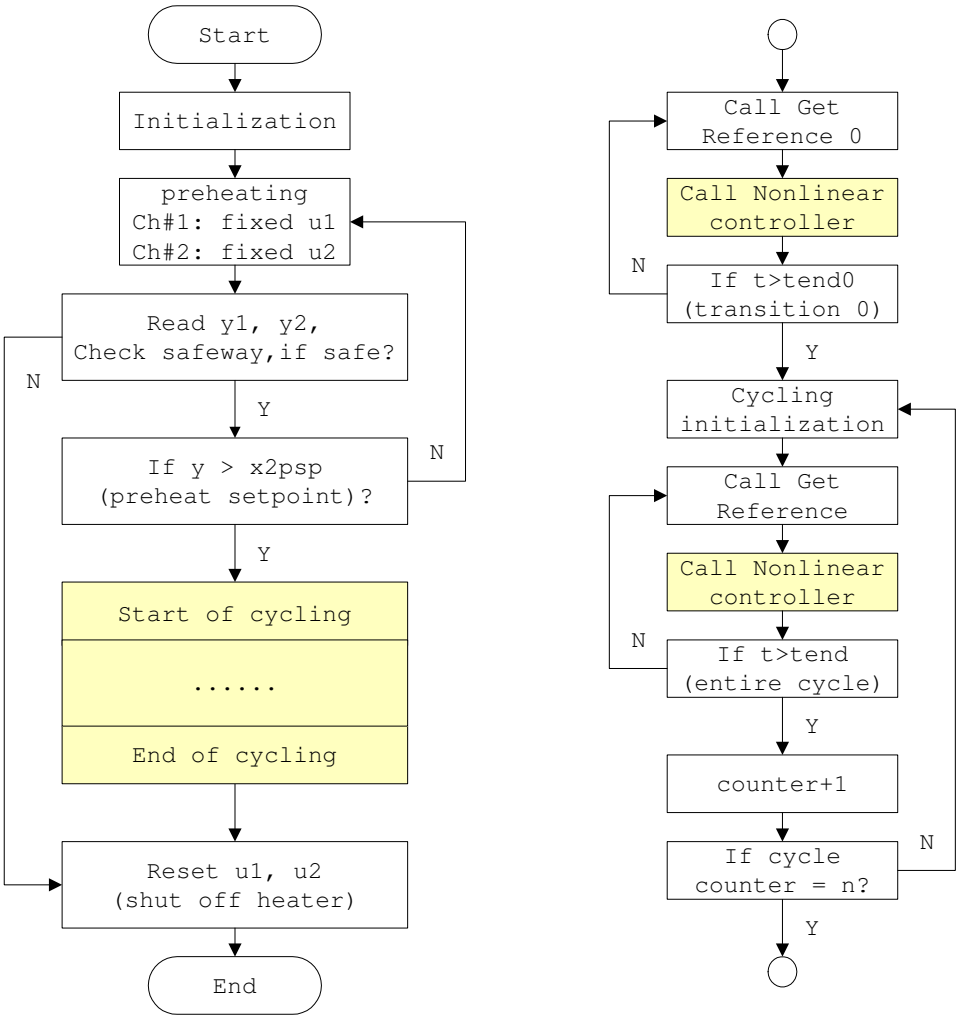

Figure 5.1: Flowchart diagram of the nonlinear non-switching controller. The first transition is separated from the regular cycling with a different reference.

In the controller algorithm, we update all of q_i values at each sampling instance but q_5 and q_{10} values in the simulated model. Because unlike other q_is which can be easily calculated as functions of temperature, there are no simple formula available for q_5 and q_{10}. They are functions of $(x, \dot{x}, u)$ and both $\dot{x}$ and u vary largely during transition. In addition, not direct measurement of $\dot{x}$ is available. If we calculate the approximated $\dot{x}$ values to determine q_5 and q_{10}, the dynamic system model are used

inside the controller. Therefore the controller algorithm will include the calculation of the $\dot{x}$ and further assigning q_5 and q_{10} values based on approximated $\dot{x}$ and measured u using look-up tables. The controller algorithm will be more complicated and time-consuming. Instead, using constant values to simplify the controller algorithm is reasonable in practice. However, the feasibility of this simplification depends on the robustness of the controller with certain model uncertainties and needs to be verified by real system parameters. The tuning parameters α_1 and α_2 are initially set to 1. In determining the shape of the newly introduced reference, we choose to set the slope of the ramp function at a bit steeper than the slope limited by hardware. Therefore positive e_1 will be observed during the heating transition which will lead the controller to achieve fast transition. Meanwhile, the range of feasible α_i values will be also much larger with positive e_1 values. The simulated closed-loop system responses of two measured temperatures are shown in Fig. 5.2.

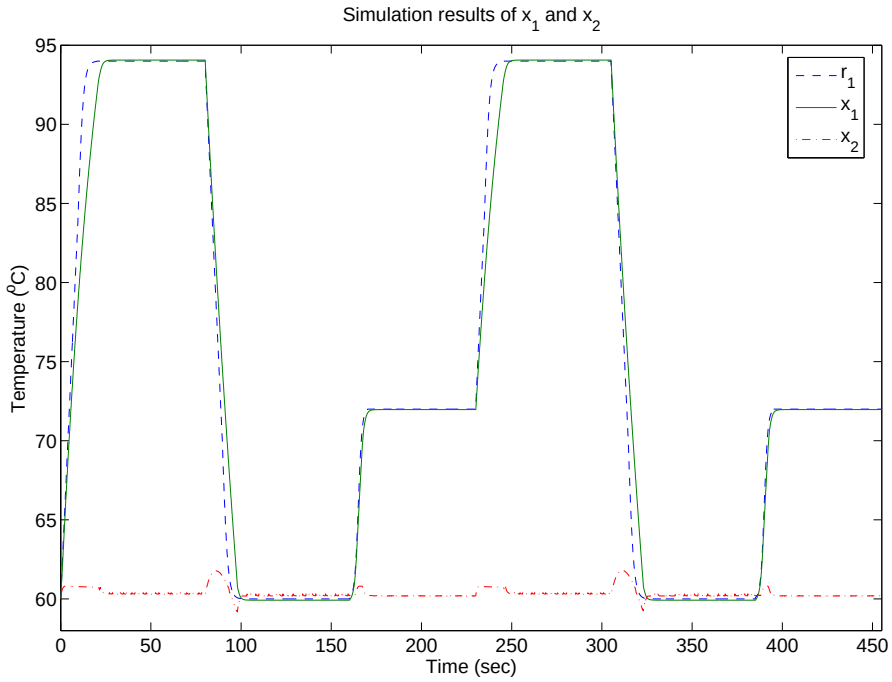

Figure 5.2: Simulated closed-loop response of the two-stage Peltier device using an extended feedback linearization controller: (dashed) new reference signal, (solid) top Peltier temperature x_1, (dash-dotted) bottom Peltier temperature x_2.

In Fig. 5.2, we observe that the closed-loop response tracks the reference closely.

No discernable overshoot appears in x_1 after each transitions, which achieves one of our objective to reduce the overshoot found in the closed-loop response of earlier linear switching PID design [35] (Fig. 4.7 includes experimental results using that type of linear switching PID design). The tracking errors are relatively larger during the transitions than local regions, where the maximum tracking errors of e_1 is about ± 5°C observed during the transitions from 72 to 94°C and from 94 to 60°C. The tracking errors are smaller ($\pm$1°C) during the transition from 60 to 72°C. The relatively larger errors found during transition are mainly due to the limitation of the maximum heating/cooling ability when our preset slope cannot be reached by the device over a large variation range. The temperature regulation result of x_2 also improves significantly compared to the performance using our earlier decentralized switching PI/PD controller design. Maximum error of x_2 is reduced from $\pm$5°C to $\pm$2°C. The reduction of variation range of the bottom Peltier temperature indirectly benefits the fast settling of the top Peltier temperature. However, steady-state errors (about 1°C) are found in the simulated results of x_2. Overall, using the new extended feedback linearization-based controller, variation ranges of both states are significantly reduced, oscillations are eliminated, therefore fast and smooth transition are achieved in both Peltiers. The feasibility of using constant q_5 and q_{10} for the design simplification is also validated by the simulation results.

5.4.2 Model uncertainty and robustness analysis

The earlier simulations assume that there are no modeling errors, while for model-based controller designs, the effect of model uncertainty on the closed-loop performance should be further studied. For linear systems, usually stability margin of the closed-loop system are calculated and the corresponding parameter ranges can be derived. For nonlinear systems, the robustness analysis will be more difficult, and usually the concept of regions of attraction are used which will depend on different choice of Lyapunov functions. Usually the domain of feasible control u will be functions of system dynamics and specific Lyapunov functions. For this Peltier-based system, we study the robustness of nonlinear controller using numerical simulations.

First of all, except for q_5 and q_{10}, the other twelve parameters are functions of material properties and Peltier surface temperatures, we can calculate the relative deviations of parameters $\delta q_i/q_i$ when the states have some mismatch with the nominal steady-states. From the definitions of q_i in Table 4.2, q_1-q_4 and q_{11}-q_{14} depend on (x_1, x_2), while q_6-q_9 depend on (x_2, d). Therefore, we could choose some nominal values of (x_1, x_2, d) to determine normal q_i values. By applying a grid with different level of deviation on the plane of either (x_1, x_2) or (x_2, d), we can calculate the effect of q_i due to the deviation.

Since the drifting of d during regular PCR cycles are not large (less than 5°C), and the errors of both x_1 and x_2 in the closed-loop system is also less than 5°C (less than 1°C at local regions), we initially apply a two-dimension grid over [-5,+5] on the nominal steady-state temperatures and study the effect on parameter deviations. Since r_2 is constant, and the drifting of d is relatively small, we use $(x_2, d)_{ss} = (60, 25)$ as our nominal values. The corresponding parameter deviations are shown in Fig. 5.3. The largest relative deviation is found on q_6 which is less than 2%. The deviations on other three parameters are much smaller.

The parameters of the top Peltier is more complicated since x_1 tracks the reference over about 40 degree range. And the relative parameter deviations will be function of different nominal x_1 value. To study the effect of the temperature deviation, we also apply a two-dimension grid over [-5,+5] on the nominal pair of (x_1, x_2). The relative deviations of q_1 to q_4 at $(94, 60)$ operating point are shown in Fig. 5.4. Unlike 5.4(a) where $\delta q_1/q_1$ is plotted, Fig. 5.4(b)-Fig. 5.4(d) show $-\delta q_2/q_2$ to $-\delta q_4/q_4$ to highlight the appearance of largest deviations at the vertices (the largest deviations can not be seen in original $\delta q_2/q_2$ to $\delta q_4/q_4$ plots). For all of the four parameters, we found the largest relative deviations happen at either (-5,-5) or (+5,+5) vertex, therefore we choose to calculate the relative deviations of parameters only at these two points. The profiles of the deviations of the two vertices along the x_1 axis between 55 to 95 can be obtained. Fig. 5.5(a) shows the trajectory of $\delta q_i/q_i$ at the vertex (+5,+5) along the x_1 axis with fixed $x_2 = 60$, while Fig. 5.5(b) shows the trajectory of $\delta q_i/q_i$ at the vertex (-5,-5). From Fig. 5.5, we found the largest relative deviations are always less than 3% for q_1 to q_4 along the

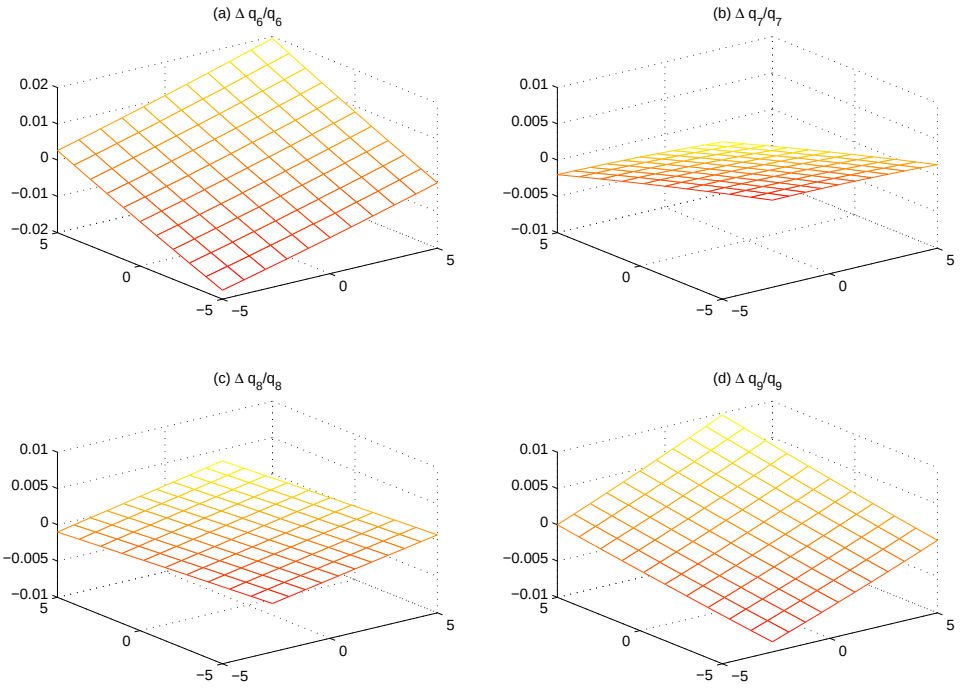

Figure 5.3: Relative parameter deviations of q_6 to q_9 over a -5 to 5 grid around (60,25)

x_1 axis ($x_1 \in$[55, 95]).

Since by definition $q_1/q_{11} = q_2/q_{12} = q_3/q_{13} = q_4/q_{14}$, the relative deviation levels of q_{11}-q_{14} will be same as q_1-q_4 respectively. For all of the twelve temperature-dependent parameters the relative deviations due to the [-5,+5] temperature discrepancy will be less than 3%. Similar procedures are applied with [-10,+10] grid, and the corresponding relative parameter deviations are less than 6%.

Next, we further run simulations to verify the effect of parameter deviations on the closed-loop performance. Relative parameter deviation levels at $\pm$3%, $\pm$6%, and $\pm$10% are chosen, since 3% is the maximum deviation due to $\pm$5°C deviation from nominal state values, 6% is the maximum deviation for $\pm$10°C case. By choosing 10% as the largest level for simulation, we are confident the worse cases due to model uncertainty are covered. We intentionally change the q_i values in the controller algorithm by the chosen deviation levels and perform closed-loop system

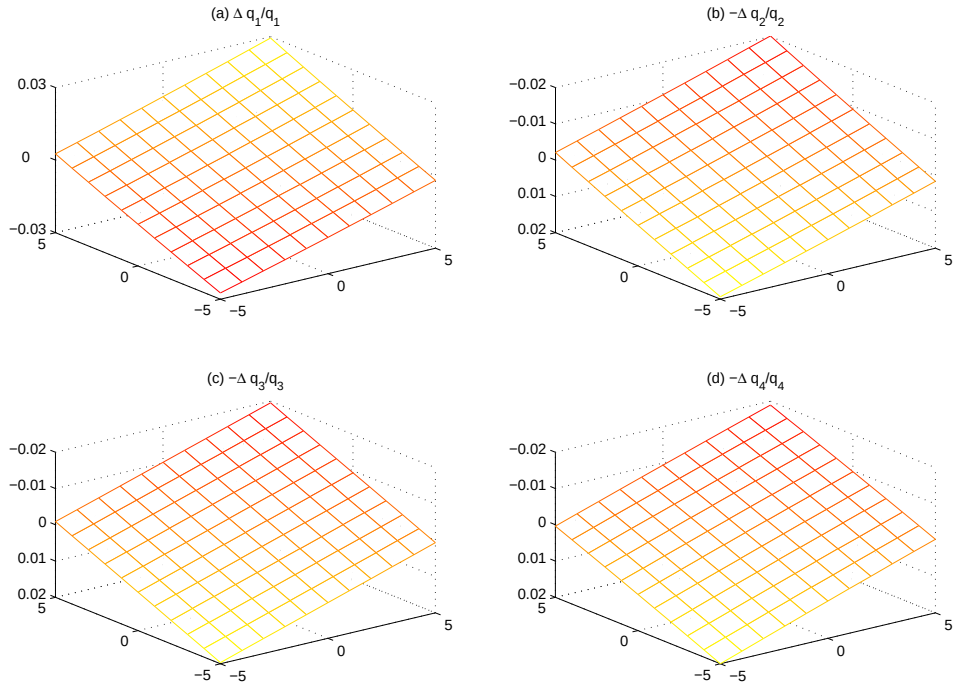

Figure 5.4: Relative parameter deviations of q_1 to q_4 over a -5to 5 grid around (94,60)

simulations. For all these cases, the closed-loop stabilities are always preserved, therefore we can confident that the stability margin of the system is large enough for these levels of model/controller parameter discrepancy. The existence of parameter deviations leads to the difference on the magnitude of the steady-state errors. The largest steady-state errors about $\pm$0.2°C are observed at the 94°C region with $\pm$10% parameter deviation, which are acceptable for current PCR operation.

However, as a preventive measure to deal with the steady-state errors due to model/controller parameter mismatch at local ranges, we considered to include some bias tracking techniques. High gain proportional controllers are introduced at local regions to reduce the errors. The new local controller will be

$$u_{1hg} = u_1 + K_{c1}e_1 \tag{5.17a}$$

$$u_{2hg} = u_2 + K_{c2}e_2 \tag{5.17b}$$

For $\pm$10% deviation case, we use $K_{c1} = K_{c2} = [600, 3000, 6000]$ respectively, and the corresponding steady-state errors of e_1 are reduced from 0.2 to

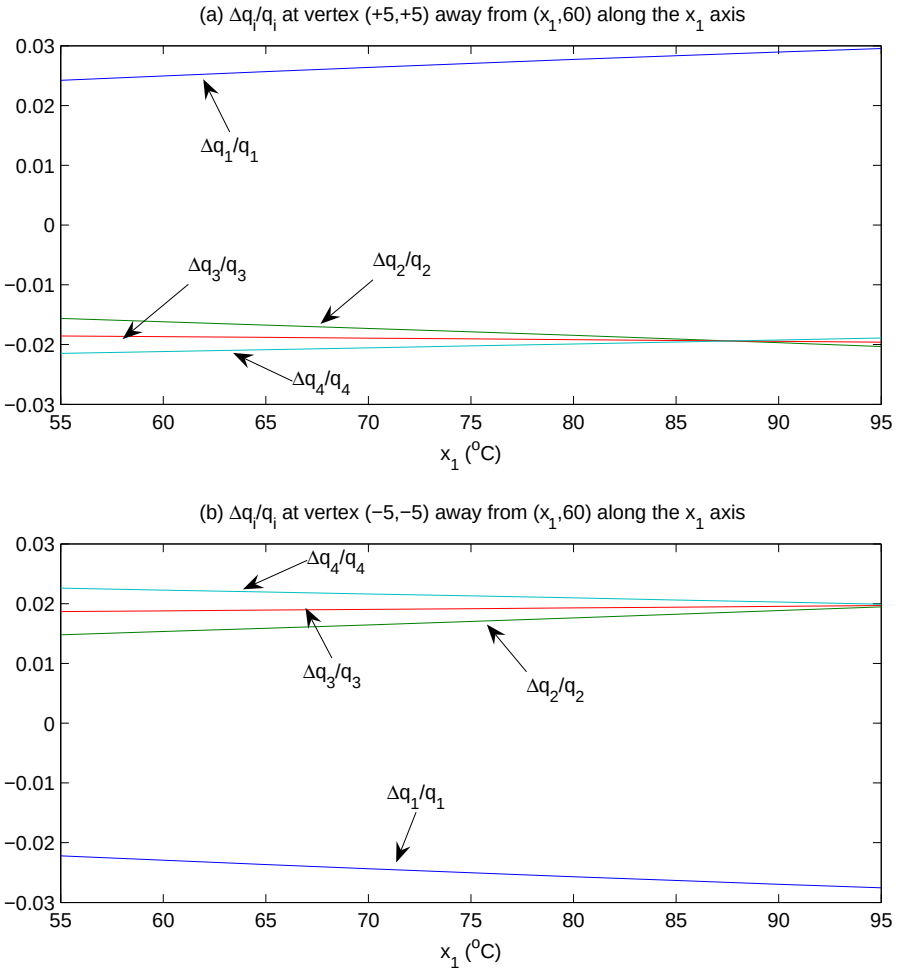

Figure 5.5: Relative parameter deviations of q_1 to q_4 at the two vertices (-5,-5) and (+5,+5) along the x_1 axis

$[0.080, 0.035, 0.018]$ respectively. Although from the theory, the higher the gain the smaller the steady-state error, we avoid too large gain value due the the bound of control signal [0, 4095]. To apply the new local controller, the choice of switching time will be also important. The main guide line here is to delay the inclusion of high gain part as later as possible since high gain part usually will lead to extreme large value when error is large which may cause overshoot at the end of transition. Integral control could also be introduced locally to remove the steady-state error, however we will prefer quick settling from high gain controller over slow integration process as we only intend to use them when errors are already very small.

5.5 Experimental results

The algorithm of the extended feedback linearization design was coded in C and implemented in a PIC micro-controller. A sampling time of 0.1 second is used for the controller. Both control signals and measured temperature data are recorded. The local high gain controller is coded as an option for inclusion where the turn-on times are to be determined by experimental observations.

Measured temperature outputs of the extended feedback linearization-based design without local high gain controller are shown in Fig. 5.6, which includes six PCR cycles. The corresponding control inputs are shown in Fig. 5.7. The temperature outputs of the top Peltier around the three set-points are shown in Fig. 5.8(a)-(c) respectively, while the temperature output of the bottom Peltier is shown in the zoomed-in range in Fig. 5.8(d). In the measurement of x_1, relatively larger steady-state errors (about 0.4-0.5°C) are observed in the local ranges compared to closed-loop simulation response. The initial overshoot is about 0.5-0.6°C. The value of α_1 is further increased in the local range, but no significant reduction in the magnitude of the steady-state errors is achieved. Although the steady-state errors of x_1 are relatively large, the relative overshoot over the steady-state temperature is very small which is bounded by $\pm$0.1°C. Reduced overshoots and steady-state errors are also observed in x_2. The steady-state errors of x_2 are bounded by $\pm$0.4°C, while the maximum errors during transition are bounded by $\pm$2°C, except the large drop below 55°C in the beginning of the transition 0. This large temperature drop is due to the limitation of the heat generation rate of the device in the extreme heating of the top Peltier. Since the steady-state errors are within tolerable bound for current PCR application, we did not include the local high gain option. Overall, smooth transitions and set-point regulations are achieved in the criteria of overshoot and steady-state errors.

Fast transition is also achieved in the sense of the settling time. Compared to the linear switching decentralized controller, the rise time observed in x_1 is about 2-3 seconds slower, which is due to the tradeoff between small overshoot and fast transition. However, by eliminating the oscillations after the first overshoot found

in linear designs, the rise time and the settling time in this case have the same value. Therefore, the settling time is significantly reduced by about 8-10 seconds.

Differences are also found in the control inputs (as the input to a 12-bit D/A converter, the range is [0, 4095]). The u_2 value is close to zero (about 100) only for a short time span during the cooling transition and coupling effects are included in the controller algorithm. While in earlier switching decentralized PID design, due to lack of models of the entire transition region, the u_2 value is set to zero for a much longer time, and after that fixed compensation terms are added to the regular controller output to counteract the coupling until the end of transition. The utilization of nonlinear model for the transition regions helps achieve less variations in u_2 which further contribute to the smooth transition in x_2. In addition, look-up tables for different heat sink temperatures are avoided in this nonlinear design. Experimental results validate the simulation results of the improved transition performance using the nonlinear feedback linearization-based controller.

5.6 Summary

In this chapter, the characteristics of the dynamics of the error models are studied. Based on the strict feedback property, the MIMO controller design can be solved by sequential SISO designs. For each SISO sub-system, square terms of u_i are transformed into a new fictitious control by completing of square. Input-to-state feedback linearization technique is applied to each transformed SISO nonlinear control affine system to obtain a simple and easily extendable design. An extended feedback linearization-based for the MIMO system is formulated, and the existence conditions of the transformation and the sufficient conditions of the closed-loop stability are proposed. An equivalent design from Lyapunov stability theory is also developed which includes the feedback-linearization design as a special case and provides more information about the tuning parameters.

Model parameter uncertainties are studied for typical PCR operating conditions. Simulations results show that the closed-loop stability is preserved within 10% parameter discrepancy. The effect of parameter discrepancy are mainly observed on

the magnitude of the steady-state errors. The larger the parameter discrepancy, the larger the steady-state error. An optional local high gain proportional controller is proposed to reduce the steady-state error and the effectiveness of this strategy is verified by simulations. Further experimental results validated the improvement of the nonlinear design. Significantly reduced overshoots and no further oscillation at local range are observed using the controller compared to earlier linear model-based switching PID controller design. Settling times are reduced by 8-10 seconds at different local regions from the switching PID design. In addition, since this nonlinear design incorporates the coupling effects internally, much smaller variations are found in the bottom Peltier, which indirectly helps the smooth transition in the top Peltier.

Although comparable performance may also be achieved using linear switching design with further fine-tuning. By using a single nonlinear controller with parameters updated online, the controller implementation is much simpler and those look-up tables and local controller parameters tunings can be avoided. Furthermore, since the nonlinear model is not limited to a small local region, the nonlinear model-based controller can be applied to different set-points or references without the necessity of local model re-identification and parameter tuning. With the simple controller structure, and the large application range of the model, this nonlinear controller design are readily to be used in other reference settings or biochemical reactions beyond PCR applications.

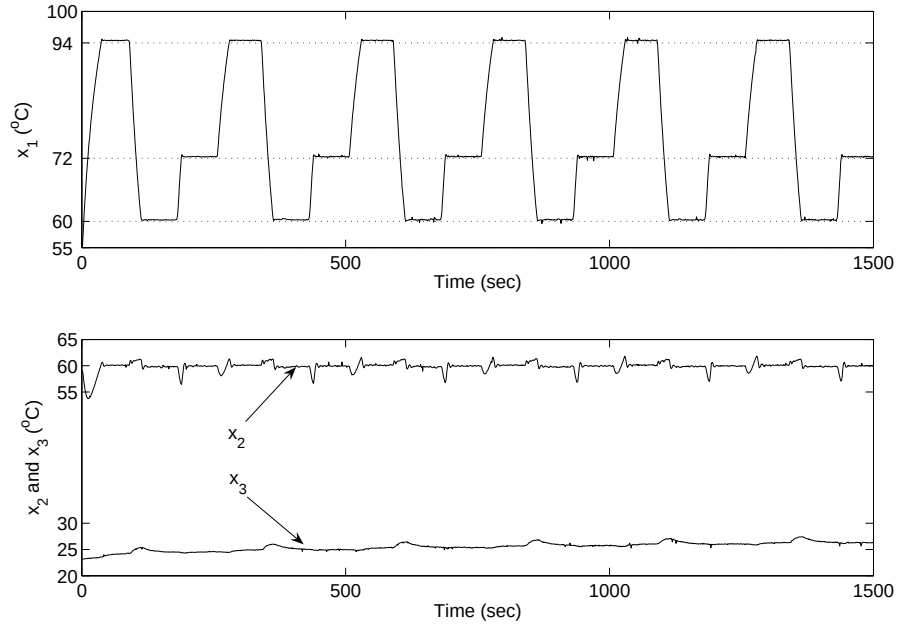

Figure 5.6: Measured outputs using an extended feedback linearization controller for six PCR cycles: (top graph) temperature of the top Peltier x_1, (bottom graph) temperature of the bottom Peltier x_2 and heat sink x_3.

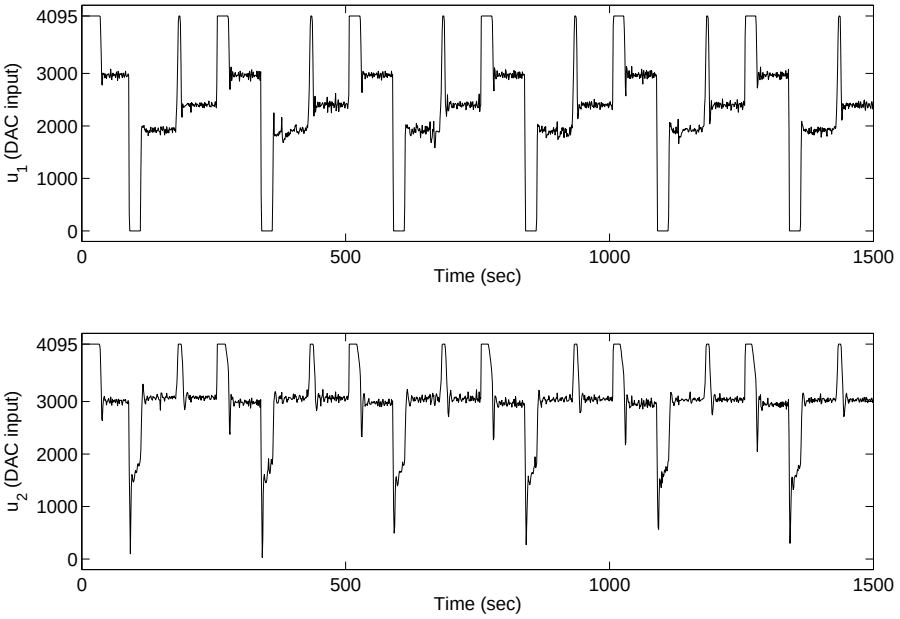

Figure 5.7: Digital control inputs using an extended feedback linearization controller for six PCR cycles: (top graph) 12-bit DAC input for the top Peltier u_1, (bottom graph) 12-bit DAC input for the bottom Peltier u_2.

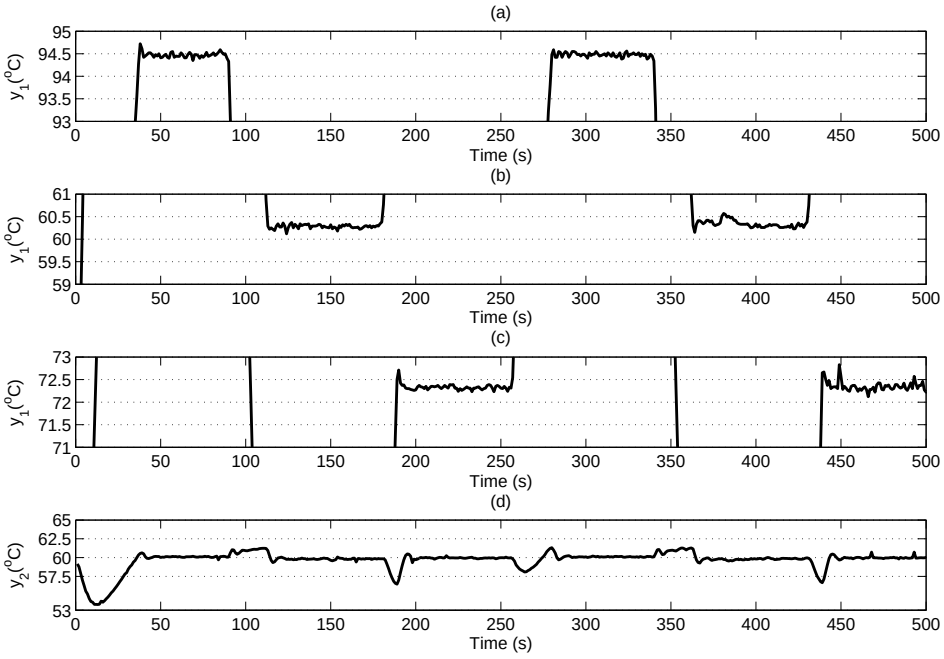

Figure 5.8: Measured outputs at local regions for two representative PCR cycles using an extended feedback linearization controller. (a) x_1 around the 94°C region; (b) x_1 around the 60°C region; (c) x_1 around the 72°C region; (d) x_2 around the 60°C region;

Chapter 6

Nonlinear switching pseudo-PID controller design

In the previous chapter, we developed a nonlinear feedback-linearization based controller for the temperature control of the PCR cycler with improved closed performance and simplicity in design and implementation. The extension of the input-to-state feedback linearization depends on the feasibility of completing the square to transform the u and u^2 term to a new fictitious $\bar{u}$. Constraints are included in the design implicitly. For a general nonlinear system, Lyapunov function based design usually can deal with all non-conventional characteristics explicitly. For comparative study, we also developed an equivalent algorithm to the extended feedback linearization-based design using Lyapunov function method. No constraints of specific controller structure are enforced in the design, therefore nonlinear equations are to be solved at each iteration in digital control implementation. This repeated online calculation may be redundant when the system is very close to the steady-state. As an alternative, certain simple controller with fixed parameters could be considered in the local stabilization to reduce the online calculation burden. In some applications with a faster sampling rate requirement or with limited resources for online calculation, applying a local time-invariant controller may be necessary.

On the other side, the possible model parameter uncertainty will affect the performance of the model-based controller design. In the previous chapter, we found that steady-state errors will increase when the model/controll parameter discrepancy increases by simulations. Some bias tracking or steady-state error reduction

measures may be needed which will be also included in the choice of controller structure.

In this chapter, we consider to develop a switching nonlinear controller which uses nonlinear algorithms to improve the transition performance and linear counterpart to save the local calculation and reduce the steady-state error. Considering the simplicity of the local controller, the convenience of parameter setting at the switching time, and the minimization of steady-state errors, a pseudo-PID/ state feedback design is developed in this chapter.

6.1 A pseudo-PID/ state feedback design by Lyapunov function theory

With the intention to have the controller parameter numbers as few as possible and the ability to reduce steady-state errors, a PID controller structure is first considered. In addition, due to the strong coupling between two Peltier modules during the transitions, cross state terms are also needed to be considered. Furthermore, since we want to develop nonlinear model-based controllers to improve the transition performance and avoid intensive tuning efforts, the smooth switching from a nonlinear controller to a linear controller, and the quick algorithm to determine the parameters of local controllers are also important factors to determine the controller structure. Combining all these objectives, we propose a nonlinear controller with a special structure for the Peltier device. A combination of pseudo-PID controller and state feedback controller is chosen here. State feedback is usually the first choice, while the derivative term and the bias term are included for non-constant reference tracking. Therefore, the following controller structure with seven controller parameters is proposed

$$u_1 = k_0\dot{r}_1 + k_1e_1 + k_2e_2 + k_3 \tag{6.1a}$$

$$u_2 = l_1e_1 + l_2e_2 + l_3 \tag{6.1b}$$

where k_1, k_2, l_1, l_2 are the state feedback gains, k_3 and l_3 are the bias terms due to non-constant reference tracking, and k_0 is the derivative gain which only appears in u_1. We use $\dot{r}$ instead of $\dot{x}$ since the rate of temperature change is not measured, and

the value of our proposed $\dot{r}$ is easy to calculate. This approximation will be feasible during transitions when $\dot{e} \ll \dot{r}$. Unlike u_1, there is no $\dot{r}_1$ related term in u_2 because $\dot{e}_2$ does not rely on $\dot{r}_1$ directly (no explicit terms of $\dot{r}_1$ appears in dynamic equation of $\dot{e}_2$ in Eqn. (5.1b)).

Although k_is and l_is in our controller are actually functions of states and inputs, we treat them as controller parameters and can find similarity of this controller to the PID controller. Therefore, we name this controller as pseudo-PID type controller due to the similarity. u_1 is similar to a PID controller while u_2 is similar to a PI controller except the the cross terms $k_2 e_2$ and $l_1 e_1$. The state feedback terms $k_1 e_1$ and $l_2 e_2$ are equal to the proportional part. The terms k_3 and l_3 are the bias terms which are not constant and are updated with new error information, so in some sense they can be viewed as the integral part. The $k_0 \dot{r}_1$ in u_1 can approximate $k_0 \dot{x}_1$ as the derivative part of a PID controller. At local regions, when those parameters k_1 and l_1 are fixed, and additional integrations introduced to replacing the bias tracking term k_3/l_3, the pseudo-PID controller is a PI controller plus a cross state feedback term.

Enforcing a specific controller structure will apply more constraints to the controller design. Here, Lyapunov function-based designs are considered to develop the corresponding algorithms. Usually, more parameter numbers will lead to more complicated algorithms especially for high dimension systems. Therefore, we tried to minimize the parameter numbers as few as possible, and this type of design is more suitable for lower order one-stage, or two-stage Peltier-based devices.

Next we choose the Lyapunov function of each subsystem as $V_i(e) = \frac{1}{2} e_i^2,\ i = 1, 2$, which is a simple and popular candidate. In addition, this same Lyapunov function is used earlier to develop an equivalent algorithm to the extended feedback linearization-based design, therefore the performance of the new controller is comparable to the earlier one in the sense of Lyapunov stability. The derivatives of the two V_is are derived, both the expressions of u_i and the corresponding u_i^2 are filled

into the $\dot{V}_i$, where u_i^2 are expanded as follows,

$$\begin{aligned} u_1^2 &= k_0^2\dot{r}_1^2 + 2k_0\dot{r}_1k_1e_1 + 2k_0\dot{r}_1k_2e_2 + 2k_0\dot{r}_1k_3 + k_1^2e_1^2 \\ &\quad +2k_1e_1k_2e_2 + 2k_1e_1k_3 + k_2^2e_2^2 + 2k_2e_2k_3 + k_3^2 \\ u_2^2 &= l_1^2e_1^2 + l_2^2e_2^2 + 2l_1l_2e_1e_2 + 2l_1l_3e_1 + 2l_2l_3e_2 + l_3^2 \end{aligned}$$

By organizing in descending order of e_i, we have

$$\begin{aligned} \dot{V}_1(e_1,e_2) &= -(q_4k_1^2+q_2)e_1^3 - (q_2+q_4k_2^2-q_3k_2)e_1e_2^2 + (q_3-2q_4k_2)k_1e_1^2e_2 \\ &\quad -(q_1+q_5+2q_2r_1+q_3r_2k_1+2q_4k_0\dot{r}_1k_1+2q_4k_1k_3)e_1^2 \\ &\quad +(q_1+2q_2r_2-q_3r_2k_2+(q_3-2q_4k_2)k_0\dot{r}_1+(q_3-2q_4k_2)k_3)e_1e_2 \\ &\quad +(\dot{r}_1+q_1r_1+q_5r_1-q_5T_a-q_1r_2+q_2r_1^2-q_2r_2^2-q_3r_2k_0\dot{r}_1 \\ &\quad -q_3r_2k_3-q_4k_0^2\dot{r}_1^2-2q_4k_0\dot{r}_1k_3-q_4k_3^2)e_1 \end{aligned}$$

Four new variables $c_i,\ i=0,\cdots,3$ are introduced to represent the coefficients of the terms in $\dot{V}_1$,

$$\begin{aligned} c_0 &= q_4k_1^2e_1^2 + q_4k_0^2\dot{r}_1^2 \\ c_1 &= q_1+q_5+2q_2r_1+q_3r_2k_1+2q_4k_0\dot{r}_1k_1+2q_4k_1k_3 \\ c_2 &= 1-q_3r_2k_0-2q_4k_0k_3 \\ c_3 &= q_1r_1+q_5r_1-q_5T_a-q_1r_2+q_2r_1^2-q_2r_2^2-(q_1+2z_1e_2)e_2+z_1^2e_2^2+q_2e_1^2 \end{aligned}$$

The derivative can be expressed as

$$\dot{V}_1(e_1,e_2) = -c_1e_1^2 + (-c_0+c_2\dot{r}_1-c_3)e_1.$$

If $\dot{V}_1 \leq 0$, the error system is stable. Therefore, a set of sufficient conditions of the closed-loop Lyapunov stability can be expressed in terms of c_i. Since the coefficients of $e_1^2e_2$ and $e_1e_2^2$ only depend on k_2, by setting $q_3-2q_4k_2=0$ we can remove the cross term $e_1^2e_2$ and simplify $e_1e_2^2$ and e_1e_2 terms. A new set of sufficient conditions for the stability of subsystem of e_1 with additional constraint $k_2=q_3/2q_4$ is proposed in the following theorem.

Theorem 6.1. *Applying a controller constructed as Eqn. (6.1a) with $k_2=q_3/(2q_4)$ to the error system as Eqn.(5.1a), if for some $\alpha_1>0$, $0\leq\delta_+<\alpha_1$, and $0\leq\delta_-<\alpha_1$, there exists some k_0,k_1,k_3 satisfying the following conditions,*

(i) $c_1 \geq \alpha_1$

(ii) $\begin{cases} c_0 + c_3 - c_2\dot{r}_1 - \delta_+ e_1 \geq 0 & \textit{if } e_1 \geq 0 \\ c_0 + c_3 - c_2\dot{r}_1 - \delta_- e_1 \leq 0 & \textit{if } e_1 < 0 \end{cases}$

then the subsystem of e_1 *is exponentially stable and has a convergent rate faster than* $e_1^{-2\alpha_1 t}$.

Proof. If the conditions in (ii) are satisfied, we have

$$-(c_0 + c_3 - c_2\dot{r}_1)e_1 \leq -\min(\delta_+, \delta_-)e_1^2$$

Therefore $\dot{V}_1 \leq -(c_1 + \min(\delta_+, \delta_-))e_1^2$. Applying condition (i), $c_1 \geq \alpha_1 > 0$, we have $\dot{V}_1 \leq -\alpha_1 e_1^2$ when $e_1 \neq 0$, and $\dot{V}_1 = 0$ when $e_1 = 0$. Since $V_1 = \frac{1}{2}e_1^2$, then $\dot{V}_1 \leq -2\alpha_1 V_1$, which means e_1 is exponentially stable with a convergent rate faster than $e_1^{-2\alpha_1 t}$. □

Assuming the existence of a solution for u_1, then we can design u_2 to satisfy $\dot{V}_2 < -\alpha_2 e_2^2$. Substitute u_2 and u_2^2 into $\dot{V}_2$ and combine terms, we have $\dot{V}_2$ as follow,

$$\begin{aligned} \dot{V}_2(e_1, e_2) &= \big\{-q_9(l_2e_2 + l_1e_1)^2 - q_{12}e_1^2 + (q_{11} + 2q_{12}r_1 - q_8l_1d - 2q_9l_3l_1)e_1 \\ &\quad -(q_6 + q_{10} + q_{11} + 2q_7r_2 + 2q_{12}r_2 + q_8l_2d + 2q_9l_3l_2)e_2 + (q_6r_2 \\ &\quad -q_6d + q_7r_2^2 - q_7u_3^2 - q_{11}r_1 + q_{11}r_2 - q_{12}r_1^2 + q_{12}r_2^2 + q_{10}r_2 \\ &\quad -q_{10}T_a + q_{13}r_1u_1 + q_{14}u_1^2 - q_8dl_3 - q_9l_3^2 + (q_7 + q_{12})e_2^2)\big\}\, e_2 \end{aligned}$$

Four variables $d_i,\ i = 0, \cdots, 3$ are defined to simplify the notation of $\dot{V}_2$.

$$\begin{aligned} d_0 &= q_9(l_2e_2 + l_1e_1)^2 + q_{12}e_1^2 \\ d_1 &= q_6 + q_{10} + q_{11} + 2q_7r_2 + 2q_{12}r_2 + q_8l_2d + 2q_9l_3l_2 \\ d_2 &= q_{11} + 2q_{12}r_1 - q_8l_1d - 2q_9l_3l_1 \\ d_3 &= -q_6r_2 + q_6d - q_7r_2^2 + q_7d^2 + q_{11}r_1 - q_{11}r_2 + q_{12}r_1^2 - q_{12}r_2^2 - q_{10}r_2 \\ &\quad +q_{10}T_a - q_{13}r_1u_1 - q_{14}u_1^2 - (q_7 + q_{12})e_2^2 + q_8dl_3 + q_9l_3^2 \end{aligned}$$

Using these new variables, $\dot{V}_2$ can be expressed as

$$\dot{V}_2(e_1, e_2) = -d_1e_2^2 - (d_0 - d_2e_1 + d_3)e_2$$

If $\dot{V}_2 \leq 0$, then e_2 is stable. The sufficient conditions for the closed-loop stability can be expressed in terms of d_is.

A new set of sufficient conditions for the stability of e_2 is proposed in terms of d_i in the following theorem.

Theorem 6.2. *Applying a controller constructed as Eqn. (6.1b) to the error system in Eqn. (5.1b), if for some $\alpha_2 > 0$, $0 \leq \delta_+ < \alpha_2$, and $0 \leq \delta_- < \alpha_2$, there exists some l_1, l_2, l_3 satisfying the following conditions:*

(i) $d_1 \geq \alpha_2$

(ii) $\begin{cases} d_0 + d_3 - d_2 e_1 - \delta_+ e_2 \geq 0 & \text{if } e_2 \geq 0 \\ d_0 + d_3 - d_2 e_1 - \delta_- e_2 \leq 0 & \text{if } e_2 < 0 \end{cases}$

then the subsystem of e_2 is exponentially stable and has a convergent rate faster than $e_2^{-2\alpha_2 t}$.

Proof. If the conditions in (ii) are satisfied, we have

$$-(d_0 + d_3 - d_2 e_1) e_2 \leq -\min(\delta_+, \delta_-) e_2^2$$

Also applying condition (i), we have $\dot{V}_2 \leq -(d_1 + \min(\delta_+, \delta_-)) e_2^2 \leq -\alpha_2 e_2^2$, $\dot{V}_2 = 0$ only and only if $e_2 = 0$. Since $V_2 = \frac{1}{2} e_2^2$, then $\dot{V}_2 \leq -2\alpha_2 V_2$, which means the exponentially stability of e_2 with a convergent rate faster than $e_2^{-2\alpha_2 t}$. □

If the designed controller u_1 and u_2 satisfy all the sufficient conditions in Theorem 6.1 and 6.2, the Lyapunov function of the entire system defined as $V(e) = V_1(e) + V_2(e)$ satisfies the following inequality,

$$\dot{V} \leq -(\alpha_1 e_1^2 + \alpha_2 e_2^2) \leq -2\min(\alpha_1, \alpha_2) V,$$

therefore the entire error system is stable.

Developing algorithms for controller parameters k_i and l_i is challenging since the terms in the sufficient conditions are nonlinear functions of these parameters. To obtain k_i and l_i from these conditions may require some search algorithm by iterations. From practical point of view, we would prefer to partially decouple the parameters first and then develop some explicit expressions from the sufficient

conditions. Relations between k_i and c_i, and between l_i and d_i are first studied. By fixing k_2, the other three parameters k_3, k_0, and k_1 can be solved sequentially. Similarly solving l_3 first, l_1 and l_2 can be solved sequentially. Next, some extra constraints are introduced to decouple c_i and d_i in the sufficient conditions of Theorems 6.1 and 6.2. Different δ_+, δ_- values may be required for the transformation.

For the subsystem of e_1, the following procedures are applied on the sufficient conditions in Theorem 6.1.

- If $e_1 \geq 0$, first we set $c_2 = 0$ to remove the effect from reference $\dot{r}_1$, this constraint can be removed in local stabilization when $\dot{r}_1 = 0$. By choosing $\delta_+ = 0$, the condition $c_0 + c_3 - c_2\dot{r}_1 - \delta_+ e_1 \geq 0$ can be relaxed to $c_0 + c_3 \geq 0$. Since $c_0 \geq 0$, we use the constraint $c_3 \geq 0$ here to develop the expression of k_i. The boundary conditions of k_3 can be solved at the equality condition. k_0, k_1 can be solved sequentially.

- If $e_1 < 0$, the appearance of c_i in those conditions is difficult to decouple. We need to assign k_0 and k_1 values first to calculate c_0, then choose a positive value for c_{20} and assign the initial value of c_2 as $\text{sign}(\dot{r}_1)c_{20}$. If $\dot{r}_1 = 0$, we set $c_2 = 0$. Therefore the sufficient condition can as formulated as

$$c_3 \leq c_{20}\dot{r}_1 - c_0 - \delta_-|e_1|, \quad e_1 < 0 \tag{6.2}$$

  By choosing very small δ_-, we can neglect the $\delta_-|e_1|$ term and the constraint in Eqn. (6.2) can be further relaxed to $c_3 \leq c_{20}\dot{r}_1 - c_0$. The range of k_3 can be found through this new inequality. Using a feasible k_3 value, k_0 and k_1 can be solved. At last, we need to verify the constraint in Eqn. (6.2) with the new c_0 updated with the new k_0 and k_1 values.

Similar procedures are applied to the sufficient conditions in Theorem 6.2. In this case, e_1 replaced $\dot{r}_1$ in the inequality condition. We also studied the conditions according to the sign of e_2 separately.

- If $e_2 \geq 0$, first we set $d_2 = 0$ to remove the effect from e_1, this condition can be relaxed in local stabilization when $e_1 \approx 0$. By choosing $\delta_+ = 0$, the

condition $d_0 + d_3 - d_2 e_1 - \delta_+ e_2 \geq 0$ can be relaxed to $d_0 + d_3 \geq 0$. Since $d_0 \geq 0$, we use the constraint $d_3 \geq 0$ to obtain the expression of l_i. The boundary conditions of l_3 can be solved at the equality condition. l_1 and l_2 can be solved sequentially.

- If $e_2 < 0$, the appearance of d_i in those conditions is difficult to decouple. We have to assign l_1 and l_2 values first to calculate d_0, then choose a positive value d_{20} and assign the initial value of d_2 as sign$(e_1)d_{20}$. Thereafter, we can reformulate the condition as

$$d_3 \leq d_{20} e_1 - d_0 - \delta_- |e_2|, \quad e_2 < 0 \tag{6.3}$$

  By choosing very small δ_-, we can neglect the $\delta_- |e_2|$ term, and replace the constraint in Eqn. (6.3) with $d_3 \leq d_{20} e_1 - d_0$. The range of l_3 can be found by the new inequality. Choosing a feasible l_3 value, l_1 can be solved by $d_2 =$ sign$(e_1)d_{20}$ and l_2 can be solved by $d_1 \geq \alpha_2$ sequentially. At last, we will need to verify the constraint in Eqn. (6.3) with the new d_0 updated with the new l_1 and l_2 values.

The corresponding algorithm is derived based on the simplifications of sufficient conditions illustrated above.

Algorithm : Pseudo PID/State feedback controller

1. Calculate parameters $z_{i,\ i=1,\cdots,3}$

$$z_1 = q_2 - \frac{q_3^2}{4q_4}$$

$$z_2 = q_1 r_1 + q_5 r_1 - q_5 T_a - q_1 r_2 + q_2 r_1^2 - q_2 r_2^2 + (q_1 + 2 z_1 r_2) e_2 - z_1^2 e_2^2 - q_2 e_1^2$$

$$z_3 = q_1 + q_5 + 2 q_2 r_1$$

   and $k_2 = \frac{q_3}{2q_4}$.

2. If $e_1 \geq 0$, search for a solution of F_1 that satisfies $F_1^2 \geq (q_3 r_2)^2 + 4 q_4 z_2$. Calculate $k_3 = (F_1 - q_3 r_2)/(2q_4)$ and $k_0 = 1/F_1$.
   Choose $\alpha_1 > 0$ and solve for k_1 satisfying

$$(F_1 + 2 q_4 \dot{r}_1 / F_1) k_1 > \alpha_1 - z_3$$

3. If $e_1 < 0$ and we have k_i available from last iteration, we calculate c_0 using these k_i values as $c_0 = q_4 k_1^2 e_1^2 + q_4 k_0^2 \dot{r}_1^2$ and verify the constraints

$$F_1^2 \leq (q_3 r_2)^2 + 4q_4(z_2 + c_2\dot{r}_1 - c_0)$$

$$c_1 = z_3 + F_1 k_1 + 2q_4 \dot{r}_1 k_0 k_1 \geq \alpha_1$$

If these two constraints are satisfied, we use the same k_i from last iteration and continue to step 4.

Else, we choose some positive constant C_{20}, and set initial c_{20} =sign$(\dot{r}_1)C_{20}$, assign some initial k_0 and k_1 to calculate $c_0 = q_4 k_1^2 e_1^2 + q_4 k_0^2 \dot{r}_1^2$, and solve the inequality

$$F_1^2 \leq (q_3 r_2)^2 + 4q_4(z_2 + c_{20}\dot{r}_1 - c_0)$$

Calculate $k_3 = (F_1 - q_3 r_2)/(2q_4)$ and $k_0 = (1 - c_{20})/F_1$.

Choose $\alpha_1 > 0$ and solve for k_1 satisfying

$$(F_1 + 2q_4\dot{r}_1(1 - c_{20})/F_1)k_1 > \alpha_1 - z_3$$

Next, we need to calculate the new c_0 with k_0 and k_1. If the new c_0 is smaller than the old c_0, the search for k_i ends. Otherwise, use these new k_0 and k_1 values to search for new k_3 and repeat the process.

4. Fill in the value of k_i into the following controller structure and get the control value

$$u_1 = k_0\dot{r}_1 + k_1 e_1 + k_2 e_2 + k_3$$

and apply the constraints on u_1.

$$\tilde{u}_1 = \begin{cases} \min(u_1, u_{1max}), & u_1 \geq 0 \\ \max(u_1, u_{1min}), & u_1 < 0 \end{cases}$$

5. Calculate parameters $z_{i,\ i=4,\cdots,6}$

$$\begin{aligned} z_4 &= q_6 + q_{10} + q_{11} + 2q_7 r_2 + 2q_{12} r_2 \\ z_5 &= q_{11} + 2q_{12} r_1 \\ z_6 &= q_6 r_2 - q_6 d + q_7 r_2^2 - q_7 d^2 - q_{11} r_1 + q_{11} r_2 - q_{12} r_1^2 + q_{12} r_2^2 \\ &\quad + q_{10} r_2 - q_{10} T_a + q_{13} r_1 \tilde{u}_1 + q_{14} \tilde{u}_1^2 + (q_7 + q_{12}) e_2^2 \end{aligned}$$

6. If $e_2 > 0$, search for a solution of F_2 that satisfies

$$F_2^2 \geq (q_8 d)^2 + 4 q_9 z_6$$

Calculate $l_3 = (F_2 - q_8 d)/(2q_9)$ and $l_1 = z_5/F_2$

Choose $\alpha_2 > 0$ and find a solution l_2 that satisfies

$$F_2 l_2 \geq \alpha_2 - z_4$$

7. If $e_2 < 0$ and we have l_i available from last iteration, we calculate $d_0 = q_9(l_2 e_2 + l_1 e_1)^2 + q_{12} e_1^2$, and verify the constraints

$$F_2^2 \leq (q_8 d)^2 + 4 q_9 (z_6 + d_2 e_1 - d_0)$$

$$d_1 = z_4 + F_2 l_2 \geq \alpha_2$$

If these two constraints are satisfied, the same k_is are used and continue to step 8.

Else, choose some initial $D_{20} > 0$, and assign d_{20} =sign$(e_1) D_{20}$, and assign some l_1 and l_2 to calculate d_0, next solve the inequality

$$F_2^2 \leq (q_8 d)^2 + 4 q_9 (z_6 + d_{20} e_1 - d_0)$$

If the solution of the above inequality is found, we choose the positive solution and calculate $l_3 = (F_2 - q_8 d)/(2q_9)$ and $l_1 = (z_5 - d_{20})/F_2$.

For some $\alpha_2 > 0$, and find a l_2 satisfies:

$$F_2 l_2 \geq \alpha_2 - z_4$$

Fill in the new l_1 and l_2 values to obtain d_0, if the new d_0 is no larger than the old d_0, then the conditions of the theorem are all satisfied. Otherwise, use the new d_0 as the initial value and search for a new l_3 and l_1, l_2 sequentially, until the conditions are satisfied.

8. Calculate $u_2 = l_1 e_1 + l_2 e_2 + l_3$ and apply constraints on u_2

$$\tilde{u}_2 = \begin{cases} \min(u_2, u_{2max}), & u_2 \geq 0 \\ \max(u_2, u_{2min}), & u_2 < 0 \end{cases}$$

Remark 6.1. *In the algorithm, six new variables* $z_i,\ i = 1, \cdots, 6$ *and two new functions* $F_1(k_3) = q_3 r_2 + 2q_4 k_3$, $F_2(l_3) = q_8 d + 2q_9 l_3$ *are introduced to simplify the formulation of conditions. The coefficients* c_i *and* d_i *in Theorem 6.1 and 6.2 can be expressed as follows:*

$$\begin{aligned} c_1 &= z_3 + F_1 k_1 + 2q_4 \dot{r}_1 k_0 k_1 \\ c_2 &= 1 - F_1 k_0 \\ c_3 &= \frac{F_1^2 - 4q_4 z_2 - q_3^2 r_2^2}{4q_4} \\ d_1 &= z_4 + F_2 l_2 \\ d_2 &= z_5 - F_2 l_1 \\ d_3 &= \frac{F_2^2 - 4q_9 z_6 - q_8^2 d^2}{4q_9} \end{aligned}$$

By direct comparison, these inequalities used in the algorithm can find their counterparts in the sufficient conditions of the two theorems.

Remark 6.2. *Similar to the feedback linearization-based design, the existence condition of a solution depends on both the error dynamics and the sign of the error, which can not be determined* a priori. *In addition, due to the additional constraints, the algorithm is more conservative. For the specific system, we are confident that the system can be stabilized in normal operating conditions. In the proposed algorithm, when* $e_i > 0$ *the system dynamics provides relatively large range for the parameters and further simplifications can be applied to develop a quick search algorithm. When* $e_i < 0$*, there is no explicit expression for the parameters. If the system is operated in close vicinity of the equivalent point, the same parameters for* $e_i > 0$ *usually can still satisfy the conditions due to the robustness of the system. When* e_i *is a large negative number, those simplified conditions are not valid, and we have to return to the original conditions to search for a solution. In that case, a few iterations may be required. Similar to the feedback linearization-based design, we would either reduce* α_i *value or use the previous feasible solution.*

Remark 6.3. *Due to the appearances of* e_1 *and* e_2 *in* z_2 *and* z_6 *respectively, the parameter* k_i *and* l_i *are directly related to the process errors. Therefore, the pseudo-PID controller has state-dependent parameters. One exception is* k_2*, which is cal-*

culated as $k_2 = q_3/(2q_4)$ and is only indirectly affected by e_i through q_3 and q_4. In local range q_3 and q_4 are almost constant, constant k_2 could be used for further simplification.

Since the controller parameters are updated by the algorithm online, changes of model parameters and operating conditions are reflected automatically, which could facilitate smooth transition and fast stabilization. Nonlinear characteristics and coupling effects between subsystems are also included in the design implicitly. However, some limitations exist in this pseudo-PID/ cross state feedback controller. The search algorithm uses inequality conditions and may need several iterations when $e_i < 0$, which may cause a relatively longer calculation time. In practice, we may need to restrict the errors into a small range through the reference design and parameter tuning to avoid the infeasible cases. If the system dynamics provides a large enough parameter range to guarantee the stability, we may consider using a time-invariant PID type controller locally to avoid the iterations in the parameter search, which is further considered under a switching strategy.

6.2 Switching strategy

Using the parameter algorithm for the nonlinear pseudo-PID/cross state feedback controller, a linear PID/cross feedback controller can be derived in the local range easily by fixing the parameter values. The main difference is that the varying bias term in the nonlinear controller is replaced by an integral control with non-zero initial integral value. The introduction of integral control ideally can eliminate steady state errors. The derivative term $k_0\dot{r}_1$ is removed from u_1 since we set $\dot{r}_1 = 0$ at the local ranges. Therefore, the local controller has the following structure,

$$u_1 = k_1 e_1 + k_2 e_2 + k_{30} + k_i \int e_1 dt \tag{6.4a}$$

$$u_2 = l_1 e_1 + l_2 e_2 + l_{30} + l_i \int e_2 dt \tag{6.4b}$$

where k_{30} and l_{30} are two constants used as the initial integral values, k_i and l_i are newly introduced integral gains. Since the new controller is only used for local stabilization in a very tight range, small k_i and l_i values can be used.

A typical PCR cycle is partitioned into six stages based on pre-determined switching times (Fig. 3.1) and can be repeated according to the PCR test requirement. “Transition 0” appears only once in the initial heating from 60 to 94°C before the first cycle. Each cycle starts with the first local region at 94°C, and all three local regions are followed by three transition regions. According to the partition of a PCR reference, a switching strategy can be formulated where nonlinear pseudo-PID/cross feedback controllers are applied during transitions and time-invariant PI/cross feedback controllers are applied in local stabilization. The nonlinear controller can account for the coupling between subsystems and nonlinear creeping, therefore improving tracking performance during transitions, while the local PI controller can minimize steady-state errors. Therefore the combination of these two will have the additional advantage over a single non-switching controller.

Compared to a conventional linear model-based design, the nonlinear switching controller can reflect the nonlinear creeping and coupling effects in the parameters automatically by online calculation, therefore it can avoid those off-line efforts to pre-determine look-up tables and parameter values in linear model-based switching designs. In addition, the switching from transition controller to local linear controller is time-based instead of state-based in our earlier linear switching controller [35]. Each switch move is smooth and chattering around the critical state value in the state-based switching controller can be avoided without any additional effort.

On the other hand, since the PI parameters are tuned according to the state values at the switching time instead of the local steady-state values, the parameter values of the local PI controller depend on the model parameters and the errors at the switching time, which is not best-tuned to the local model parameters. The effectiveness of the closed-loop performance will rely on the sensitivity of parameter deviations. In general, with bounded small error magnitude, parameters are always inside the stability margin. In extreme cases such as sensor failures or large signal distortions, irregular error values may lead to extreme parameter values and may cause unexpected results. Backup PID parameters may be stored to deal with this issue.

6.3 Simulation results and robustness analysis

6.3.1 Simulation results

The non-switching pseudo-PID/cross state feedback controller and the switching controller are both simulated in Simulink® 7.0. The closed-loop response using the non-switching pseudo-PID type controller as in Eqn. (6.1a) and (6.1b) is shown in Fig. 6.1. The performance is similar to the result of the feedback linearization-based controller, in which steady-state errors are found in x_2.

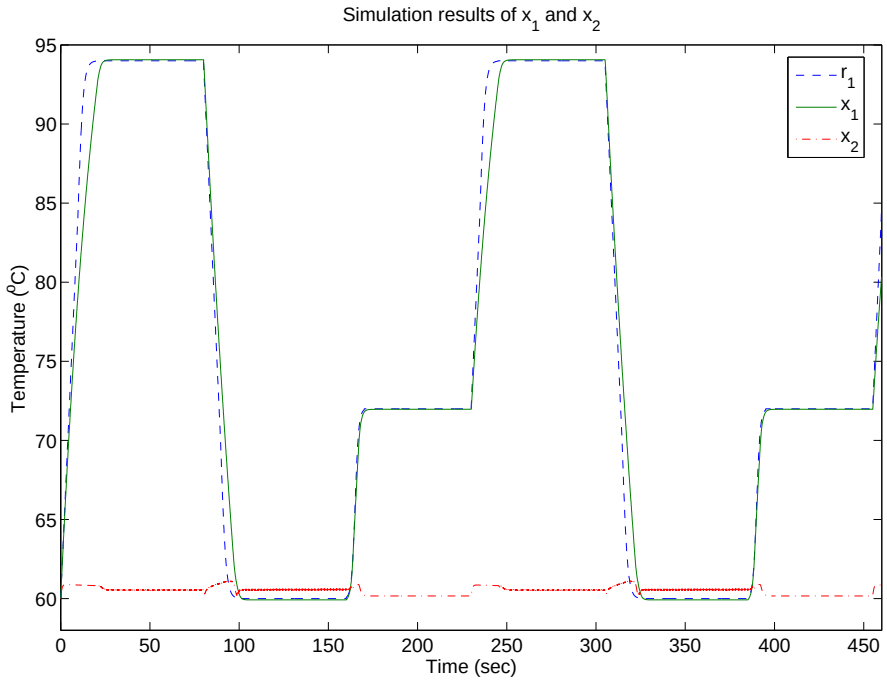

Figure 6.1: Simulated closed-loop responses of the two-stage Peltier device using a non-switching pseudo-PID/ cross feedback controller: (dashed) new reference signal, (solid) top Peltier temperature x_1, (dash-dotted) bottom Peltier temperature x_2.

Simulation of the switching pseudo-PID type controller with local time-invariant controller as in Eqn. (6.4a) and (6.4a) is further performed. The two integral gains k_i and l_i are set to 0.1 (before the voltage to DAC conversion), while the other parameters of local controller are calculated at the end of transition using the parameter algorithm of the nonlinear controller. The simulated result is shown in Fig. 6.2. Steady-state errors are eliminated as expected. But an unexpected over-

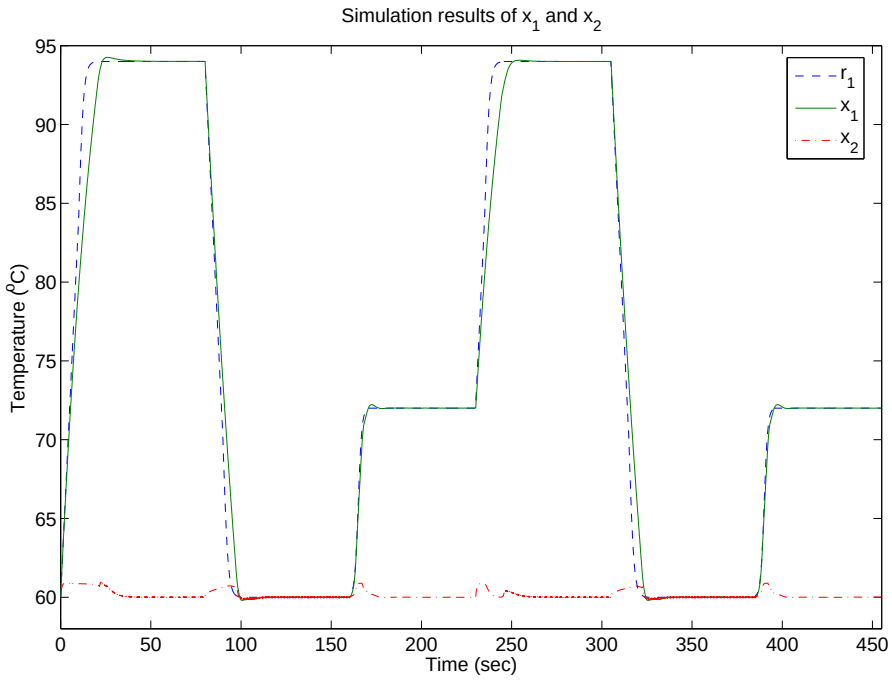

Figure 6.2: Simulated closed-loop responses of the two-stage Peltier device using a switching pseudo-PID/ cross feedback controller: (dashed) new reference signal, (solid) top Peltier temperature x_1, (dash-dotted) bottom Peltier temperature x_2.

shoot appears with the local PID controller after switching (which is due to the local PI controller). However, the magnitude of the overshoot is relatively small (about 0.3°C) which is acceptable for our PCR test. The new switching controller achieves our design objectives of eliminating steady-state errors and removing the online parameter calculations in local ranges.

6.3.2 Robustness analysis

In the previous chapter, we studied the relative parameter deviations from nominal values due to the effect of temperatures discrepancy. For $\pm$5°C deviations on temperature, the largest relative parameter deviations are only 3%. Similar to the study of the non-switching controller, we change the parameter values used in the nonlinear algorithm by different deviations levels at 3%, 6%, and 10%, and repeated closed-loop simulations. The linear controller parameters are derived using the perturbed parameters at the switching instance. As expected, closed-loop stability are

always preserved for these scenarios, and in addition, steady-state errors are minimized due to the help of the local integration action. The only difference is the magnitude of the overshoots after the transition, the largest overshoot is about 0.18 at the 10% deviation case, which is acceptable for normal PCR application.

We further studied the relative parameter deviation range of the local PI controller. Since we use the the nonlinear algorithm to derive the parameters at the switching instance, the state values are not same as the steady-state values. The effect of this difference on the local controller parameters can be viewed as model/ parameter discrepancy. During the simulation, the worse case error is with $\pm$5°C, and the errors at the switching time are about 2-3°C. For this particular two-stage Peltier modules, 2-3°C deviation on states will cause parameter deviations are much less than 3%. Assuming the worse case scenario which has the 3% parameter deviations due the modeling errors superimposed on less than 3% deviations due to the mismatch between states at the switching time and the steady-state, the overall deviations will be still much less than 10%, therefore the closed-loop stability will be preserved.

6.4 Experimental results

The switching controller is also coded into the PIC micro-controller. The sampling interval is also 100ms. Fig. 6.3 shows the measured temperatures of the two Peltiers and the heat sink, which verified the expected performance from the simulation. The corresponding control inputs are shown in Fig. 6.4. The temperature outputs of the top Peltier around the three set-points are shown in Fig. 6.5(a)-(c) respectively, while the temperature output of the bottom Peltier is shown in the zoomed-in range in Fig. 6.5(d).

Smooth transitions are observed where largest overshoots (about 0.6°C) are found at 94 region on x_1. Subsequent oscillations after the first overshoot are eliminated, therefore x_1 settles to steady-state quickly. Using the parameters set in simulations, the initial overshoot of x_1 at the 60°C region is relatively larger, we further delay the switching time by 2 seconds. No overshoot is found in x_1 in the

60°C region with the new switching time. Also, a reduced variation range of both the transitions and the local regions are observed in measured x_2.

Compared to our earlier decentralized switching controller design in Chapter 3, we find that the two nonlinear model-based controller designs share a few advantages:

- Smoother transitions and smaller overshoots of x_1 are achieved using the nonlinear model-based controllers. By applying a carefully designed smooth reference signal, the magnitudes of the errors in the transitions are much smaller, which help improve the transition response. The overshoot of x_1 after transition to 94°C is reduced from 0.8°C to 0.6°C, and a larger reduction of overshoot is achieved in 60°C region (reduced to 0.2°C).

- Subsequent oscillations after the overshoot observed in linear switching design are eliminated using the nonlinear designs, which lead to the reduction of the settling time. Although the rise time is 2-3 seconds slower than the linear switching controller, the settling time is reduced by about 8-10 seconds. Here, a smaller error bound ($\pm$0.5°C) is used to determine the settling time.

- The MIMO controller includes the cross feedback terms which reflects the coupling effects between the two Peltiers. Therefore, smaller errors of x_2 are achieved during transition with the help of coupling terms from e_1. The maximum magnitudes of the errors e_2 are reduced from 4°C to 2°C. The minimum u_2 values from the two nonlinear designs at most time are away from the lower bound. Extreme cooling only happens in very short time span. While in earlier linear design, we intentionally to use minimum value for a very long time due to lack of transition model information.

Compared to the extended feedback linearization-based design, the main advantage of the switching pseudo-PID controller is the reduced calculation burden at local range using fixed controller parameters. Although there are some steady-state errors observed using the extended feedback linearization-based controller, the errors due to model/controller mismatch could be reduced by including a local high

gain controller on top of the nonlinear controller. While with the switching pseudo-PID controller, steady-state errors are minimized due to the integration action.

Another difference is observed on the magnitude of u_2 (as the input to a 12-bit D/A converter, the range is [0, 4095]). In the extreme cooling transition, the minimum DAC value is about 1000 in the switching pseudo-PID controller, while in the extended feedback linearization case the minimum DAC is about 100. The main reason of the difference is that the sign choice of u_2, and when in the first controller, we choose the negative square root, and while in the pseudo-PID design, the negative square root is out of boundary and only the positive root can be used. However, since the trough of u_2 during transition appears in a very short time span, the effect of the different minimum u_2 values on x_2 is not discernable.

Furthermore, we use local integration element to deal with bias term in this design while in extended feedback linearization design we choose a local proportional gain element instead of an integration part. The main reason of choosing two different bias adjusting methods here is the difference on the switching time and the necessity to set initial integration value. For the first design, we intended to avoid switching during transitions (more convenient for the controller to be scaled up). So at the time when local bias adjusting part is applied, the errors are relatively small (less than 0.5°C), and a large gain could minimize the error much quickly compared to slower integration process. If the high gain controller is applied earlier during switching, extreme control value will be generated which essentially cause the control signal saturated at the hardware limitation. And extreme control signals at the end of the transition usually will cause larger overshoot which is undesired. For the second design, the choice of integration control is straightforward as the local controller already has the proportional control elements and the inclusion of the integral control is necessary to improve the robustness of the linear controller.

6.5 Summary

In this chapter, we proposed a switching nonlinear controller which has a structure similar to PID controller but with extra cross state feedback term. With this simple

structure, designing the local fixed-parameter controller is simple and straightforward from the nonlinear counterpart. Both simulation and experimental results verified that improvement on the transition performance and the minimizations of steady-state errors.

However, the improvement in performance is associated with the complexity in the algorithm. As a general Lyapunov function-based design, the controller algorithm is specific to the exact system model, and the existence of solutions depends on the system parameter values. The extension to higher order system will be more difficult. For our custom-made two-stage Peltier-based thermal device for microfluidic-based PCR cycling, this nonlinear switching pseudo-PID type controller achieves the desired closed-loop performance in the sense of fast and smooth transition and small steady-state errors and avoid the intensive tuning efforts associated with the linear model-based designs.

Due to the similarity to conventional PID controller, this nonlinear controller design includes the earlier linear switching PID controller design and other variants as special cases and could be used as the basis for other switching controller designs. Although the parameters are usually different as the nonlinear design is based on the models at the switching time while linear designs are based on steady-state. The nonlinear algorithm could still be used to calculate the initial values for switching parameters setting to replace the look-up tables. Also further model simplifications can be introduced such as a design with partially bang-bang action before switching for u_1 and nonlinear algorithm for u_2 (bang-bang control is a control strategy for fast transition with control input values set at either the maximum or the minimum, which is not suitable for u_2 as r_2 is constant). Here, such designs with different simplifications are not further discussed as they are more specific to the reference and operating conditions and require more tunings and if-else conditions, which contradicts with our intention to have controllers with less tuning burden and to be easily applicable with different references without further modeling efforts.

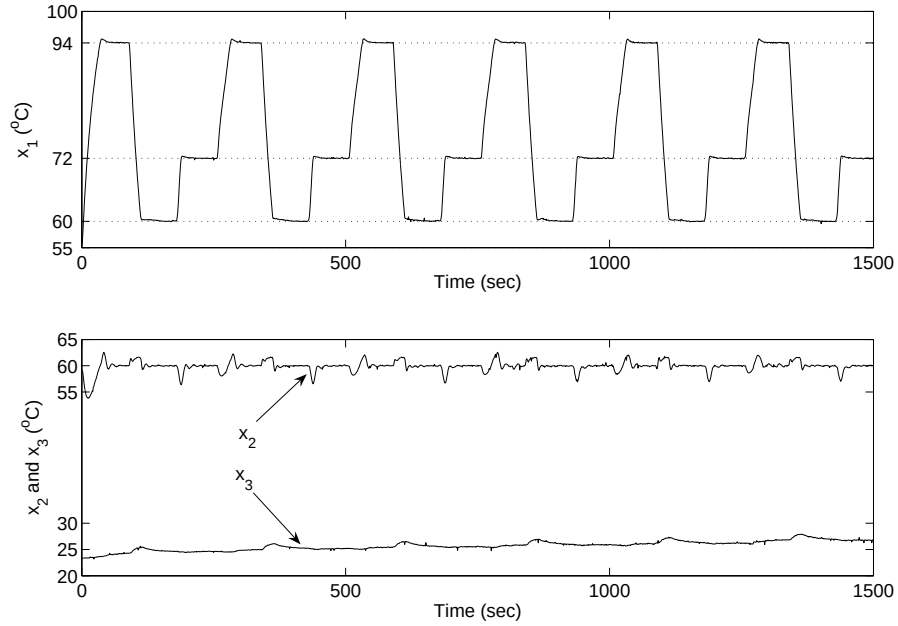

Figure 6.3: Measured outputs using a switching pseudo-PID/ cross feedback controller for six PCR cycles: (top graph) temperature of the top Peltier x_1, (bottom graph) temperatures of bottom Peltier x_2 and heat sink x_3.

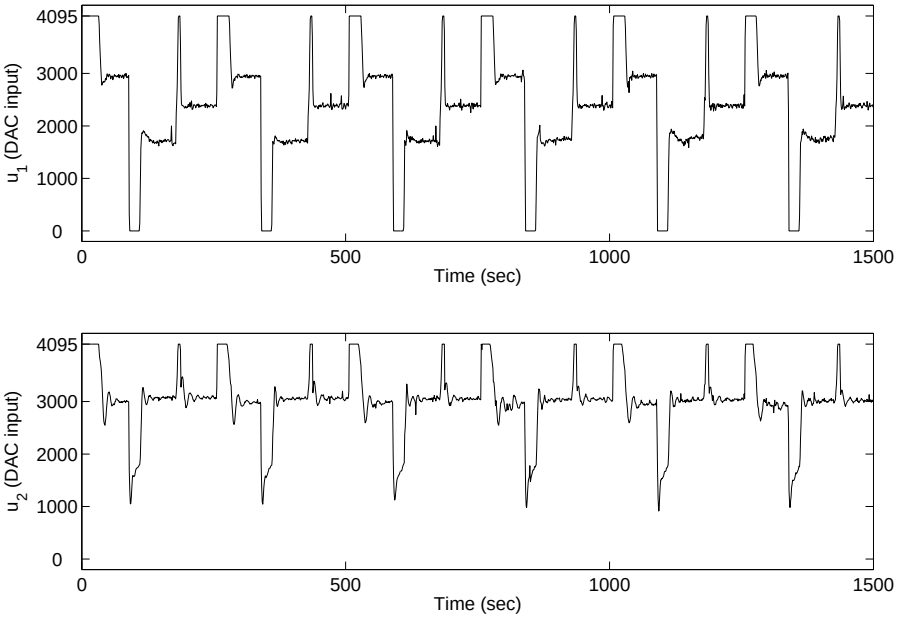

Figure 6.4: Digital control inputs using a switching pseudo-PID/ cross feedback controller for six PCR cycles: (top graph) 12-bit DAC input for top Peltier u_1, (bottom graph) 12-bit DAC input for bottom Peltier u_2.

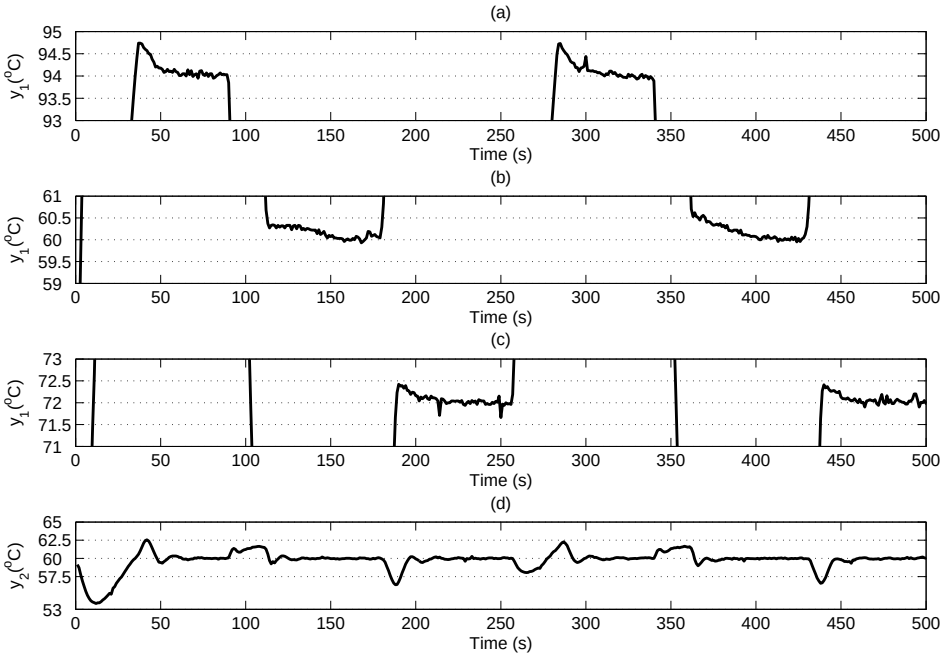

Figure 6.5: Measured outputs at local regions for two representative PCR cycles using a switching pseudo-PID controller. (a) x_1 around the 94°C region; (b) x_1 around the 60°C region; (c) x_1 around the 72°C region; (d) x_2 around the 60°C region;

Chapter 7

Conclusions

Using microfluidic-based platform to perform traditional bio-molecular tests for disease diagnosis has been widely studied and applied in various laboratories. Portable diagnostic test-kits will lead the new revolution in medical device development. From an instrument point of view, a high efficiency thermal cycler with fast response rate, precise tracking performance and low cost is one of the key factors of successful tests. Various heating materials and configurations are developed for microfluidic-based reactions, the Peltier module as a traditional external contact-mode thermal device has some advantages in microfluidic applications. Low cost and external heating could help to make disposable microchips, while combined heating/cooling ability could reduce the cooling time. Furthermore, multiple-stage Peltier modules with multiple control inputs are studied here to improve the thermal efficiency of each Peltier module and achieve reduced transition time with MIMO controller designs. In this thesis, we focused on the controller designs of multi-stage Peltier-based thermal device for a microfluidic platform developed in the AML at the University of Alberta. Although the controllers are developed for one typical PCR cycling requirement, the modeling methods and design methodology can be extended to other bio-molecular applications and different Peltier-based devices.

In Part I of the thesis, linear system identification based controller design is proposed and implemented. A decentralized switching PID controller is tuned in both simulations and experiments, and is validated by a PCR-CE test of patients' urine sample for BK virus detection. Successful DNA amplification results are achieved using our Peltier device with this switching controller. We deal with this

highly nonlinear system with a multi-model approximation, and identify three intermediate local linear models to approximate the system in local regions. Internal model-based PID controllers provide desired local stabilization performance while transition performance is improved by carefully tuned PD/PI switching strategy. This design is easy to use due to the small number of parameters. However, intensive tuning of PID parameters and the switching settings are required to achieve the balance between fast transition and small overshoot which is difficult with limited linear model information. In addition, when the reference changes, further parameter tuning usually is required and local models may need to be re-identified, which makes the extension of the controller more complicated.

In Part II of the thesis, we intended to develop nonlinear model-based controllers to better reflect the coupling and drifting effects during the transitions and to reduce or avoid parameter tuning effort associated with the linear designs. Main electrothermal effects contributing the heating/cooling functionalities of a single Peltier module are studied, and the thermodynamics of the interfacing materials are used to develop models based on energy balance equations. A simplified nonlinear MIMO state-space model with state-depended parameters is developed which can approximate the system over a large temperature range. Model structure reduction and parameter simplifications are applied through various open-loop local RBS input tests and closed-loop reference tracking test. The obtained model can track both the transition and local stabilization responses and reflect the coupling effects between two Peltier modules.

Based on this nonlinear model, two nonlinear non-switching controller designs are proposed. Special treatments are introduced here to deal with the new challenges associated with the model (both u_i and u_i^2 affect the dynamics of the state). An extension of the strict feedback form of the traditional control-affine system is introduced to the new system with both u_i and u_i^2. Since the Peltier system model is in strict feedback form, the MIMO controller design is converted to sequential SISO controller designs.

First, we applied the input-state feedback linearization method to the transformed SISO dynamics in the sequential manner. Corresponding theorem for the

closed-loop stability conditions is proved and an algorithm is developed which generates a numerical control value at each simulation/sampling step with updated system parameters. This single non-switching controller achieved fast transition and small overshoot and validated the feasibility of the nonlinear control application. Since the design methodology is applied to individual SISO system sequentially, this design can be extended to high dimension with similar parameter algorithm. The deviation levels of model parameters are studied and the worse case scenarios are simulated, and we found relatively large tolerance of uncertainty level on the closed-loop stability. Larger steady-state errors are found with larger parameter deviations, therefore, an optional local high gain controller is proposed to reduce the steady-state errors. Unlike the local model based PID design which relies on the identification results at specific operating points, this nonlinear controller can be applied to different tracking profile without model identification steps and controller parameter re-design as the model parameters are updated online inside the controller algorithm. This later property will facilitate the extension of this Peltier-based device to other tests beyond PCRs.

However, the necessity of the implementation of the entire nonlinear algorithm and the internal parameter updating of the feedback linearization-based design will be redundant at local regions when the system is close to equivalent points. Relatively large stability margin to tolerate parameter uncertainties are observed in closed-loop simulation, therefore using local fixed parameter controller to replace the nonlinear control is feasible. A local PI controller is considered where the integral action is included to minimize the steady-state error. A pseudo-PID type controller is proposed based the nonlinear model, whose parameters are derived using the Lyapunov function method. A simplified algorithm is developed and the stability conditions are proposed for the algorithm. A new time-based switching strategy is introduced to utilize the parameters of the nonlinear pseudo-PID controller for the initial values of the local PI controller, and to achieve smooth transitions. Simulation and experimental results validated the feasibility of the new proposed switching nonlinear pseudo-PID type controller. Steady-state errors are minimized as expected while the transition rate is almost similar to the non-switching case. The

overshoots are a little bit larger but the magnitude is inside the acceptable range.

In this thesis, three different controllers are developed for the custom-made two-stage Peltier-based thermal device for medical applications. Although the linear model identification based design can achieve the PCR cycling requirement with careful tuning, the local models and controllers are based on specific operating points and the closed-loop performance will deteriorate when the operating conditions change. The two nonlinear-model based designs utilize the first principle-based models and could work over larger ranges. Smooth transitions with reduced overshoot and settling time and minimized steady-state error are achieved using these two controllers. The first non-switching design is based on an extension of a general input-to-state feedback linearization technique which can be applied to a class of systems not only affine on the control but also affine on the square of control inputs, including many electromagnetic systems. Also the design can be easily extended to higher order systems. Adding an optional local bias tracking adjustment, performance deterioration due to the model parameter uncertainty can be minimized. The second nonlinear switching design provides the option to reduce online calculation burden and could include linear switching PID design as a special case. However, the fixed controller structure requires a more complicated parameter algorithm and the design is not easily scalable to higher order systems. Depending on the performance requirements and other implementation considerations, all three controllers can be chosen for microfluidic-based thermal applications. With fewer parameters to set and an internal parameter updating mechanism, the applications of the Peltier-based device with nonlinear controllers are easier for non-control end-users and the device is readily for other various thermal settings in microfluidic-based reactions.

Further improvement of the experimental device with user friendly graphic user interfaces (GUIs) and user triggered online parameter tuning functionality are expected to be implemented to facilitate the commercialization of the device for portable disease diagnostic applications.

Bibliography

[1] K. J. Aström and H. Hagglund. *PID Controllers: theory, design, and tuning*. Instrument Society of America, Research Triangle Park, N.C., 2nd edition, 1995.

[2] C. J. Backhouse, M. Carrmano, F. Oaks, E. Nordman, A. Carrillo, B. Johnson, and S. Bay. DNA sequencing in a monolithic microchannel device. *Electrophoresis*, 21:150–156, 2000.

[3] C. J. Backhouse, T. Footz, S. Adamia, and L. M. Pilarski. Microfluidic chips for the molecular analysis of human cancer. In *Proc. IEEE International Conference on MEMS, NANO and Smart Systems(ICMENS'03)*, pages 377 – 382, Banff, AB, Canada, Jul 2003.

[4] P. Belgrader, S. Young, B. Yuan, M. Primeau, L. A. Christel, F. Pourahmadi, and M. A. Northrup. A battery-powered notebook thermal cycler for rapid multiplex real-time PCR analysis. *Analy. Chem.*, 73:286–289, 2001.

[5] A. Boukhris, G. Mourot, and J. Ragot. Non-linear dynamic system identification: a multi-model approach. *Int. J. Control*, 72:591–604, 1999.

[6] Catalog. Applied Biosystems, Veriti Thermal Cycler [online]. Available: http://www.appliedbiosystems.com/, 2010.

[7] Catalog. Bellingham + Stanley, Refractometers [online]. Available: http://www.bellinghamandstanley.com/ltd/refractometers.html, 2010.

[8] Catalog. Bio-rad, c1000 Thermal Cycler [online]. Available: http://www.bio-rad.com/, 2010.

[9] Catalog. Deben (UK), COOLSTAGE SEM heating & cooling stages [online]. Available: http://www.deben.co.uk/, 2010.

[10] Catalog. Eppendorf mastercycler thermal cycler [online]. Available: http://www.eppendorf.com/, 2010.

[11] Catalog. Ferrotec (USA) corp. [online]. Available: http://www.ferrotec.com/technology/thermoelectric/, 2010.

[12] Catalog. Maxim Integrated products Inc. [online]. Available: http://datasheets.maxim-ic.com/en/ds/MAX1978-MAX1979.pdf, 2010.

[13] J. A. Chávez, J. A. Ortega, J. Salazar, A. Turó, and M. J. García. SPICE model of thermoelectric elements includeing thermal effects. In *Proc. 17th IEEE Instrumentation Measurement Technology Conference (IMTC2000)*, pages 1019–1023, Baltimore, M.D., May 2000.

[14] FerroTec (USA) Corp. Thermoelectric technical reference guide [online]. Available: http://www.ferrotec.com/technology/thermoelectric/thermalRef01/, 2010.

[15] H. J. Crabtree, E. C. S. Cheong, D. A Tilroe, and C. J. Backhouse. Microchip injection and separation anomalies due to pressure effects. *Anal. Chem.*, 73:4079–4086, 2001.

[16] F. Felici, J. van Wingerden, and M. Verhaegen. Subspace identification of MIMO LPV systems using a periodic scheduling sequence. *Automatica*, 43:1684–1697, 2007.

[17] T. Footz, M. J. Somerville, R. Tomaszewski, B. Elyasb, and C. J. Backhouse. Integration of combined heteroduplex/restriction fragment length polymorphism analysis on an electrophoresis microchip for the detection of hereditary haemochromatosis. *Analyst*, 129:25–31, 2004.

[18] R. A. Freeman and P. V. Kokotović. *Robust Nonlinear Control Design: State-Space and Lyapunov Techniques*. Birkhäuser, Boston, M.A., 1996.

[19] N. Futai, W. Gu, and S. Takayama. Rapid prototyping of microstructures with bell-shaped cross-sections and its application to deformation-based microfluidic valvess. *Adv. Mater.*, 16:1320–1323, 2004.

[20] C. E. Garcia and M. Morari. Internal model control. 1. a unifying review and some new results. *Ind. Eng. Chem. Process Des. Dev.*, 21:308–323, 1982.

[21] C. E. Garcia and M. Morari. Internal model control. 2. design procedure for multivariable systems. *Ind. Eng. Chem. Process Des. Dev.*, 24:472–484, 1985.

[22] P. Gascoyne, J. Satayavivad, and M. Ruchirawat. Microfluidic approaches to malaria detection. *J. Micromech. Microeng.*, 89:357–369, 2005.

[23] B. C. Giordano, J. Ferrance, S. Swedberf, A. F. R Huhmer, and J. P. Landers. Polymerase chain reaction in polymeric microchips: DNA amplification in less than 240 seconds. *Anal. Biochem.*, 291:124–132, 2001.

[24] K. R. Godfrey, A. H. Tan, H. A. Baker, and B. Chong. A survey of readily accessible perturbation signals for system identification in the frequency domain. *Control Eng. Pract.*, 13:1391 – 1402, 2005.

[25] N. Goedecke, B. McKenna, S. El-Difrawy, L. Carey, P. Matsudaria, and D. Ehrlich. A high-performance multilane microdevice system designed for the dna forensic laboratory. *Electrophoresis*, 25:1678–1686, 2004.

[26] T. L. Hawkins, J. Detter, and P. M. Richardson. Whole genome amplification - applications and advances. *Current Options in Biotechnology*, 75:65–67, 2002.

[27] V. N. Hoang. Thermal management strategies for microfluidic devices. Master's thesis, Electrical and Computer Engineering, University of Alberta, 2008.

[28] J. W. Hong, T. Fujii, M. Seki, T. Yamamoto, and I. Endo. Integration of gene amplification and capillary gel electrophoresis on a polydimethylsiloxane-glass hybrid microchip. *Electrophoresis*, 22:328–333, 2001.

[29] D. S. Hwang and P. L. Hsu. A practical design for a multivariable proportional-integral controller in industrial applications. *Ind. Eng. Chem. Res.*, 36(7):2739–2748, 1997.

[30] M. Imran and A. Bhattacharyya. Thermal response of an on-chip assembly of RTD heaters, sputtered sample and microthermocouples. *Sensors and Actuators A*, 121:306–320, 2005.

[31] J. Jiang, G. V. Kaigala, H. J. Marquez, and C. J. Backhouse. Nonlinear controller designs for thermal management in PCR amplification. Submitted to IEEE Trans. Control Syst. Technol., 2010.

[32] G. V. Kaigala, V. N. Hoang, and C. J. Backhouse. Electrically controlled microvalves to integrate microchip polymerase chain reaction and capillary electrophoresis. *Lab Chip*, 8:1071–1078, 2008.

[33] G. V. Kaigala, V. N. Hoang, A. Stickel, J. Lauzon, D. Manage, L. M. Pilarski, and C. J. Backhouse. An inexpensive and portable microchip-based platform for integrated RT-PCR and capillary electrophoresis. *The Anaylyst*, 133:281–404, 2008.

[34] G. V. Kaigala, R. J. Huskins, J. Preiksatis, X. L. Peng, L. M. Pilarski, and C. J. Backhouse. Automated surveillance using microfluidic chip-based PCR thermocycling and product detection to assess risk of polyoma BK virus associated neuropathyin renal transplant recipients. *Electrophoresis*, 27:3753–3763, 2006.

[35] G. V. Kaigala, J. Jiang, C. J. Backhouse, and H. J. Marquez. System design and modeling of a time-varying, nonlinear temperature controller for microfluidics. *IEEE Trans. Control Syst. Technol.*, 18:521–530, 2010.

[36] H. K. Khalil. *Nonlinear Systems*. Prentice Hall, Upper Saddle River, N.J., 3rd edition, 2002.

[37] J. Khandurina, T. E. Mcknight, S. C. Jacobson, L. C. Waters, R. S. Foote, and J. M. Ramsey. Integrated system for rapid PCR-based DNA analysis in microfluidic devices. *Anal. Chem.*, 72:2995–3000, 2000.

[38] M. U. Kopp, A. J. de Mello, and A. Manz. Chemical amplification: Continuous-flow PCR on a chip. *Science*, 280:1046–1048, 1998.

[39] M. V. Kothare, P. J. Campo, M. Morari, and C. N. Nett. A unified framework for the study of anti-windup designs. *Automatica*, 30(12):1869–1883, 1994.

[40] J. H. Lienhard IV and J. H. Lienhard V. *A Heat Transfer Textbook*. Phlogiston Press, Cambridge, M.A., 3rd edition, 2008.

[41] S. Lineykin and S. Ben-Yaakov. Modeling and analysis of thermoelectric modules. *IEEE Trans. Ind. Appl.*, 43:505–512, 2007.

[42] C. N. Liu, N. M. Toriello, and R. A. Mathies. Multichannel PCR-CE microdevice for genetic analysis. *Anal. Chem.*, 78:5474–5479, 2006.

[43] J. Liu, C. Hansen, and S. Q. Quake. Solving the ”world-to-chip” interface probelm with a microfludic matrix. *Anal. Chem.*, 75:4718–4723, 2003.

[44] L. Ljung. *System Identification - Theory For the User*. Prentice Hall, Upper Saddle River, N.J., second edition, 1999.

[45] R. G. Lyons. *Understanding digital signal processing*. Addison Wesley, Reading, M.A., 1997.

[46] H. J. Marquez. An input-output approach to systems described using multiple models. *IEEE Trans. Circuits and Systems-I: Fundamental Theory and Applications*, 47:940–943, 2000.

[47] H. J. Marquez. *Nonlinear Control Systems: Analysis and Design*. John Wiley & Sons Inc., Hoboken, N.J., 2003.

[48] M. W. McConley, B. D. Appleby, M. A. Dahleh, and E. Feron. A computationally efficient Lyapunov-based scheduling procedure for control of nonlinear systems with stability guarantees. *IEEE Trans. Autom. Control*, 45:33–49, 2000.

[49] D. Mitrani, J. A. Tomé, J. Salazar, A. Turó, M. J. García, and J. A. Chávez. Methodology for extracting thermoelectric module parameters. *IEEE Trans. Instru. Meas.*, 54:1548–1552, 2005.

[50] P. N. Ngatchou, M. R. Holl, C. H. Fisher, M. S. Saini, J. Dong, T. H. Ren, W. H. Pence, D. L. Cunningham, S. E. Moody, D. A. Donaldson, and D. R. Meldrum. A real-time PCR analyzer compatible with high-throughput automated processing of 2-μl reactions in glass capillaries. *IEEE Trans. Autom. Sci. Eng.*, 3(2):141–151, 2006.

[51] G. S. Nolas, J. Sharp, and H. J. Goldsmid. *Thermoelectrics: Basic Principles and New Materials Developments*. Spinger-Verlog, Berlin, Germany, 2001.

[52] P. J. Obeid, T. K. Christopoulos, H. J. Crabtree, and C. J. Backhouse. Microfabricated device for DNA and RNA amplification by continuous-flow polymerase chain reaction and reverse transcription-polymerase chain reaction with cycle number selection. *Anal. Chem.*, 75:288–295, 2003.

[53] R. Pal, M. Yang, B.N. Johnson, N. Shrivastava, S. X. Razzacki, K. J. Chomistek, D. C. Heldsinger, V. M. Ugaz R. M. Haque, P. K. Thwar, Z. Chen, K. Alfano, M. B. Yim, A. O. Fuller M. Krishnan, R. G. Larson, D. T. Burke, and M. A. Burns. An integrated microfluidic device for influenza and other genetic analyses. *Lab on a chip*, 5:1024–1032, 2005.

[54] P. M. Pilarski, S. Adamia, and C. J. Backhouse. An adaptable microvalving system for on-chip polymerase chain reactions. *J. Immunological Methods*, 305:48–58, 2005.

[55] A. R. Prakash. BioMEMS and nanoscience for generic analysis. Master's thesis, Electrical and Computer Engineering, University of Alberta, 2004.

[56] X. Qiu and J. Yuan. Temperature control for PCR thermocyclers based on Peltier-effect thermoelectrics. In *Proc. 27th IEEE Engineering in Medicine and Biology Annual Conference*, pages 7509 – 7512, Shanghai, P.R. China, Sept. 2005.

[57] S. B. Raffat and X. Ma. Thermoelectrics: a review of present and potential applications. *Appl. Therm. Eng.*, 23:913–935, 2003.

[58] D. E. Rivera and K. S. Jun. An integrated identification and control design methodology for multivariable process system applications. *IEEE Control Syst. Mag.*, 20(3):25–37, Jun 2000.

[59] M. G. Roper, C. J. Easley, and J. P. Landers. Advances in polymerase chain reaction on microfludic chips. *Anal. Chem.*, 77:3887–3893, 2005.

[60] D. M. Rowe. General principles and basic considerations. In *Thermoelectrics Handbook: Macro to Nano*. CRC Press, Taylor & Francis Group, Boca Raton, F.L., 2006.

[61] J. J. Shah, S. G. Sundaresan, J. Geist, D. R. Reyes, J. C. Booth, M. V. Rao, and M. Gaitan. Microwave dielecric heating of fluids in an integrated microfluidic device. *J. Micromech. Microeng.*, 17:2224–2230, 2007.

[62] J. S. Shamma and M. Athans. Analysis of nonlinear gain-scheduled control systems. *IEEE Trans. Autom. Contr.*, 35:898–907, 1990.

[63] J. S. Shamma and M. Athans. Guaranteed properties of gain scheduled control for linear parameter-varying plants. *Automatica*, 27:559–564, 1991.

[64] Y. S. Shin, K. Cho, S. H. Lim, S. Chung, S. J. Park, C. Chung, D. C. Han, and J. K. Chang. PDMS-based micro PCR chip with parylene coating. *J. Micromech. Microeng.*, 13:768–774, 2003.

[65] S. Skogestad and I. Postlethwaite. *Multivariable Feedback Control: Analysis and Design*. John Wiley & Sons, London, UK, 1996.

[66] S. Sundaresan, B. Polk, D. R. Reyes, M. V. Rao, and M. Gaitan. Temperature control of microfluidic system by microwave heating. In *Proc. 9th International Micro Total Analysis Systems (mu TAS-2005)*, pages 657 – 659, 2005.

[67] T. Takagi and M. Sugeno. Fuzzy identification of systems and its application to modeling and control. *IEEE Trans. Syst. Man Cybernet.*, 15:116–132, 1985.

[68] Y. Tanaka, M. N. Slyadnev, A. Hibara, M. Tokeshi, and T. Kitamori. Non-contact photothermal control of enzyme reactions on microchip by using a compact diode laser. *J. Chromatogr. A*, 894:45–51, 2002.

[69] T. Tood. *Microfluidic technologies for high-throughput screening applications*. PhD thesis, Biochemistry and Molecular Biophysics, California Institure of Technonolgy, 2002.

[70] E. Verpoorte. Microfluidic chips for clinical and forensic analysis. *Electrophoresis*, 23:677–712, 2002.

[71] E.W. Weisstein. Sigmoid Function. from MathWorld - a Wolfram Web Resource. [online]. Available: http://mathworld.wolfram.com/SigmoidFunction.html, 2009.

[72] T. E. Yamamoto, T. Nojima, and T. Fujii. PDMS-glass hybrid microreactor array with embedded temperature control device application to cell-free protein synthesis. *Lab on a chip*, 2:197–202, 2002.

[73] C. Zhang, J. Xu, W. Ma, and W. Zheng. PCR microfluidic devices for DNA amplification. *Biotechnol. Adv.*, 24:243–284, 2006.